SEARCH FOR CHARMED MESON-PION CONTINUUM PRODUCTION IN SEMILEPTONIC B DECAYS AT CLEO II

By

RENE JANICEK, Department of Physics

A Thesis
Submitted to the Faculty of Graduate Studies and Research
in Partial Fulfilment of the Requirements
of the Degree of
Doctor of Philosophy

McGill University

0-612-64583-5

CHARMED MESON-PION CONTINUUM PRODUCTION IN SEMILEPTONIC B DECAYS

DOCTOR OF PHILOSOPHY (2000) MCGILL UNIVERSITY
(High Energy Physics) Montreal, Quebec

TITLE: **Search for Charmed meson-Pion continuum production in Semileptonic B decays at CLEO II**

AUTHOR: Rene Janicek
Department of Physics

SUPERVISOR: Prof. Popat M. Patel

NUMBER OF PAGES: xvii, 149

Abstract

This thesis describes an experimental investigation of semileptonic B meson decays with a D and π mesons in the final state: $B^- \rightarrow D^+\pi^-e^-\bar{\nu}_e$. The data for the analysis were collected with the CLEO II detector at the Cornell Electron-positron Storage Ring. The D meson is reconstructed in the $D^+ \rightarrow K^-\pi^+\pi^+$ channel. The advantage of using this particular B decay mode is that there is no contribution from the D^* due to phase space exclusion. This analysis is the first attempt at measuring non-resonant decays semileptonic decays with the CLEO II detector. Even though we do not distinguish between higher order D resonances and the so called non-resonant decays, measuring this decay channel reveals useful information about the deficit observed in inclusive charm semileptonic B decays. We present the full neutrino reconstruction method used in extracting this decay channel from our data sample. The main difficulty comes in understanding combinatoric backgrounds and we develop two methods to solve this problem. After extensive study, no statistically significant signal is observed. So an upper limit is extracted. The result we obtain is $\mathcal{B}(B^- \rightarrow D^+\pi^-e^-\bar{\nu}_e) < 0.71\%$ at 90% C.L. This is consistent with the expected amount of $B^- \rightarrow D^+\pi^-e^-\bar{\nu}_e$ events predicted by the current models.

Résumé

Cette thèse décrit une étude de la désintégration semileptonique du méson B produisant un méson charmé D ainsi qu'un méson π dans l'état final. L'échantillon de données pour cette analyse a été collecté avec le détecteur CLEO II produit par l'anneau de collision CESR se retrouvant à l'université Cornell. Le méson D est reconstruit dans le mode de désintegration $D^+ \to K^-\pi^+\pi^+$. L'avantage d'utiliser ce mode de désintegration en particulier vient du fait que l'état excité du méson charmé D, le D^*, se trouve à être exclus en tant que source de contamination des mésons D^+ dans la réaction en question, $B^- \to D^+\pi^-e^-\bar{\nu}_e$, à cause de l'exclusion basée sur le principe de "phase space". Cette réaction $B^- \to D^+\pi^-e^-\bar{\nu}_e$ est un premier essai pour identifier et mesurer les soit dites réactions non-resonantes. Bien qu'on ne soit pas capable de distinguer les réactions contenant les excitations d'ordre supérieur du méson D et les réactions non-resonantes, la mésure de ce ratio d'embranchement s'avère a être très utile et intéressante pour la résolution du déficit observé dans le domaine des désintegrations charmées inclusives et exclusives dans le domaine de décomposition du méson B de façon semileptonique. Nous présentons la méthode de reconstruction du neutrino utilisée pour l'extraction de ce ratio d'embranchement à partir de notre échantillon de données. La difficulté principale provient des "background" combinatoires, et nous développons deux méthodes pour la résoudre. Après des études étendues, le résultat final n'est pas statistiquement significvatif. Une limite supérieure sur la mesure est ainsi calcullée. Nous obtenons un résultat final de $\mathcal{B}(B^- \to D^+\pi^-e^-\bar{\nu}_e) < 0.71\%$ at 90% C.L. Ceci est consistant avec la valeur prédite par les modèles courrants.

Acknowledgments

There are so many people who have helped me during my graduate studies at McGill and Cornell Universities, that I am not really sure where to begin. I will start by thanking my advisor, Popat Patel. His steady and strong support stand as a wonderful example for any physicist.

As for concrete and consistent assistance in my analysis, I am indebted to Kenneth W. McLean for answering so many questions, and helping me out when I needed help the most. It would have been impossible for me to complete this analysis without his guidance.

I would like to thank especially David Cassel whose continuous stream of ideas helped enormously. The improvements to the analysis from his contributions as well as his support permitting me to stay at Cornell for an extra year are greatly appreciated.

Special thanks go to Alain Bellerive for his support during my stay at Cornell as well as his guidance during my first few years as a graduate student. He was a great officemate and companion in nights to the pubs in Ithaca.

I also express my gratitude to (in alphabetical order): Roy Briere, Dave Cinabro, Karl Ecklund, Peter Gaidarev, Lawrence Gibbons, Rob Kutschke, Marko Milek, Ritchie Patterson, Chris O'Grady and Ed Thorndike.

On a personal level, I would like to thank my parents. I am grateful to them for the love and support they have given me. I would like to thank all my friends and colleagues who helped me to get through it all. You know who you are. One outstanding person I would like to point out is Dominique Dupont, your friendship and love have been a wonderful gift.

I wish to thank all the CESR staff and all the members of the CLEO collaboration since without their contribution to the experiment this would not have been possible. I would like to thank also the B-to-lepton analysis group where I presented my analysis on a monthly basis during my stay at Cornell and refined many of the techniques presented here.

I would also like to express my gratitude to the Department of Physics at McGill University, le Fonds Québécois pour la Formation de Chercheurs et l'Aide à la Recherche, and the Natural Sciences and Engineering Research Council of Canada as well as Cornell's Graduate Student Office for financial support.

Contents

List of Figures

List of Tables

Chapter 1

Introduction

Ever since humans developed the ability to think in abstract terms, they must have wondered about the basic constituents of the world around them. Already two thousand years ago they believed that matter consists of "atoms" as the most fundamental constituents. This picture hardly changed over the years. Only during the past two centuries did it change dramatically.

The atom, the Greek word for "indivisible", changed from a subject of philosophical debate into an object of scientific study when chemists began identifying the basic constituents of chemical elements. Around 1911, Ernest Rutherford's famous experiments showed that the atom must consist of two parts: a central core, positively charged, and a negatively charged cloud surrounding it, making the atom neutral as a whole. Thus it was obvious that what was being called an atom was not true to the original Greek idea, it was not the most fundamental particle in nature. The atom is a composite of a nucleus and electrons. This century has witnessed many other fundamental discoveries on this scale. As the number of subatomic particles known to human kind increased, the field of Particle Physics grew as a frontier field of physics, dedicated to the study of the fundamental building blocks of atoms and the interactions between them.

Today, the number of observed "elementary" particles exceeds one hundred [1]. To explain this wide variety of elementary particles, Gell-Mann and Zweig proposed in 1964 more fundamental constituents, quarks [2, 3]. The quark model suggests that the particles which are known as hadrons are built from quarks. This model has proved extremely successful in both classifying the known particles and predicting the existence of some unknown particles. The present improved version of the quark model assumes quarks with six different flavours and three different colours. The original model was based on three flavours (up, down, and strange). It was suspected that there could be a forth flavour, charm. One of the striking events is the discovery of the J/ψ particle in 1974 by two independent research groups [4, 5], leading to the confirmation of the charm flavour.

Evidence for the fifth quark, the bottom quark b, associated with the quantum number beauty, came from the discovery in 1977 of the lightest bottonium state, the $\Upsilon(1S)$ meson in an experiment performed at the Fermi National Laboratory (FNAL) [6].

Since the discovery of the b quark, B physics has gone through many phases and important discoveries. The Cabibbo-Kobayashi-Maskawa mixing matrix formulation and $B^0\bar{B}^0$ mixing are just two examples. Semileptonic decays played a major role in these discoveries and are being investigated further to increase our knowledge on the B meson. The main semileptonic decays investigated were the $B^- \to D^0\ell^-\bar{\nu}_\ell$ and $B^- \to D^{*0}\ell^-\bar{\nu}_\ell$. These are the exclusive decays. In parallel, the inclusive semileptonic rate had also been measured. The discrepancy between the inclusive and the sum of the exclusive semileptonic branching fractions became established and further modes have been sought after to explain it. Recently a measurement of $B^- \to D_1^0 e^-\bar{\nu}_e$ has been added to the exclusive measurements. Even though this last measurement was significant, it didn't reconcile the deficit. In the present work we will study the semileptonic decay of a B meson to a D meson and a π meson, where the D and π do not form a narrow resonance. This is one of the many non-resonant B decay channels one hopes will shed light on this deficit.

1.1 The Standard Model

In this section, we briefly describe the present theoretical model of physics at the sub-nuclear level: the Standard Model. It describes elementary particles and their interactions. This model has proven to be most adequate in explaining current experimental observations in High Energy Physics. It not only provides a framework in which high energy physicists can work but also the basis on which a more extended theory may be built in the future. Since its introduction, the Standard Model has had great success. It has been able to explain all of the validated results seen so far from particle physics experiments at accessible energies.

All matter consists of leptons and quarks, interacting through four known forces: the gravitational, the weak, the electromagnetic and the strong forces, ordered by the strength of their interactions. Each particle has an anti-particle with the same mass as the original particle but opposite quantum numbers; particles which are charge conjugation invariant are their own anti-particles.

The fundamental forces of the Standard Model postulates are shown in Table 1.1. The particles that mediate each type of interaction are also listed; these are typically bosonic particles of spin one, except for the graviton which is postulated to have spin two. The fundamental fermions of the Standard Model are divided into two sub-categories. In Table 1.2 we list the six leptons and in Table 1.3 we list the six quarks that form all the known hadrons.

Table 1.1: The fundamental interactions and their gauge bosons.

Interaction	Boson	Relative Strength	Range (m)
Strong	gluon (g)	1	10^{-15}
Electromagnetic	photon (γ)	10^{-2}	∞
Weak	W^+, W^-, Z^0	10^{-13}	10^{-18}
Gravitational	graviton (G)	10^{-42}	∞

The lepton family consists of the electron e, the muon μ and the tau τ, as well as their associated neutrinos ν_e, ν_μ and ν_τ. The leptons interact via the electromagnetic and weak forces. They all have spin 1/2 and they naturally form doublets, or generations:

$$\begin{pmatrix} \nu_e \\ e \end{pmatrix} \begin{pmatrix} \nu_\mu \\ \mu \end{pmatrix} \begin{pmatrix} \nu_\tau \\ \tau \end{pmatrix}$$

Table 1.2: Properties of the six leptons [1].

Lepton	Charge (e)	Mass (MeV/c^2)	Lifetime (s)
e	-1	0.511	$> 1.4 \times 10^{31}$
ν_e	0	< 0.000015	stable
μ	-1	105.7	2.197×10^{-6}
ν_μ	0	< 0.17	stable
τ	-1	$1777.05^{+0.29}_{-0.26}$	2.900×10^{-13}
ν_τ	0	< 18.2	stable

Table 1.3: Properties of the six quarks [1]. I_3 denotes the third component of isospin; S, C, B and T represent the strangeness, charm, bottom (or beauty) and top (or truth) quantum numbers respectively.

Quark	Charge (e)	Mass (GeV/c^2)	I_3	S	C	B	T
d	-1/3	0.0015 to 0.005	-1/2	0	0	0	0
u	2/3	0.003 to 0.009	+1/2	0	0	0	0
s	-1/3	0.060 to 0.170	0	-1	0	0	0
c	2/3	1.1 to 1.4	0	0	+1	0	0
b	-1/3	4.1 to 4.4	0	0	0	-1	0
t	2/3	173.8 ± 5.2	0	0	0	0	+1

The neutrinos possess zero electric charge and experience only weak interactions. The other leptons have unit electric charge and see both weak and electromagnetic interactions. Each generation of the leptons has an additive quantum number called lepton number (L_e, L_μ, L_τ). They are separately conserved to our experimental knowledge, but there is no firm theoretical argument that the conservation could not be broken. The neutrinos masses are assumed to be zero in the Standard Model. Other lepton generations could exist, but the experimental evidence is that there are only three generations with light neutrinos.

There are six quarks, u (up), d (down), s (strange), c (charm), b (bottom), t (top) making up a similar generation or family structure:

$$\begin{pmatrix} u \\ d \end{pmatrix} \begin{pmatrix} c \\ s \end{pmatrix} \begin{pmatrix} t \\ b \end{pmatrix}$$

The quarks interact via the electromagnetic, weak and strong forces.

The fundamental particles have to interact with each other in order to be observable. These interactions are mediated via the four gauge bosons mentioned previously. The gravitational force, although the earliest discovered, is the least important in particle physics, because its magnitude is so much weaker than any of the other forces. The electromagnetic interaction is by far the most precisely calculable. The mediator of the electromagnetic force is the photon, γ, and is responsible for most interactions at the atomic and macroscopic scales. The weak interaction is responsible, for example, for nuclear β decays which are viewed as transitions between quarks. The electromagnetic interaction and weak interaction have been put together beautifully into a unified $SU(2) \times U(1)$ electroweak theory [7].

Quarks do not exist freely. They are bound together by strong interactions. Particles composed of quarks are called hadrons. A quark and an anti-quark form a meson, three quarks form a baryon. The fact that hadrons can exist in the form of baryons decuplets (in which three quarks occupy the same state) led to an important discovery, colour. The resulting force is the essential piece of Quantum Chromodynamics or QCD. There are three colours forming a $SU(3)$ colour group. Each quark carries a single colour. The gluon, which carries the colour force, is exchanged between the quarks. A physical particle has to be in a colour neutral state because, unlike other forces, the colour force increases with distance. The principle of "asymptotic freedom" determines that the renormalized QCD coupling is small only at high energies, and it is only in this domain that high-precision tests, similar to those in QED (Quantum Electrodynamics) can be performed using perturbation theory.

Although asymptotic freedom suggests quarks are free within hadrons, the nonperturbative nature of QCD makes it difficult to extract hadron weak decay properties. To study weak interactions, one has to understand the effects of QCD. One way to avoid strong interaction effects is to study semileptonic decays of hadrons, because leptons do not participate in strong interactions. However, because of the difficulty of detecting the neutrino experimentally, semileptonic decays are not always easy to observe and reconstruct fully. Hadronic or nonleptonic decays, are, on the other hand, more difficult to deal with theoretically, but easier to fully reconstruct experimentally. By resorting to some approximations, for example Heavy Quark Effective Theory (HQET) [8], and symmetries among different quarks, we can extract weak decay information to a good extent.

The dynamics of interacting particles in the SM are described by the interaction terms in the Lagrangian. Since the unified electromagnetic and weak interactions are invariant under weak isospin $\mathrm{SU}(2)_L$ and weak hypercharge $\mathrm{U}(1)_Y$, the electroweak Lagrangian contains a $\mathrm{SU}(2) \times \mathrm{U}(1)$ symmetry. The electroweak Lagrangian contains three terms: one for the weak charge current, one for the weak neutral current, and one for the electromagnetic neutral current. Explicitly:

$$\begin{aligned}\mathcal{L} &= \mathcal{L}(\text{Weak CC}) + \mathcal{L}(\text{Weak NC}) + \mathcal{L}(\text{EM NC}) \\ &= \frac{g}{\sqrt{2}}\,(J_\mu^- W_\mu^+ + J_\mu^+ W_\mu^-) + \frac{g}{\cos\theta_W}\,(J_\mu^0 - \sin^2\theta_W\, J_\mu^{\mathrm{EM}})\, Z_\mu + e\, J_\mu^{\mathrm{EM}} A_\mu, \quad (1.1)\end{aligned}$$

where $W_\mu^\pm$, Z_μ, and A_μ represent the field operators for the physical gauge bosons $W^\pm$, Z^0, and γ, respectively. The coupling constants for the weak and electromagnetic interactions are related by the weak mixing angle, θ_W:

$$e = g\,\sin\theta_W\,. \quad (1.2)$$

Finally, the $J_\mu^\pm$, J_μ^0 and J_μ^{EM} denote the charged weak, neutral weak, and electromagnetic currents. For the charged leptonic weak current, we have:

$$J_\mu^+ = (\bar\nu_e, \bar\nu_\mu, \bar\nu_\tau)\,\frac{1}{2}\,\gamma_\mu\,(1-\gamma^5)\begin{pmatrix} e \\ \mu \\ \tau \end{pmatrix}, \quad (1.3)$$

where the γ_μ are the usual Dirac matrices and $\gamma^5 = i\gamma_0\gamma_1\gamma_2\gamma_3$. The formulation of this current expresses the empirical fact that leptons only couple within their own generation. In the case of the quarks, on the other hand, inter-generational couplings are observed. The theory handles this experimental fact by making the weak eigenstates of quarks different from the mass eigenstates. By convention, the

u, c, and t quarks are unmixed, while the weak eigenstates of the d, s, and b quarks are given by linear combinations of their mass eigenstates. The weak charged current involving quarks is therefore given by:

$$J_\mu^+ = (\bar{u}, \bar{c}, \bar{t})\,\frac{1}{2}\,\gamma_\mu\,(1-\gamma^5)\begin{pmatrix} d' \\ s' \\ b' \end{pmatrix}. \tag{1.4}$$

with the primed quarks being related to their physical counterparts by the Cabibbo-Kobayashi-Maskawa (CKM) matrix [9]:

$$\begin{pmatrix} d' \\ s' \\ b' \end{pmatrix} = \begin{pmatrix} V_{ud} & V_{us} & V_{ub} \\ V_{cd} & V_{cs} & V_{cb} \\ V_{td} & V_{ts} & V_{tb} \end{pmatrix}\begin{pmatrix} d \\ s \\ b \end{pmatrix}. \tag{1.5}$$

The CKM matrix is a generalization of the Cabibbo hypothesis postulated since 1963 [10]. Since the elements of the CKM matrix can be complex, a total of eighteen numbers are needed to describe all the terms of the matrix. By imposing unitarity, and by redefining the quark fields to remove unphysical phases, the numbers of parameters can be reduced from eighteen to four. These four parameters can be chosen as three angles $(\theta_{12}, \theta_{13}, \theta_{23})$ and one phase (δ). The CKM matrix can then be written as:

$$V = \begin{pmatrix} c_{12}c_{13} & s_{12}c_{13} & s_{13}e^{-i\delta} \\ -s_{12}c_{23} - c_{12}s_{23}s_{13}e^{i\delta} & c_{12}c_{23} - s_{12}s_{23}s_{13}e^{i\delta} & s_{23}c_{13} \\ s_{12}s_{23} - c_{12}c_{23}s_{13}e^{i\delta} & -c_{12}s_{23} - s_{12}c_{23}s_{13}e^{i\delta} & c_{23}c_{13} \end{pmatrix}. \tag{1.6}$$

where $c_{ij} = \cos\theta_{ij}$, $s_{ij} = \sin\theta_{ij}$, and i, j denote the quark generations.

Based on the empirical observation that the mixing angles have a hierarchical structure such that we can expand in powers of the Cabibbo angle $\lambda = s_{12} = \sin\theta_{12} = 0.226$, with $s_{23} = A\lambda^2$ and $s_{13}e^{-i\delta} = A\lambda^3(\rho - i\eta)$. The CKM matrix takes the form [11]:

$$V \simeq \begin{pmatrix} 1-\frac{1}{2}\lambda^2 & \lambda & A\lambda^3(\rho - i\eta) \\ -\lambda & 1-\frac{1}{2}\lambda^2 & A\lambda^2 \\ A\lambda^3(1-\rho-i\eta) & -A\lambda^2 & 1 \end{pmatrix}. \tag{1.7}$$

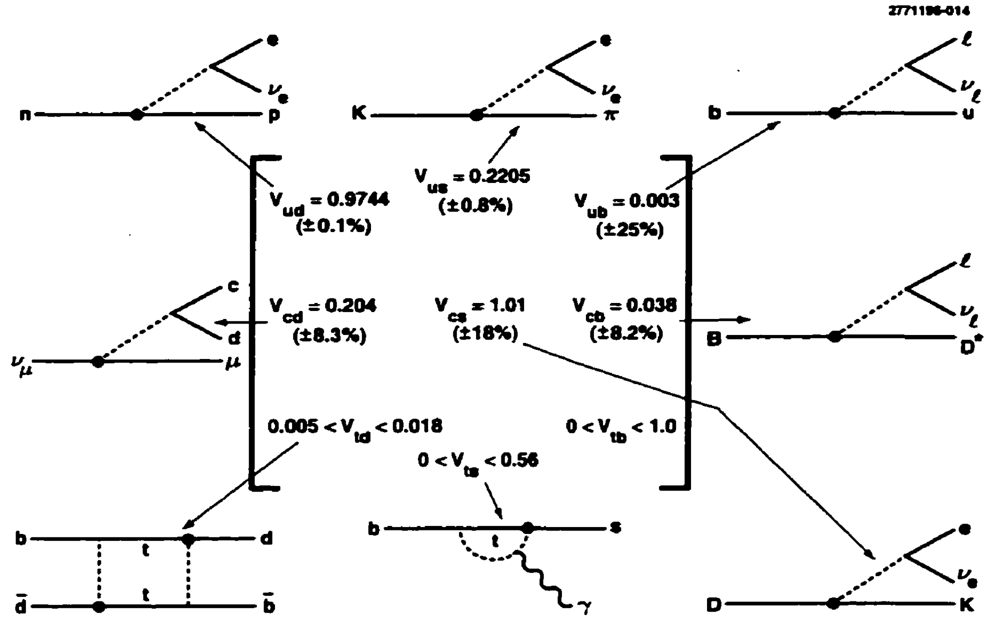

Figure 1.1: The measured values of CKM matrix elements and a schematic diagram indicating the processes used to measured them [12].

In Figure 1.1 a summary of the measured values of the various CKM matrix elements is given as well as the experimental ways of actually measuring these matrix elements.

One must also include the gluonic fields in the SM framework. The theory which describes the strong interaction in the Standard Model is called Quantum Chromodynamics (QCD). To describe QCD, the electroweak Lagrangian is extended to include an SU(3) colour symmetry. The mediator of the strong force, the gluon, couples to the colour charge of the quark and therefore belongs to an octet representation of SU(3). Although QCD is not tested to the same extent as QED, it is nevertheless in impressive agreement with a large body of experimental data. The favored form of the resulting strong interaction potential for short interquark distances ($r \lesssim R_{\mathrm{hadron}} \simeq 1/\Lambda_{\mathrm{QCD}} \simeq 1$ fm) is:

$$V_{\mathrm{QCD}} \simeq -\frac{4\,\alpha_s}{3\,r}\,, \tag{1.8}$$

where α_s is the strong coupling constant between quarks and gluons. At large distances ($r > 1$ fm), a confining term must be added to the Coulomb type potential to confine quarks inside hadrons.

Although the SM has great predictive power, it contains many free parameters. The gauge coupling constants ($\alpha_{\rm em}$, G_F, α_s), the parameters of the Higgs field (m_Z, θ_W, $m_{\rm Higgs}$), the fermions (quarks and leptons) masses, and the CKM matrix elements all have to be determined experimentally.

1.2 Motivation For The Present Analysis

From the study of semileptonic decays of the B mesons, one outstanding puzzle has remained over time. Basically the problem remains that the branching ratios into the exclusive final states that have been measured do not add up to the inclusive semileptonic branching fraction.

The known deficit in semileptonic $b \to c$ decays has been a problem for a long time. The inclusive charmed semileptonic branching fraction of $b \to c\ell\nu$ ($\sim$ 10.5%) is not fully saturated by observed exclusive decays $\bar{B} \to D\ell\bar{\nu}$ and $\bar{B} \to D^*\ell\bar{\nu}$ which cover 70% of it. A recent CLEO measurement of $\bar{B} \to D^{**}e^-\bar{\nu}_e$ has added an additional 0.56% [13] to the absolute branching ratio, or reduced the 30% deficit by 5%. There is still almost 2.1% unaccounted for. It is believed that the non-resonant decays should cover the major part of this deficit [14]. By non-resonant decays we mean there is no enhancement at a certain $M_{D\pi}$, like would be the case for a D^{*+} resonance which occurs at a $M_{D\pi}$ = 2010MeV. The non-resonant contributions are the continuum production to the resonant states. The following table summarizes the status of CLEO measurements :

1.3 Thesis Outline

This thesis will concentrate on the study of a particular semileptonic decay, the decay of a B lepton to a non-resonant D π system plus the electron and the neutrino. Chapter 2 outlines the theoretical framework related to B meson physics. This is

Table 1.4: Charmed semileptonic B decays. I emphasize that all the measurements shown below are from one detector - that differences do not come and go due to different systematic errors between detectors.

Decay Mode	Branching Fraction	
$B^- \to X_c e^- \bar{\nu}_e$	$(10.49 \pm 0.46)\%$	[15]
$B^- \to D^0 e^- \bar{\nu}_e$	$(1.94 \pm 0.37)\%$	[16]
$B^- \to D^{*0} e^- \bar{\nu}_e$	$(5.13 \pm 0.84)\%$	[17]
$B^- \to D_1^0 e^- \bar{\nu}_e$	$(0.56 \pm 0.16)\%$	[13]
$B^- \to D_2^{*0} e^- \bar{\nu}_e$	$< 0.8\%$ @ $90\% C.L.$	[13]
Inclusive-Exclusive	$\lesssim (2.1 \pm 1.0)\%$	

presented in order to put the present analysis in perspective. In chapter 3 we present the outline of our experimental setup. Chapter 4 will discuss the idea behind particle selection, the optimization process for selecting signal events and how we proceed to obtain our present result. Also the data set used will be presented and the various Monte Carlo sets used will be described. In chapter 5 we present the results we obtain and also some interpretations. Finally chapter 6 is the conclusion and presents some interpretations of our results. We also append a brief summary of the procedure that has been used between the process of data collection and the process of data analysis, the calibration of the detector. This has played a big part in the final outcome of this analysis and also was one of my personal contributions to the experiment.

Chapter 2

Theoretical Framework

In this chapter we present the theory needed to better understand the analysis discussed in this thesis. In the first section we briefly outline the discovery of the Υ Resonances and the B Mesons. Then we present the idea behind the semileptonic decays. Following that we present the main theoretical models relevant for B semileptonic decays. First we discuss the formalism of Heavy Quark Effective Theory, HQET. Second we discuss the model of ISGW2 which provides a basis for understanding semileptonic decays. We also discuss some other relevant theories that were once used for semileptonic decays. Last, but not least, we present the Goity and Roberts model, which is addressed to understanding non-resonant B semileptonic decays. We also present an alternate model for these non-resonant decays, the Isgur model, which has been published recently.

2.1 Υ Resonances and B Mesons

As mentioned in the Introduction, the discovery of the first $b\bar{b}$ states goes back to 1977. Two experiments, the pioneering one at Fermilab, the confirming one at the DORIS storage ring at DESY made the observation. The first used pN scattering experiments, while the other used e^+e^- annihilation. Both experiments observed an excess of events at masses of 9.5 GeV/c^2 and 10 GeV/c^2. These two resonances are identified as the $b\bar{b}$ bottomonium states $\Upsilon(1S)$ and $\Upsilon(2S)$.

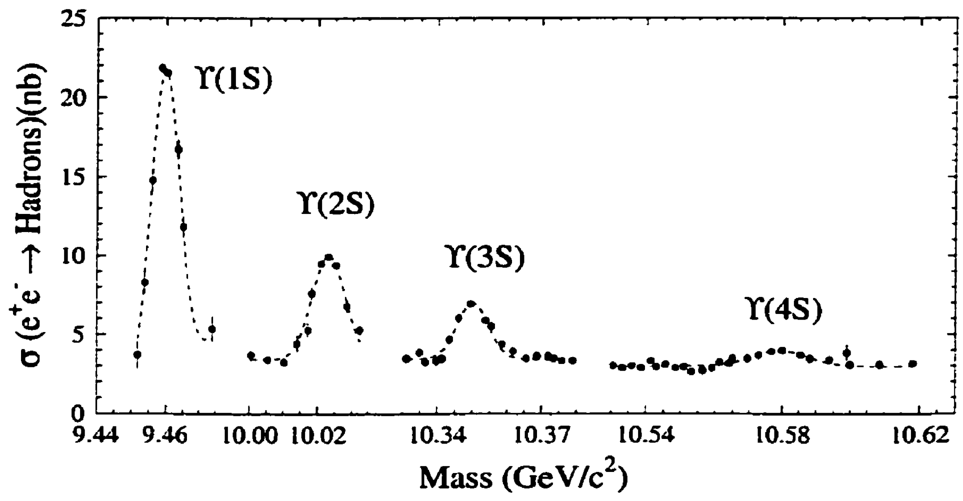

Figure 2.1: The four Υ resonances in $b\bar{b}$ annihilation.

The study of the b quark was extensively pushed at CESR (Cornell Electron Storage Ring) after it began to operate in 1979. Since it was able to deliver center of mass energies around 10-11 GeV, it was well suited to study the family of Υ resonances. During the period from 1980 to 1985, three new resonances were discovered: $\Upsilon(3S)$, $\Upsilon(4S)$ and $\Upsilon(5S)$. In Figure 2.1 we show the total hadronic cross-section for e^+e^- annihilations in the $\Upsilon(1S)$ through $\Upsilon(4S)$ energy region, as measured at CESR. From this figure one can see that the $\Upsilon(4S)$ resonance is broader than the other Υ resonances, whose widths are consistent with the storage ring energy spread. This is the consequence of the $\Upsilon(4S)$ resonance lying above the threshold for B meson pair production. In 1982, the ARGUS experiment at the reconstituted DORIS storage ring joined the competition. Since then they accumulated high statistics at the $\Upsilon(4S)$, which is the principal source of B meson decays. Today experiments like CDF at the Tevatron and most of the LEP detectors have also accumulated a significant sample of B mesons at higher CMS energies. More recently, 2 new B-factories have started taking data, the BaBar detector at PEP II and Belle at KEK.

In Figure 2.2 (a)-(c) the possible decay mechanisms of $\Upsilon(1S)$, $\Upsilon(2S)$ and $\Upsilon(3S)$ are shown. Figure 2.2 (d) and 2.3 show how B mesons are produced at the

$\Upsilon(4S)$ resonance, via popping-off of a light quark - anti-quark pair ($q = u, d$). The narrow width of the three lower lying resonances is explained by the empirical OZI rule which states that, if in a particle decay all energy is transformed via gluons ("hard gluons"), then the decay is heavily suppressed. This can also be understood by means of the running coupling constant of the strong interaction: at high gluon energies, the strong interaction weakens, resulting in a suppression of decays of the above kind, compared to the decays involving "soft gluons". This suppression results in a narrow width observed for the particle under consideration. The OZI rule applies to the hadronization processes depicted in Figures 2.2 (a) and (b). The electroweak annihilation process shown in Figure 2.2 (c) is suppressed compared to the $\Upsilon(4S) \rightarrow B\bar{B}$ process due to the relative strengths of the interactions involved.

The B mesons themselves decay after a lifetime of roughly 1.6 ps [1], mostly into final states containing the charm quark. There are at least five different mechanisms through which this decay can proceed: external W-emission ("spectator"), internal W-emission ("colour mixed"), annihilation, W-exchange, and "Penguin" processes. The corresponding quark level diagrams are displayed in Figures 2.4 (a) through (e) respectively. In the spectator model, Figure 2.4 (a), mesons are easily produced in B decays. Since the weak coupling of $b \rightarrow cW^-$ (or, at a much lower rate, $b \rightarrow uW^-$) does not alter the colour state of the quarks in the B meson, the colours of the heavy quark and the light anti-quark remain perfectly matched and nicely combine to form charmed mesons. If the decay proceeds through internal W-emission, as shown in Figure 2.4 (b), the colours of the quark and anti-quark from the W-vertex have to match the colours of the heavy and light quark. This requirement reduces the number of possible final states by a factor of 3 (given that "colour" comes in three varieties). One would therefore naively expect that this mechanism is "colour suppressed" by a factor of 9 when compared to the spectator process. The remaining three mechanisms are also suppressed, especially the "Penguin" process, which involves gluon exchange between the heavy and the light quarks in addition to the weak interaction.

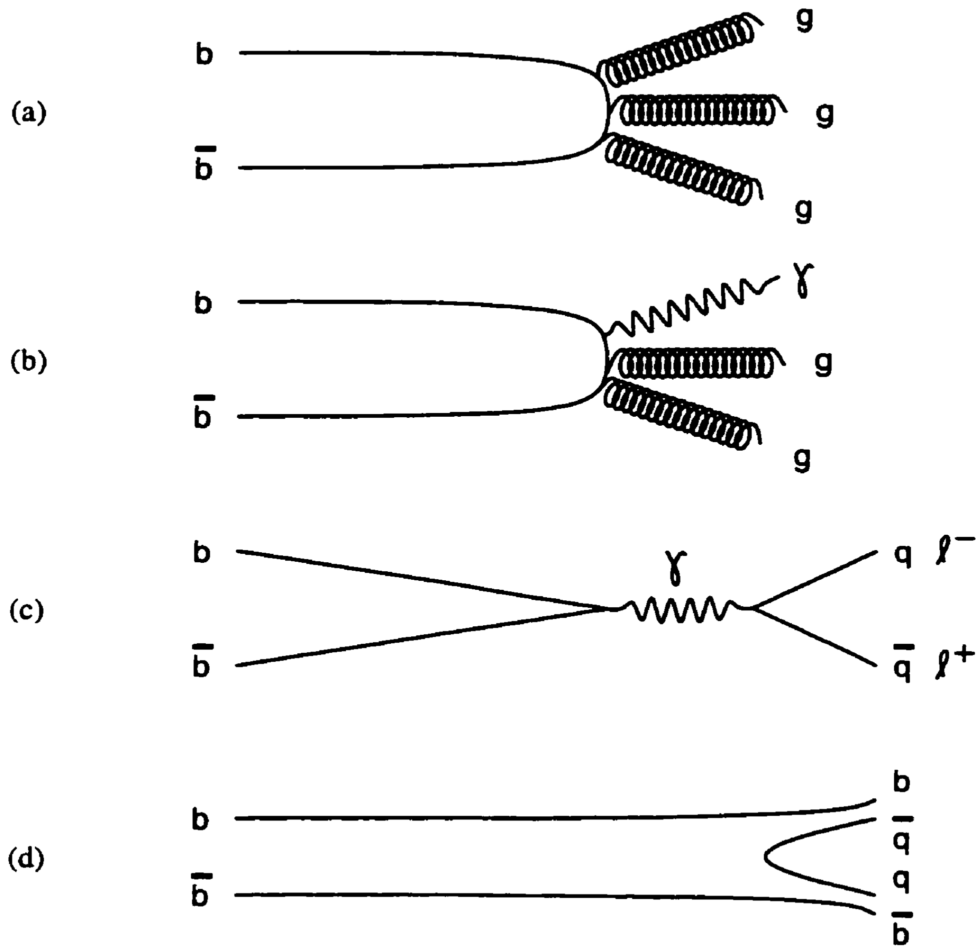

Figure 2.2: The principal decay modes of the four different Υ resonances decay methods. (a) through (c) is for the $\Upsilon(1S)$ to $\Upsilon(3S)$ resonances which decay via b and $\bar{b}$ annihilation, and (d) shows how B mesons are formed in $\Upsilon(4S)$ decay.

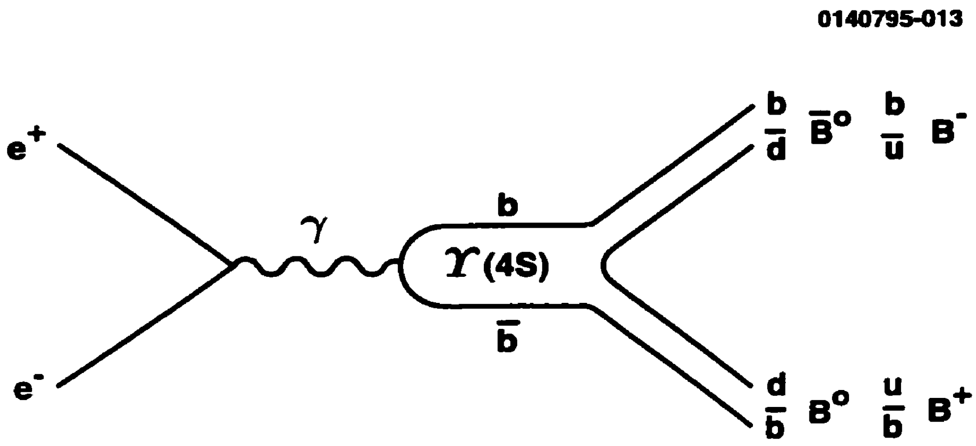

Figure 2.3: B meson production.

2.2 B Semileptonic Decays

As pictured in the diagram in Figure 2.5 , a $\bar{B}$ meson consists of a heavy b quark and a light $\bar{u}$, $\bar{d}$ or $\bar{s}$ anti-quark, bound together with the strong force. The b quark emits via the W boson the lepton (electron or muon) and the corresponding anti-neutrino. What remains is usually a hadronic system containing a c quark. Approximately 0.6 % of the time the b quark decays to a u quark. Events where the lepton is a tau are also possible but these decays are phase space suppressed in our case due to the large mass of the tau lepton. Semileptonic decays are relatively easy to understand because calculations for the leptonic part of the decays follow from the electroweak theory.

The inclusive semileptonic branching fraction at the $\Upsilon(4S)$ resonance is related to the total decay width (Γ_{TOT}) and the semileptonic decay width (Γ_{SL}) of the B meson by:

$$\mathcal{B}_{\mathrm{SL}} = \frac{\Gamma_{\mathrm{SL}}}{\Gamma_{\mathrm{TOT}}} = \tau_B \, \Gamma_{\mathrm{SL}} \,, \tag{2.1}$$

since τ_{B^+}/τ_{B^0} is consistent with unity [1]. The branching fraction for an exclusive

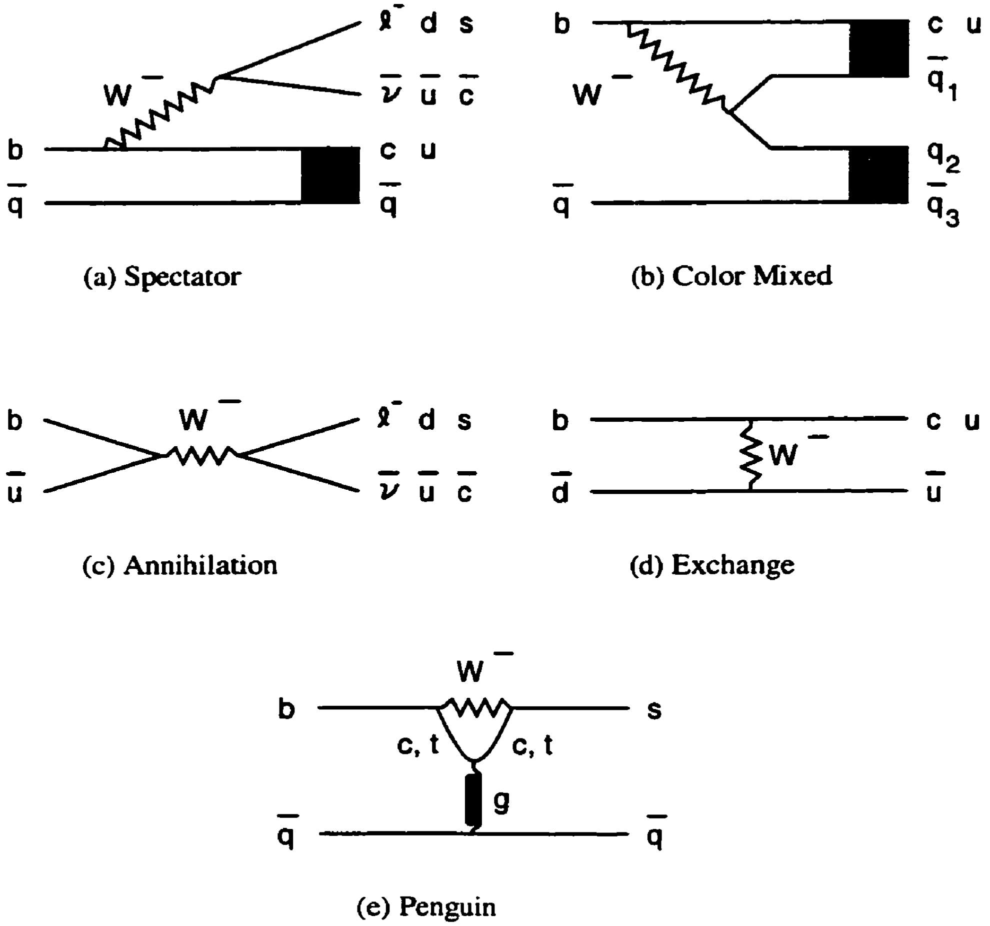

Figure 2.4: The five different B meson decay mechanisms using quark level diagrams. (a) External W-emission ("spectator"), (b) Internal W-emission ("colour mixed"), (c) Annihilation, (d) W-exchange and (e) "Penguin"

.

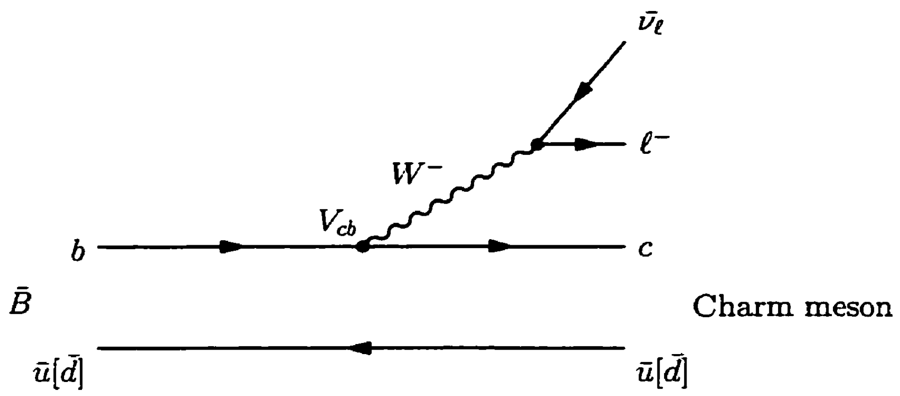

Figure 2.5: Semileptonic B decay

semileptonic decay of a $\bar{B}$ meson is given by:

$$\mathcal{B}(\bar{B} \to H\,\ell\bar{\nu}_\ell) = \frac{\Gamma(\bar{B} \to H\,\ell\bar{\nu}_\ell)}{\Gamma_{\mathrm{TOT}}}, \tag{2.2}$$

where $\Gamma(\bar{B} \to H\,\ell\bar{\nu}_\ell)$ is the partial width for $\bar{B} \to H\,\ell\bar{\nu}_\ell$. The state H denotes a particular hadronic final state kinematically allowed in semileptonic $\bar{B}$ decays, but most often turns out to be a D, D^* or D^{**} meson. Combinations of these mesons with other light pions should also be considered. One simple consequence of this definition is that the sum of all exclusive decay branching fractions has to be the inclusive branching fraction.

In the following sections we will describe how these inclusive and exclusive measurements are carried out as well as quote the most recent measurements. These, basically lead to the main reason for this analysis: the lack of exclusive decays to saturate the inclusive rate.

2.2.1 Inclusive Decays

At the $\Upsilon(4S)$, the inclusive B semileptonic branching fraction ($\mathcal{B}_{\mathrm{SL}}$) is:

$$\mathcal{B}_{\mathrm{SL}} = \sum_{i=u,c} \mathcal{B}(b \to q_i \ell\bar{\nu}_\ell) = \mathcal{B}(b \to u\ell\bar{\nu}_\ell) + \mathcal{B}(b \to c\ell\bar{\nu}_\ell)$$

$$= \sum_{i=\text{Hadrons}} \mathcal{B}(\bar{B} \to H_i \ell \bar{\nu}_\ell), \tag{2.3}$$

where H_i is any allowed hadronic final state.

In the inclusive approach, the sum over all possible final states is considered, ignoring the detailed breakdown among the individual decay modes.

Experimentally, the inclusive B semileptonic decay branching fraction is obtained by counting the number of leptons from b quarks. Determination of this inclusive semileptonic branching fraction can be accomplished by many ways but we will refer to the main two methods used by the ARGUS and the CLEO collaborations. The first one is the model dependent method since it is based around the spectral fitting to a single lepton spectrum composed of leptons from the b hadrons (primary leptons) and leptons from charm decays (secondary leptons). The other one is the model independent method. It uses the charge and angular correlations in dilepton events to extract the primary lepton spectrum. We shall discuss the results of both methods in the following two subsections.

- Model dependent method

  This method as its name suggests is based on a certain model that describes the different semileptonic decays. Most recent analyses use the ISGW II model, but previous measurements have been done with the first version of the ISGW model or the ACCMM model as well as others. Each exclusive decay mode is included and the overall shape of the sum of the primary and secondary lepton curves is fitted to the data plot distribution. From this, one can extract the portion carried by the primary lepton contributions and hence get a number for the inclusive branching ratio. Figure 2.6 shows the various fits to CLEO II data using either the ACCMM or the ISGW model. Parts a and b of Figure 2.6 represent the overall fit used for the extraction of the inclusive semileptonic rate, while parts c and d show the various modeled exclusive contributions.

- Model independent method

  The model independent method is the preferred method since it almost doesn't depend on any theoretical model. In fact, only the region below the detector

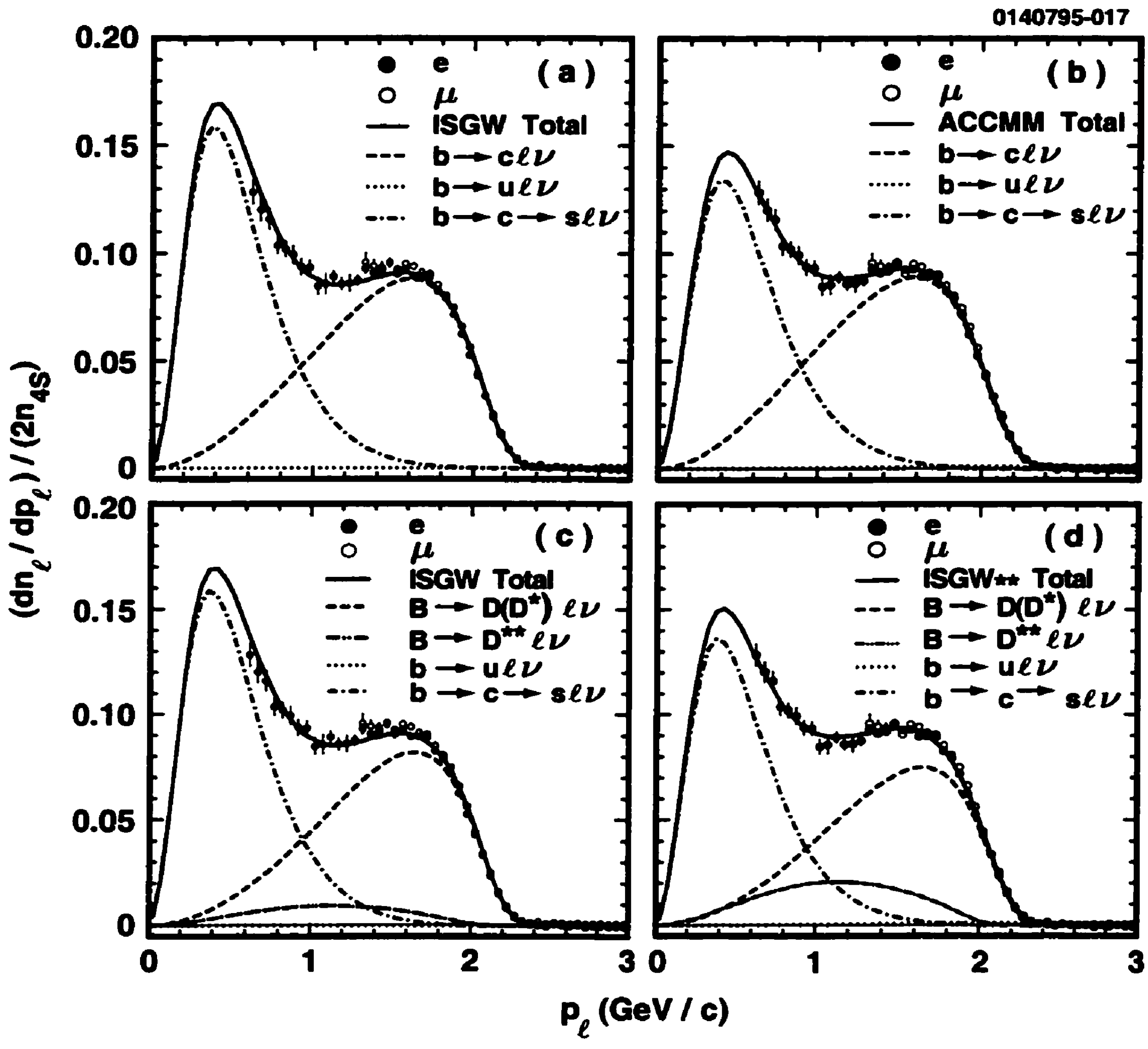

Figure 2.6: Model dependent semileptonic inclusive B decays

acceptance has to be modeled. This method is also called the di-lepton technique. The main idea is that one requires one high momentum lepton as a tag, with a $p_\ell > 1.4$ GeV/c. From the distinction of primary and secondary lepton distributions, this high momentum lepton is most likely a primary lepton. Only 2.8% of these high momenta leptons are secondary. This first lepton is used as a tag. Once a tag has been set we then look at another lepton in the event with a $p_\ell > 0.6$ GeV/c for which the lepton spectrum will be extracted. If this extra lepton is of the same charge as the tag lepton then it is necessarily a secondary lepton.

If on the other hand it is of the opposite charge as the tag lepton, then it will either be a primary lepton or a secondary lepton coming from the same B as the tag lepton. The goal in this case is to distinguish the two possibilities in order to extract only the distribution of the primary lepton. There could be further ambiguities coming from events where we have $B^0\bar{B}^0$ mixing but since this rate is well measured, it is not difficult to correct for this effect.

If the two leptons in the event are from the decay chain of the same B meson, then there is a strong angular correlation, resulting from momentum conservation, such that they tend to be in opposite hemispheres. On the other hand, leptons coming from different B mesons have uncorrelated angular distributions since the two B mesons are produced almost at rest at the $\Upsilon(4S)$. Following from the previous argument, if we require the two leptons to be found in the same hemisphere, events coming from the decay chain of a single B meson are effectively removed. This extra lepton then must be a primary lepton. We can then measure the number of primary and secondary leptons in each momentum bin. Figure 2.7 shows the fit to the two spectra, primary (black circles) and secondary (white circles) electrons, as obtained from the CLEO data set. The only place where one needs to take a certain model into account is for the momentum region below 600 MeV. This is a small contribution to the overall distribution.

A summary of the inclusive decays is found in Figure 2.8. First the model

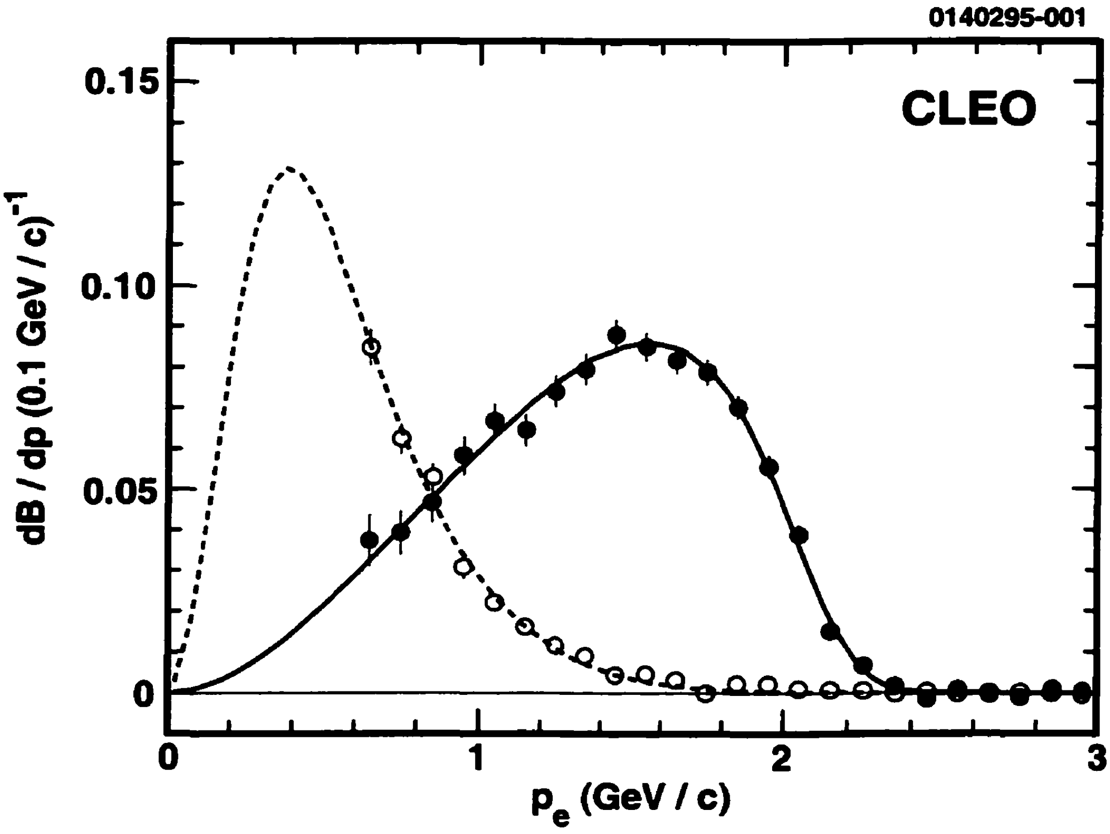

Figure 2.7: A fit to the semileptonic inclusive B decays using the model independent method. A clear distinction between the primary (black circles) and secondary (white circles) electrons can be seen.

dependent measurements are outlined and then the model independent ones. Both the CLEO and the ARGUS results are presented. The average from the two experiments for the inclusive semileptonic branching fraction based on the model independent method is $10.18 \pm 0.40\%$.

2.2.2 Exclusive Decays

In the past the main exclusive decays that were measured were the $B^- \rightarrow D^0\ell^-\bar{\nu}_\ell$ and $B^- \rightarrow D^{*0}\ell^-\bar{\nu}_\ell$. It has been assumed that these two decays would saturate most of the inclusive rate as is the case in the corresponding semileptonic D meson decay, where $D \rightarrow \bar{K}\ell\bar{\nu}_\ell$ and $D \rightarrow \bar{K}^*\ell\bar{\nu}_\ell$ saturate the total rate. The measurement of the $B^- \rightarrow D^{*0}\ell^-\bar{\nu}_\ell$ branching fraction has been easier to accomplish due to the larger data sample containing these events, but also because of the difference between the D^* and D masses. This mass difference is a very powerful criterion to reject background events in the process of selecting semileptonic D^* decays. New methods have been developed such as the one used in this thesis to deal with the more background dominated $B^- \rightarrow D^0\ell^-\bar{\nu}_\ell$ mode and we now have a good measurement of this mode as well. Figure 2.9 gives a summary of these two decays from various experiments. These are mainly the CLEO and ARGUS detectors but the LEP experiments from CERN have contributed to some of the measurements.

More recently CLEO II has made a measurement of one semileptonic decay to D^{**}, the $B^- \rightarrow D_1^0\ell^-\bar{\nu}_\ell$. This measurement has been carried out using a similar approach as in the $B^- \rightarrow D^{*0}\ell^-\bar{\nu}_\ell$ case but by adding an extra pion to the D^* and then looking at the mass difference between the D^{**} and the D^*. The branching fraction for this decay is measured to be $(0.56 \pm 0.16)\%$. This same analysis has also made an attempt at measuring the $B^- \rightarrow D_2^{*0}\ell^-\bar{\nu}_\ell$ decay. In this case it has been slightly limited by the statistical significance of the final result and an upper limit has been published instead. This sets a $90\% C.L.$ on this decay at being $< 0.8\%$.

This summarizes all the exclusive measurements made so far for the charged B meson, the neutral B meson having similar measurements. As we know there are other exclusive channels that decay to D^{**} but these are rather broad resonances and

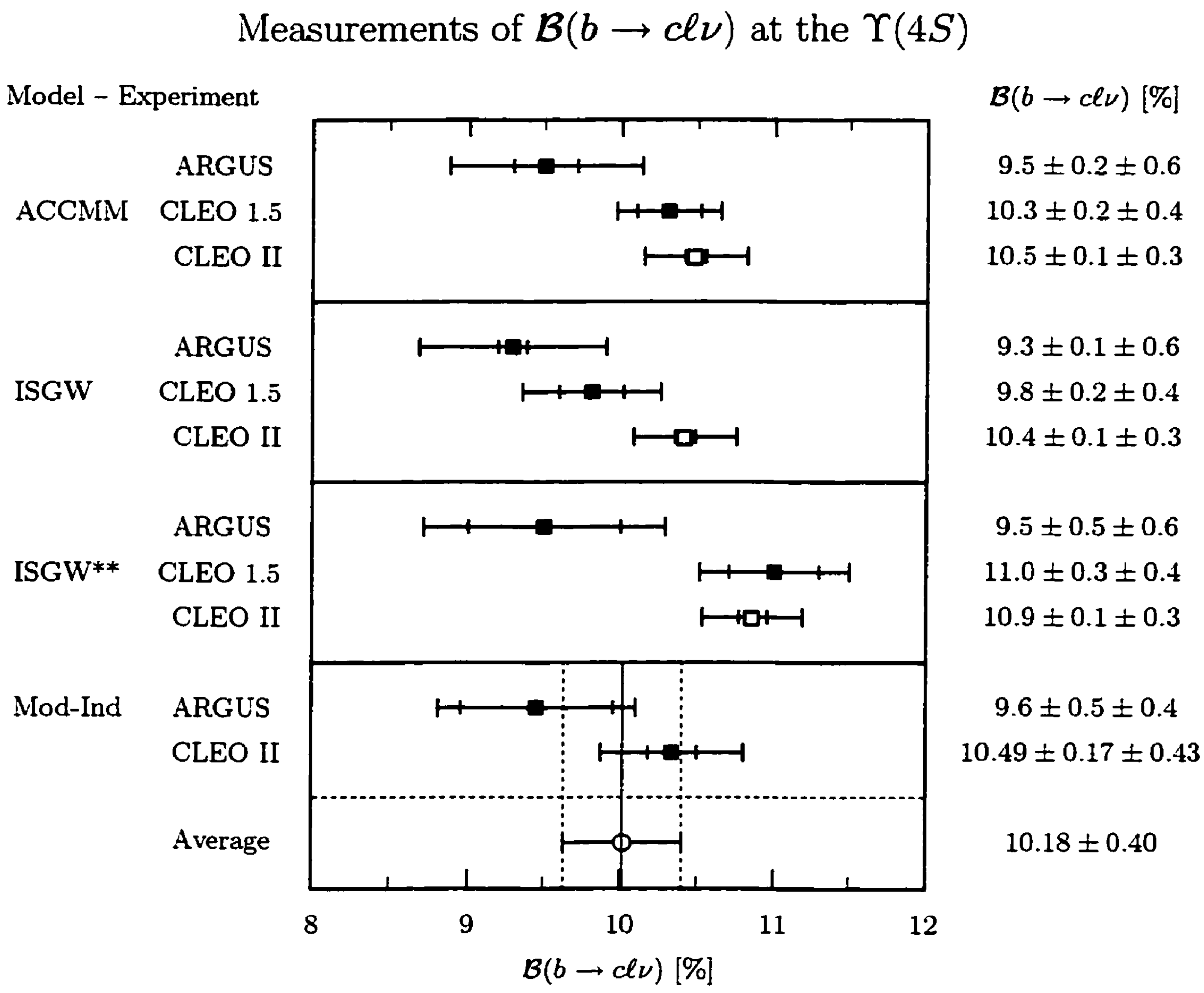

Figure 2.8: Semileptonic inclusive B decay

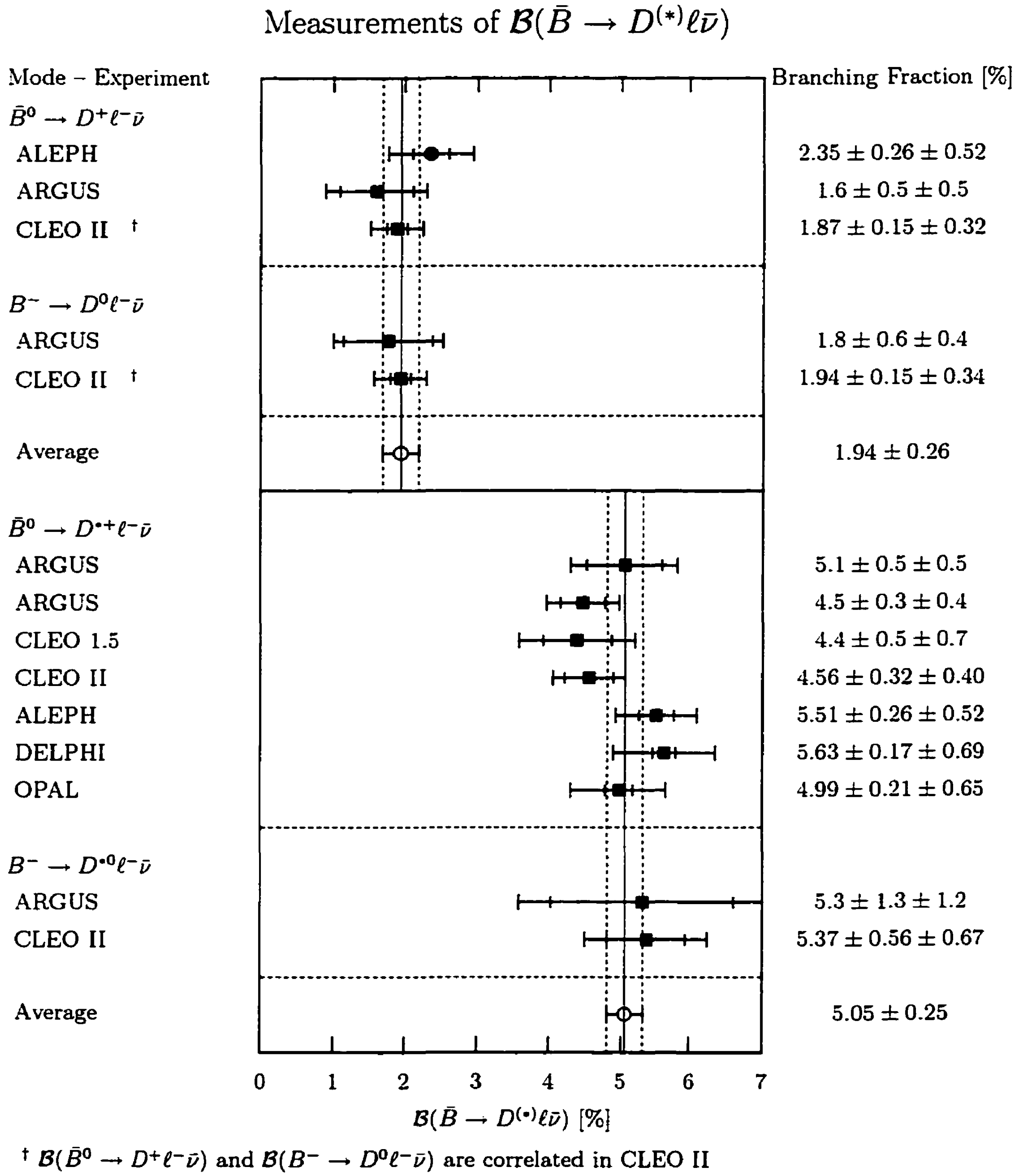

Figure 2.9: Semileptonic exclusive B decay

therefore very difficult, if not impossible, to measure. There are also all the non-resonant decays with a $D^{(*)}$ in the final state that need to be accounted for. Since this analysis is not able to distinguish between the $D^{**} \to D\pi$ and a non-resonant $D\pi$ contribution it will be a more broad measurement of all the decays going to the final hadronic $D\pi$ system. There is no D^* contribution as it is below the $D\pi$ production threshold.

2.3 Free Quark Model

In this section and the remaining sections of this chapter, we will outline the various theoretical models used in the process of this analysis. These are mainly models for semileptonic decays. Our Monte-Carlo samples are generated using these models.

The simplest description of the B meson decay treats the spectator quark as a free particle. The free quark model was developed in the scheme of inclusive decays and therefore leads to prediction for the inclusive lepton energy spectrum.

The partial width for the inclusive semileptonic decay of a free quark Q can be written as:

$$\Gamma(Q \to q\,\ell^- \bar{\nu}_\ell) = \frac{G_F^2 m_Q^5}{192\pi^3} |V_{qQ}|^2\, I(x)\,, \tag{2.4}$$

where $I(x)$ is the phase factor for QED radiative corrections and $x = m_q/m_Q$, and V_{qQ} is the respective CKM matrix element. The factor $I(x)$ is close to one for $b \to u\,\ell\bar{\nu}_\ell$ and approximately 0.5 for $b \to c\,\ell\bar{\nu}_\ell$. Here, the analogy with muon decay is obvious

$$\Gamma(\mu^- \to e^- \nu_\mu \bar{\nu}_\ell) = \frac{G_F^2 m_\mu^5}{192\pi^3}\,. \tag{2.5}$$

The rate is modified by the exchange of gluons between quarks in semileptonic decays in the free quark model. These corrections are expressed by the function $g(x)$ which modifies Equation (2.4) to become:

$$\Gamma(Q \to q\,\ell^- \bar{\nu}_\ell) = \frac{G_F^2 m_Q^5}{192\pi^3} |V_{qQ}|^2\, I(x) \left[1 - \frac{2}{3\pi}\alpha_s g(x)\right]. \tag{2.6}$$

The ACCMM model [18] was one of the first models to incorporate bound state effects to the free quark model. These effects can significantly modify the lepton energy spectrum. In the ACCMM model, the momentum of the light quark within the decaying meson is modeled by a Gaussian distribution $\phi(p)$ which has the form:

$$\phi(p) = \frac{4}{\sqrt{\pi} p_F^3} \exp\left(-\frac{p^2}{p_F^2}\right) . \tag{2.7}$$

The parameter p_F is the Fermi momentum ($p_F = 150$ MeV/c to 300 MeV/c).

The free quark spectator model gives a prediction for the lepton energy spectrum for semileptonic decays of the B meson to charm mesons.In the b quark rest-frame, the partial decay width is:

$$\frac{d\Gamma(b \to c\,\ell\bar{\nu}_\ell)}{dy} = \frac{G_F^2 m_b^5}{192\pi^3} |V_{cb}|^2 \, \Phi(x,y)\, G(x,y), \tag{2.8}$$

where $x = m_c/m_b$ and $y = 2E_\ell/m_b$. The phase space factor is $\Phi(x,y)$ and $G(x,y)$ incorporates the effects of gluon radiation [18]. To compute the lepton energy spectrum, the decay distribution in the b quark rest frame is boosted to the B meson frame. The spectator quark in this model is assumed to have a definite mass $m_{\rm sp}$, but the b quark is a virtual particle of variable mass

$$m_b^2 = m_B^2 + m_{\rm sp}^2 - 2m_B\sqrt{m_{\rm sp}^2 + p^2}. \tag{2.9}$$

Thus, the ACCMM model has three free parameters: the Fermi momentum, the effective mass for the light degrees of freedom $m_{\rm sp}$, and the mass of the daughter quark $m_q = m_c$. The lepton energy spectrum of the ACCMM model for $b \to c\,\ell\bar{\nu}_\ell$ is shown in Figure 2.10. The inclusive ACCMM spectrum of lepton energy from $b \to c \to y\,\ell\bar{\nu}_\ell$ decays is also shown in Figure 2.10.

2.4 HQET

The HQET formalism [20, 21, 8] has been developed to describe hadrons containing a heavy quark, namely a b or c quark and a light quark, u, d or s. An example of this could be the decay of a B meson to a D meson plus a lepton and neutrino. If one wants to calculate this process, the matrix element describing it must be calculated and Fermi's Golden Rule can then be used. Electroweak theory provides everything

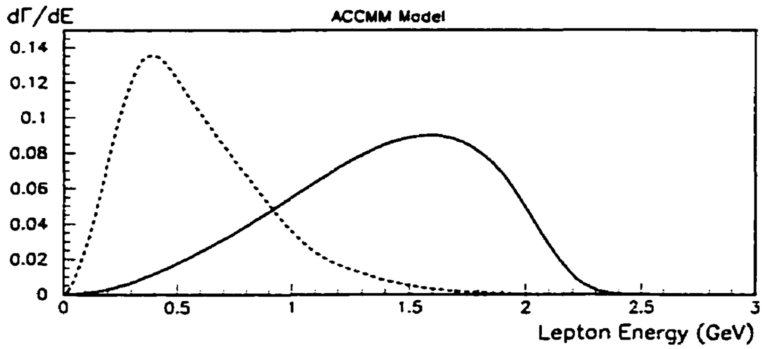

Figure 2.10: The predicted $b \rightarrow c\ell\bar{\nu}_\ell$ (solid) and $b \rightarrow c \rightarrow y\,\ell\bar{\nu}_\ell$ (dashed) lepton energy spectra for the ACCMM model. These spectra are based on the fit to the data described in Reference [19]. They have been corrected for detector acceptance and efficiencies. The spectator quark mass is taken to be $m_{\rm sp} = 150$ MeV$/c^2$. The Fermi momentum and the c quark mass are determined from the fit: $p_F = 265 \pm 25$ MeV$/c$ and $m_c = 1.670 \pm 0.025$ GeV$/c^2$.

that needs to be known about the $W\ell\bar{\nu}$ vertex. The bcW vertex is also well known apart from V_{cb}. We do not know, however, how to incorporate the light spectator quark, the u or d in this case, into the final calculation. The evolution of the light quark during this decay is described by the overlap integral of its initial and final state wave functions, but what is called the "light quark" is really a quite complicated assembly of light quark, gluons and virtual quark - anti-quark pairs. Hence, the true initial and final state wave function are very difficult or probably impossible to write down exactly.

The heavy quark in the heavy-light meson state is meant to be a quark with a mass $m_Q \gg \Lambda_{\rm QCD}$ and a Compton wavelength $\lambda_Q \sim 1/m_Q \ll 1/\Lambda_{\rm QCD}$. In this meson's rest frame it moves nonrelativistically with momentum of the order of $\Lambda_{\rm QCD}$. The scale of the typical momenta exchanged between the heavy and light constituents is set by the size of a typical hadron $R_{\rm hadron} \simeq 1/\Lambda_{\rm QCD}$. Then, the soft gluons, which keep the mesons in a bound state, are only able to resolve distances much larger than λ_Q. This means that, in the limit of $m_Q \rightarrow \infty$, the soft gluons which couple to the light degrees of freedom are not able to probe the quantum numbers of the heavy quark. In other words, the light degrees of freedom of a heavy-light meson are blind to the flavour and spin orientation of the heavy quark.

With the approximate spin-flavour symmetry highlighted by the Heavy Quark Symmetry (HQS), useful descriptions of heavy quark systems can be made. By the HQS criteria, the top, bottom, and charm quarks are heavy; and the strange, down, and up quarks are light. Hadronic systems such as the B, D, and D^* mesons can therefore be studied in the limit of HQS. As $m_Q \to \infty$, the heavy quark and the associated meson have the same velocity causing the shape and normalization of the wave function of the light degrees of freedom to be independent of the mass and the spin of the heavy quark. However, the HQS is broken by effects of the order $\Lambda_{\mathrm{QCD}}/m_Q$ because the mass of the heavy quarks are not truly infinite. HQET leads to an operator product expansion of the Lagrangian as a series of local higher dimension operators multiplied by powers of $\Lambda_{\mathrm{QCD}}/m_Q$. Consequently, the effective QCD Lagrangian in HQET is a systematic expansion and it is possible to treat the $\Lambda_{\mathrm{QCD}}/m_Q$ terms as corrections to the prediction based on the infinite mass limit.

2.4.1 ISGW 2

In a semileptonic decay, the hadronic current can be constructed from the available four-vectors, which are the velocity and spin-polarization vectors, and from Lorentz-invariant coefficients called form factors. The form factors describe the wave functions overlap of the initial and final state hadrons. In this approach, all the QCD effects are swept into the form factors. Consequently, the form factor models take advantage of the fact that the strong interactions can be isolated in the hadronic current of the semileptonic decay amplitude.

The ISGW2 [22] is a form factor model based on HQET. It is an improved version of the original ISGW model of Isgur, Scora, Grinsteins, and Wise [23]. ISGW2's calculation for semileptonic meson decays is based on a nonrelativistic constituent quark potential model, with an assumed Coulomb plus linear potential:

$$V(r) = -\frac{4\alpha_s}{3r} + c + br\,. \tag{2.10}$$

Parameter	ISGW2
b	0.18 GeV^2
c	-0.81 GeV
α_s	0.60 $\rightarrow$ 0.30
$m_u = m_d$	0.33 GeV
m_s	0.55 GeV
m_c	1.82 GeV
m_b	5.20 GeV

Table 2.1: Parameters of the constituent quark potential model ISGW2.

The quark model parameters used by ISGW2 are summarized in Table 2.1. ISGW2 incorporates the HQS constraints between the form factors and on the slopes of the form factors near zero recoil, the region where $q^2 = q^2_{max}$, q^2 being the momentum transfered. Matching requirements of HQET are also included in the ISGW2 calculations. ISGW2 is consistent with the restriction of HQS breaking at the order of $\Lambda_{\rm QCD}/m_Q$. It includes the two leading order breaking effects of HQS: the heavy quark kinematic energy which breaks the flavour symmetry, and the colour magnetic moment interaction of the heavy quark with the colour field (or chromomagnetic effects) which breaks both the spin and the flavour symmetry. Such a calculation is expected to be reliable near zero recoil where the mesons, and thus the individual quarks, have small momenta. Various relativistic corrections are included to better describe the dynamics of semileptonic decays at larger recoil.

2.4.2 Goity and Roberts Model

The model of Goity and Roberts (G&R) [24] treats soft pion emission in B semileptonic decays in the framework of the heavy quark limit. G&R then provide a description of exclusive B semileptonic decays to non-resonant and resonant hadronic states such as $\bar{B} \rightarrow D\pi\ell\bar{\nu}_\ell$ and $\bar{B} \rightarrow D^*\pi\ell\bar{\nu}_\ell$. The various effective coupling constants and the form factors are obtained using a chiral quark model and HQET. The quark contributions to the QCD Lagrangian separates naturally into two pieces: the first contribution comes from the light quarks (u, d, s) whereas the second is due to heavy

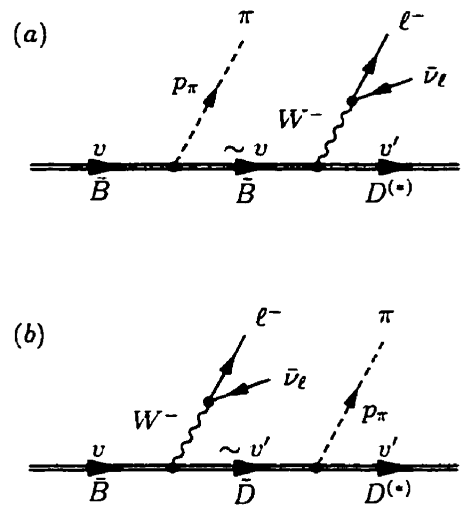

Figure 2.11: Feynman diagrams for $\bar{B} \longrightarrow D^{(*)}\pi\ell\bar{\nu}_\ell$. The dashed line represents the soft pion. The mesons $\tilde{B}$ and $\tilde{D}$ are either ground state or excited state mesons.

quarks (c, b, t). The light-quark sector has an approximate flavour chiral symmetry because the current quark masses are all very small on the typical hadron energy scale [25]. On the other hand, the dynamics of the heavy quark depend only on its velocity and are independent of its mass and spin. Hence, this model includes both the chiral symmetry of the light quarks and the heavy quark symmetry for low-energy meson interactions with the pion (called Goldstone boson in the the $\mathrm{SU}(3)_L \times \mathrm{SU}(3)_R$ flavour chiral symmetry).

The Feynman diagrams describing the process $\bar{B} \longrightarrow D^{(*)}\pi\ell\bar{\nu}_\ell$ appear in Figure 2.11. In the *G&R* model, the intermediate mesons $\tilde{B}$ and $\tilde{D}$ are either the ground state meson D, D^*, B, and B^* or the excited states D^{**} and B^{**} (J^P=1^+,2^+ states). The lowest chiral Lagrangian is expanded to the lowest order in $\mathcal{O}(p_\pi)$. The expansion places restrictions on the momentum quantum numbers of the D^{**} and B^{**}. It turns out that the well established D_1 and D_2^* states are not included in their analysis because the doublet (D_1, D_2^*) contribution appears only at higher powers of the slow pion momentum. After the expansion in p_π, the remaining states are described by a set of independent form factors. Their respective leading Isgur-Wise functions [22, 23] have an exponential form with no Λ_{QCD}/m_Q and no α_s corrections. Harmonic oscillator wave function solutions of the Coulomb plus linear potential are used to calculate the form factors. Similar work has been performed by other theorists; namely Cheng *et al.* [26] and Lee *et al.* [27]. The Goity and Roberts analysis is an improvement over previous work since it includes some of the radially excited states.

As mentioned earlier, the B semileptonic rate is far from being saturated by the resonant decays $\bar{B} \to D\ell\bar{\nu}_\ell$ and $\bar{B} \to D^*\ell\bar{\nu}_\ell$. Therefore, it is reasonable to assume that non-resonant decays $\bar{B} \to D^{(*)}\pi\ell\bar{\nu}_\ell$ may contribute to the inclusive rate. At CLEO, we employ a hybrid version of the standard G&R model to describe the non-resonant decays $\bar{B} \to D^{(*)}\pi\ell\bar{\nu}_\ell$ in generic B semileptonic Monte Carlo [28]. We do not use the G&R model of resonant decays because it does not include the exclusive semileptonic decays of the B meson to the D_1 or the D_2^* meson. The hybrid model only considers the diagram with a $\bar{B}$ (see Figure 2.11(a)) since we only care about non-resonant pion emission. Doing so removes some possibly important interference terms between the two diagrams in Figure 2.11. This approach is nevertheless believed to be adequate and corrections for interference effects are best left to future developments.

2.4.3 Isgur Model

More recently a new model of the non-resonant decay has been published [29] by Isgur, one of the authors of the original ISGW model and pioneer of the HQET. In this model he takes a new approach at solving the non-resonant decays using the Bjorken's sum rule in an "unquenched" version of the quark model. He demonstrates that in the heavy quark limit non-resonant final states should be produced at a significant rate. He then goes to calculate the individual strengths of a large number of exclusive two-body non-resonant channels. The $D\pi$ decays interesting to this analysis turn out to be only a small contribution.

The "brown muck" in heavy meson semileptonic decays is treated as a simple valence $\bar{d}$ or $\bar{u}$ antiquark confined to the heavy quark Q by including the leading effects of $q\bar{q}$ pair creation. The experimental determination of the strength and structure of these non-resonant contributions would immediately test the conclusions coming from this theory, namely that $q\bar{q}$ effects are highly suppressed in real $b \to c$ decays, that such decays extend to very high masses, and that they are highly fragmented into many small channels.

The author claims that there is a circumstantial evidence for non-resonant processes in heavy quark semileptonic decays. This theory predicts that all the non-resonant modes should account for at most 5% of the $\bar{B}$ semileptonic branching fraction. The $(D + D^{*})\pi$ contribution is approximately 0.2% of the $\bar{B}$ decay rate. This is smaller than the predicted 1% branching fraction by the Goity and Roberts model.

As mentioned, this model has been made available only very recently. We decided not to use it in the present analysis since the complete implementation of it into our Monte Carlo generator would involve major work and would require regeneration of most of our Monte Carlo. This is not feasible in the current time frame and it is also wise to let the theoretical dust settle before embarking on such an ambitious endeavour.

Chapter 3

The Experimental Setup

3.1 Overview

The data for the analysis presented here were collected at CLEO II, a general purpose detector operating at the the Cornell Electron Storage Ring. CESR started its operations in 1979. It provides electron and positron beams at an energy range corresponding to the Υ resonances ($\sim$ 10 GeV).

CESR is especially suitable for the study of B physics at the center of mass energy of 10.58 GeV, the mass of $\Upsilon(4S)$. Because of the high integrated luminosity, the CLEO II detector has collected almost 3.3×10^6 $B\bar{B}$ pairs. These make it an interesting environment to study the various B decays and more particularly semileptonic decays.

In this chapter we describe the two components of our experimental setup, CESR and CLEO, the accelerator/storage ring and the detector respectively.

3.2 The Cornell Electron Storage Ring

The Cornell Electron Storage Ring (CESR) is an electron-positron collider. It has a circumference of 768 meters, and is located on the campus of Cornell University, 14 meters below the Cornell athletic fields.

Figure 3.1 shows a simplified diagram of CESR. The figure shows the relative positioning of various accelerator components, the linear accelerator (LINAC), the synchrotron, the storage ring, and the interaction region.

3.2.1 Linear Accelerator

The first stage for the acceleration process is the linear accelerator. The linac accelerates electrons emitted from a heated filament in a 100 foot vacuum pipe. Positrons are created at an intermediate point in the linac by electrons accelerated to about 200 MeV striking a tungsten plate. Positrons are then magnetically selected from the particles emerging from the plate. The linac then accelerates positrons to about 150 MeV (electrons to about 300 MeV) for injection into the synchrotron.

3.2.2 Synchrotron

The synchrotron is a circular accelerator which is responsible for accelerating the electrons and positrons to their final energy. The particles are accelerated to the desired energy which is approximately 5.29 GeV for b quark physics. Currently there are 9 trains of bunches that are accelerated simultaneously. These are symmetrically distributed around the ring. Once the desired energies are obtained the positrons are injected into the storage ring, followed by the electrons, then both beams continue to circulate around the ring.

3.2.3 Storage Ring

The storage ring houses the two counter-rotating electron and positron beams. Each beam is composed of nine trains. The train contains either one, two or three bunches depending on the data taking period. The bunches inside each train are separated by 28 ns, while the trains are 300 ns apart.

The electron and positron beams in CESR are kept apart by electrostatic separators which have a potential difference of 25 000 Volts between the two plates. Near the CLEO interaction point, the separators are turned off, and the beams collide at a small region in CLEO. The lifetime of the beams is such that after an hour of

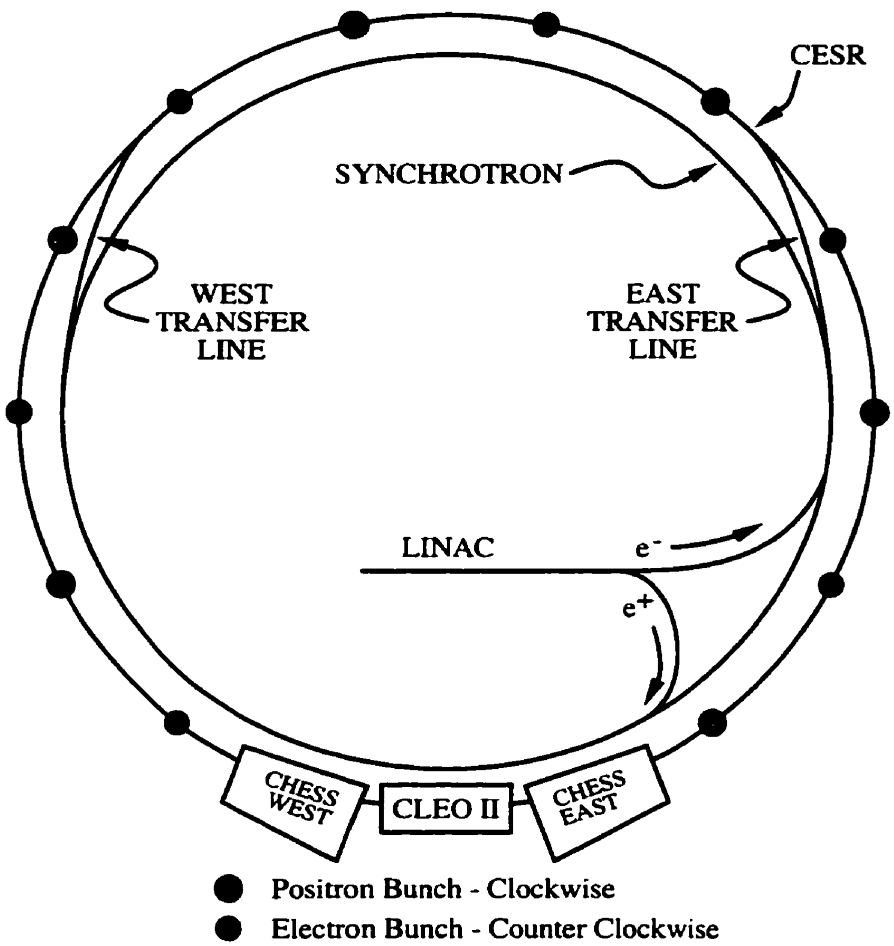

Figure 3.1: Components of the Cornell Electron Storage Ring

running time most of the beams are depleted and CESR has to be refilled in order for the experiment to continue. Energy lost to synchrotron radiation in CESR (1 MeV per particle per turn) is returned to the beams by two radio-frequency cavities located on either side of the south interaction region.

3.2.4 Interaction Region

The interaction region is where the electron and positron bunches are brought into tight focus. It is positioned to be at the center of the CLEO II detector. Once all beams are filled and properly tuned, they are allowed to collide.

3.3 The CLEO II Detector

This section is a brief description of the CLEO II detector, aimed at familiarizing the reader with the parts of the detector being used in this analysis. A detailed description of the CLEO II detector can be found in Reference [30]. The CLEO II detector was installed at CESR between the fall 1988 and spring 1989. Data taking started soon after. The CLEO II detector is a general purpose solenoidal-magnet spectrometer and calorimeter (Figure 3.2) with excellent charged particle and shower energy detection capabilities. One important point to note is that the overall symmetry of the detector is a cylindrical one. The z-axis is along the beam line and the $r - \phi$ plane describes the rotational symmetry of the various concentric detectors inside of CLEO.

The Cleo II detector is composed of layers of components, each component being designed to measure specific properties of the particles which pass through it. The objective is to combine all these individual measurements.

The detector is composed of a central barrel region and two endcap regions. The central barrel, starting from the beam pipe, is composed of three central tracking chambers: a straw tube chamber called the Precision Tracker (PT), the vertex detector (VD) and the drift chamber (DR). Outside these tracking detectors there is a Time-of-Flight System surrounded by the calorimeter. All these components are found within the magnetic field created by the superconducting Coil. Surrounding

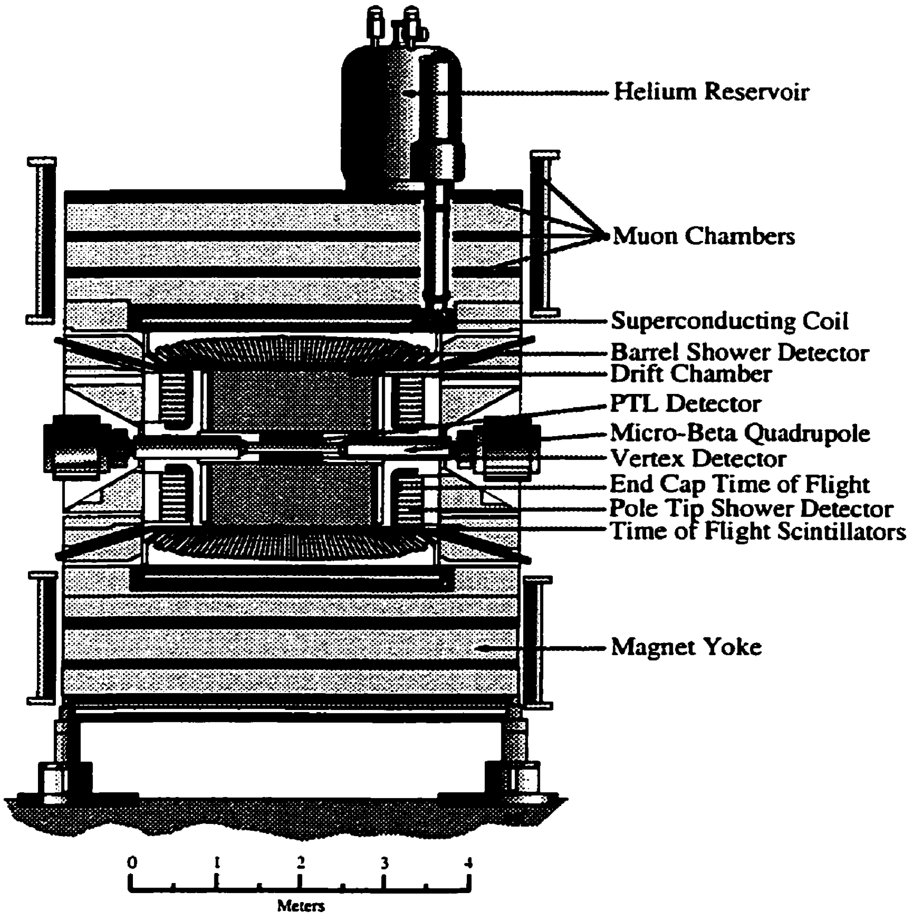

Figure 3.2: CLEO II detector side view.

all of these are the muon chambers and the magnet yoke.

The two endcap regions are composed of Time-of-Flight, crystal calorimeter and muon chambers. They are designed to give particle identification information and photon detection for small angles (15° to 36°) with respect to the beam axis. The end-view of the CLEO detector showing the endcaps is shown in Figure 3.3.

3.3.1 Precision Tracker

The Precision Tracking (PT) which extends from the beam pipe to the vertex detector, is a straw tube chamber. It is a 6 layer tube chamber, with 64 axial wires per layer. It is located within 1 cm of the 3.5 cm beam pipe. Its purpose is to measure transverse particle directions near the intersection point. No longitudinal direction measurements are made with this chamber.

3.3.2 Vertex Detector

The vertex detector (VD) is radially just outside the PT. It covers the region from 7.5 to 17.5 cm. It is a small drift chamber composed of 10 layers of small hexagonal cells as shown in Figure 3.4.

3.3.3 Drift Chamber

Beyond the VD is the 51 layer drift chamber (DR). The drift chamber extends from 17.5 cm to 95 cm. It has 12240 sense wires and 36240 field wires.

There are 40 axial or cylindrical layers which have wires parallel to the beam line and 11 stereo layers (Figure 3.5) in which the ends of the wires have a small relative displacement in azimuth transforming the layer's shape into a hyperboloid. Information in Z is obtained from these stereo layers but also from the segmented cathode surfaces which are found on the inner surface of layer 1 and the outer surface of layer 51. Axial layers measure transverse momentum, the radial distance of the closest approach to the beam line, and the azimuthal direction of tracks. Sequential layers are offset in azimuth in order to resolve left-right ambiguity in drift distance.

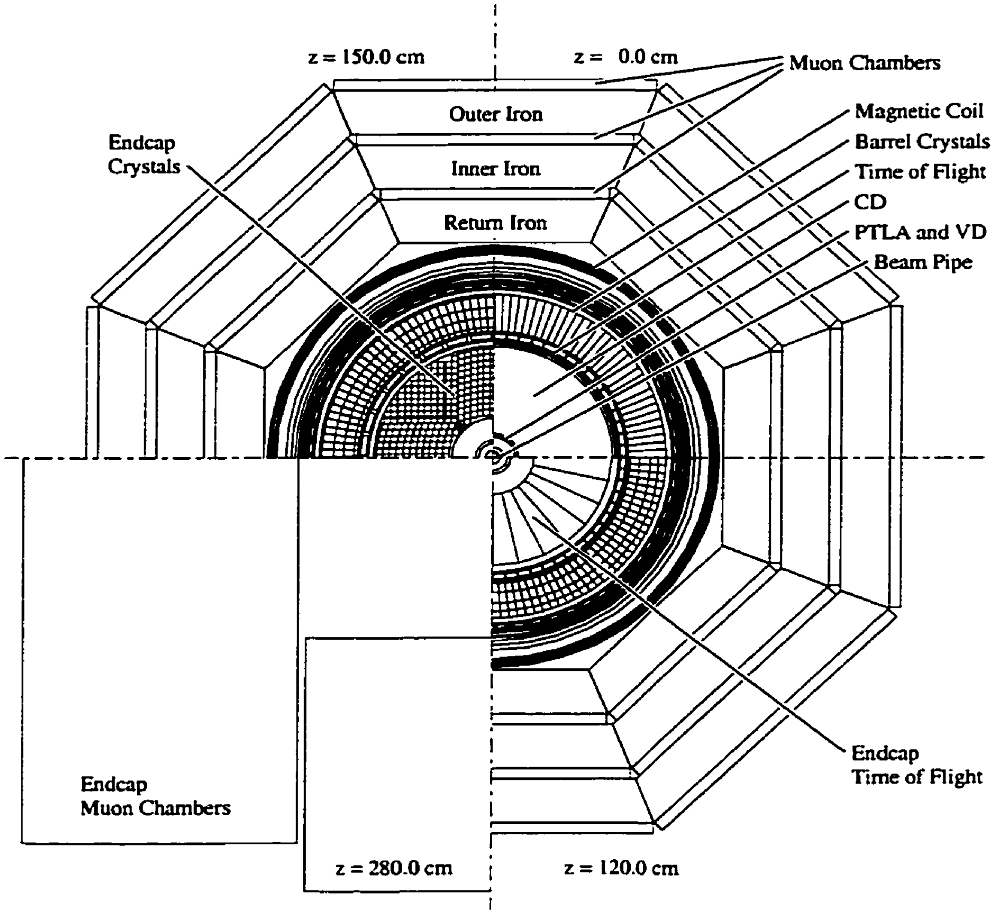

Figure 3.3: CLEO II detector end view. Each quadrant is sliced at a different depth, such as to show the structure of the endcaps.

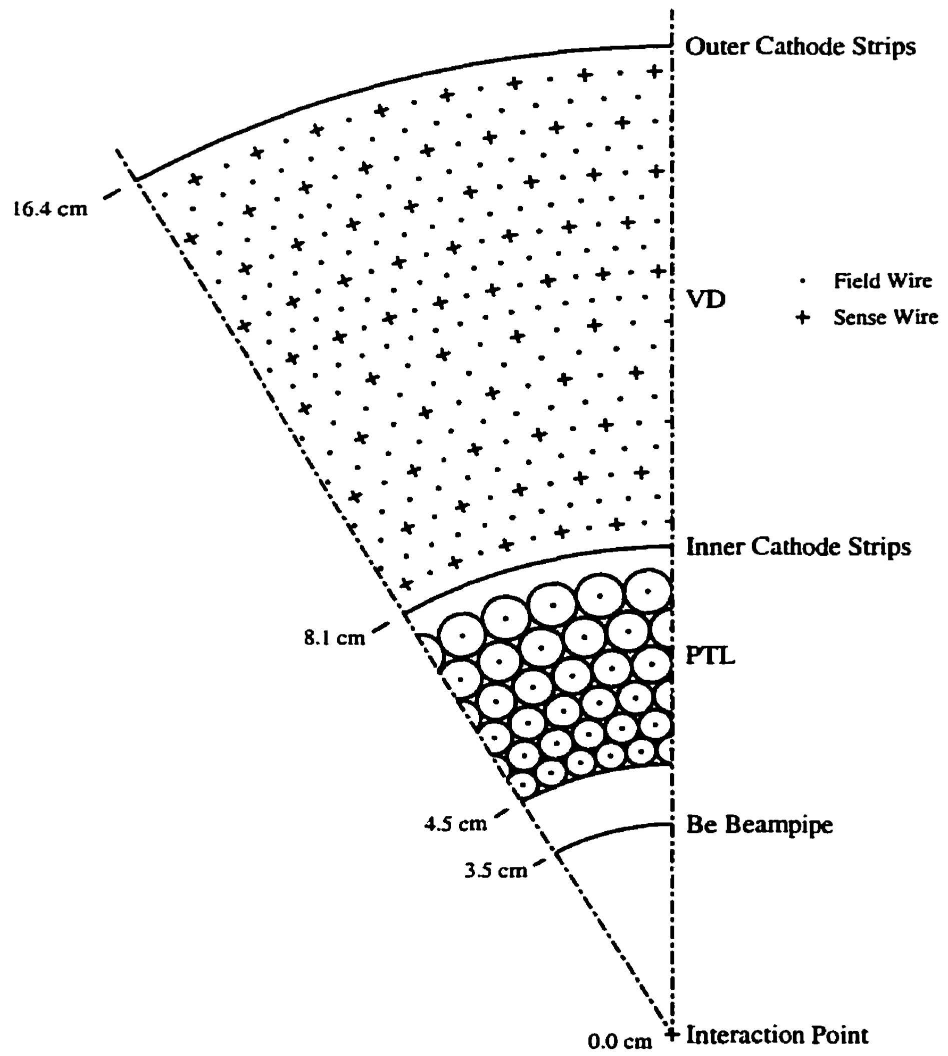

Figure 3.4: The VD/PT wires.

The gas used in the DR is composed of 50 % Argon and 50 % Ethane. The same gas mixture is being used in the VD except that a small amount of water is added there in order to reduce the amount of organic compound building up on the wires.

The central drift chamber measures a charged particles momentum and its specific ionization ($\frac{dE}{dx}$) which is used for particle identification. To measure the momentum vector of charged particles, the data from all three chambers are combined.

Track reconstruction programs are used to find charged particle tracks in an event. The patterns of hits on wires are identified from the signal left by the ionized gas molecules in the detector. These hits are then fitted using the Billoir Filter to obtain the trajectory of the original particle.

Two major factors limit the momentum resolution: multiple scattering and the position resolution of the track. Multiple scattering dominates the resolution at low momentum, ant the position resolution dominates at high momentum, where the track curvature is small.

The transverse momentum resolution on charged tracks as measured by the central drift chambers is $(\sigma p_\perp/p_\perp)^2 = (0.0015 p_\perp)^2 + (0.005)^2$, where $p_\perp$ is measured in GeV/c.

3.3.4 Time-of-Flight

Outside the DR is the barrel Time-of-Flight (ToF) system which provides additional particle identification information and serves for offline cosmic ray rejection.

The barrel Time-of-Flight system is composed of 64 scintillators forming a cylinder around the outside of the DR. The readout is performed on both ends using photomultiplier tubes.

Each endcap has 28 wedge-shaped scintillators which are arranged in a circular pattern.

The velocity of a particle can be determined from the timing obtained from the beam crossing and the time at which the particle is detected in the scintillator. Using the velocity and the particle's momentum one can derive its mass.

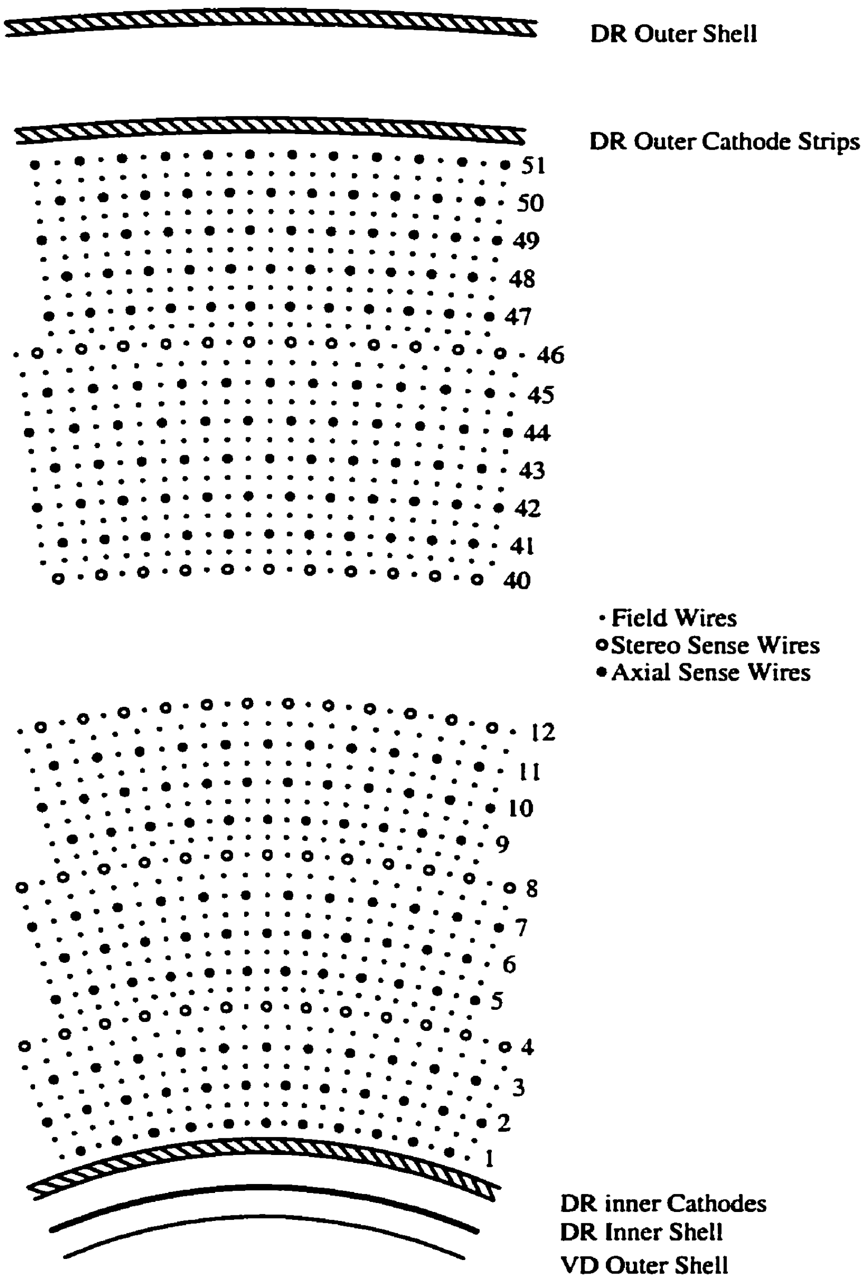

Figure 3.5: The DR wires.

3.3.5 Crystal Calorimeter

Outside the ToF is the crystal calorimeter (CC). It has high efficiency, fine segmentation, and excellent energy resolution. It consists of 7800 thallium-doped cesium iodide scintillating crystals. 6144 of these are in the central barrel and 828 are in each endcap. Overall, 95% of the total solid angle is covered.

Charged particles or photons will produce electromagnetic showers upon striking these crystals. The energy of the showers is converted into light which is detected by photodiodes placed at the end of the crystal.

The good barrel region of the calorimeter is where we have the best shower detection. It is found between angles 32° and 135°, where the angle is between the beam axis and the shower position. The resolution on the energy in this region is given by $(\sigma E/E)(\%) = 0.35/E^{0.75} + 1.9 - 0.1E$ (where E is in GeV), which represents a resolution of 1.5% at 5 GeV and 3.8% at 100 MeV. The angular resolution in the barrel is given by $\sigma_\phi(mrad) = 2.8/\sqrt{(E)} + 1.9$, $\sigma_\theta(mrad) = 0.8\sigma_\phi sin(\theta)$. This corresponds to an angular resolution of 3 mrad at 5 GeV and 11 mrad at 100 MeV.

The endcap as seen in Figure 3.3 has a circular configuration. It overlaps with the barrel region within the polar angle 32° and 36°. The resolution here is given by $\sigma E/E(\%) = 0.26/E + 2.5$. This corresponds to 2.6% at 5 GeV and 5.0% at 100 MeV. Angular resolution is correspondingly slightly worse than in the barrel region and is quoted at 9 mrad at 5 GeV and 19 mrad at 100 MeV.

3.3.6 Superconducting Magnet

The drift chambers, ToF, and crystal calorimeter are placed within a 1.5 Tesla superconducting magnet. The coil of the magnet is cooled down by 4 K liquid Helium. The magnetic field is parallel to the beam axis and is used to bend the charged particles in the $r - \phi$ plane. The curvature of a charged particle trajectory within the magnetic field is used to determine the particle's momentum.

3.3.7 Muon Chambers

Outside the superconducting magnet surrounding the whole inner detector sits the muon chambers and the iron used as the return yoke for the superconducting magnets. Iron plates used for magnetic return yoke are shared with the Muon Identification system (MU). Outside of each return yoke layer is a set of gaseous tracking chambers used for muon identification.

The barrel muon chambers are composed of three layers of wire chambers. Each layer consists of 8 planar chambers in an octagonal arrangement.

The endcap muon chambers cover the front and end region of CLEO. These are rectangular wire chambers. They allow for muon identification down to polar angles of 30°.

Because muons are the least reactive long-lived particle, they have the greatest penetration depth, therefore any track which penetrates all three layers is identified as a muon.

3.4 Trigger and Data Acquisition

While running the CLEO II detector collects a great amount of raw data. This data has to be digitized, collected, analyzed and converted into physics results. Computers play a major role during every stage of this data acquisition process (DAQ). Before all of this processing of the collected data can start we have to select the interesting events from the massive raw amount of data that are produced during the e^+e^- collisions. The DAQ system processes the electronic signals from the detector elements in a temporary storage medium called a buffer, reduces the data rate to a manageable level and then records the events of interest on a permanent storage medium. It is also designed to monitor the detector's performance. During the storage of the event into the buffer, there are trigger processors which perform some rapid but crude pattern recognition algorithms to select events of interest. A certain fraction of events is designed for calibration purposes and the major part for physics analysis.

The rate of electron and positron collisions in CESR is 3.6 MHz. This is far too fast to be accommodated by the data storage and data analysis components of CLEO. The fortunate thing is that most of these events are not interesting for the type of physics we are investigating. The actual rate of interesting annihilations is of the order of a few Hertz and hence much more manageable. CLEO II uses a hierarchical three-level trigger system; the three stages are called Level 0 (L0), Level 1 (L1), and Level 2 (L2). An additional software filter, called Level 3 (L3), is applied before data storage.

The L0 trigger is the first link of the DAQ system. It is designed to make fast and efficient decisions about whether or not charged and neutral particles have been produced in CLEO II. Because the L0 trigger system is confronted with the highest data rates, it uses information from a fraction of the detector channels. The L0 trigger receives input from the ToF scintillators, the VD tracking chamber, and the CC calorimeter. The ToF is the fastest device in CLEO II; the signals from the phototubes are ready in about 55 ns. The L0 criteria reduce the crossing frequency to a rate on the order of 10 kHz. Whenever any of the L0 requirements are met (see Reference [31] for more details), all gates to the detectors are disabled and the L1 trigger is initiated.

The L1 trigger takes more information from the detector and uses it to make better informed decisions about the event. It uses information from the ToF, VD, DR, and the CC. Typically, L0 and L1 require a few microseconds to eliminate uninteresting events. Overall the L0 and L1 requirements reduce the trigger rate to about 50 Hz.

Higher level triggers face much lower rates and perform more sophisticated event rejection algorithms. The L2 trigger uses more detailed tracking information and reduces the overall read-out rate by another factor of two. An accept flag at the Level 2 forces the detector signals to be sent to the L3 software filter. The L3 filter reduces the rate by 30% to 40%, depending on beam conditions. Events that pass the L3 requirement are then stored permanently on magnetic tapes for data reconstruction. The overall CLEO II trigger efficiency for $B\bar{B}$ events is 99.8%.

An accept signal from the L2 trigger allows CLEO to be read-out. CLEO is read-out in a common stop mode. The closing gate is set by CESR after each beam crossing. The actual data acquisition system can currently read events at 50 Hz with a 10% deadtime [32]. This means that the readout of the front-end electronics for each detector component is completed within 2 ms. To reduce the amount of data read out after a trigger, each of the electronic signals has to pass certain cuts (this process is called data sparsification) before they are sent to a buffer. The digitization of the entire CLEO II detector takes about 2.2 ms, and the digitization and sparsification take about 13.5 ms. The event size of a typical hadronic event is about 8 kbytes, which, given a 25 Hz triggering rate, requires a bandwidth of 200 kbytes/sec.

Online, a set of control and monitoring computers provides a user interface for the detector supervisors and ensures that the detector is performing correctly. Offline, diagnostic programs are used to monitor and calibrate the CLEO II sub-detectors. Bhabha and muon pair events are recorded online for calibration purposes. The L2 trigger has the capability to prescale these events by accepting only a predetermined fraction of two-track triggers. After calibration, the data stored on magnetic tapes are processed with the reconstruction program PASS2. The task of PASS2 is to transform the raw information (hits and clusters) into quantities required for physics analysis. The data processed and compressed with the program PASS2 are stored permanently on disk for later physics analysis.

Chapter 4

Event Selection Optimization

To distinguish the particular B meson decay channel we are interested in from events which mimic the signal, a series of event selection criteria were chosen. This chapter explains these criteria and the reasoning behind their selection. First we describe briefly our data sample. The second section describes the Monte Carlo event simulation and different data sets that were used. In the third section we give some details about how the selection rules were optimized. This is followed by a description of some global criteria for hadronic event selection. In the next six sections we describe how tracks were selected inside of an event and how the different particle hypotheses were applied. Once the charged tracks are selected and combined together we describe in the remaining section how we reconstruct the neutrino - it cannot be detected directly and must be inferred from all the tracks contained in the event. We also describe the criteria that allow us to select the best neutrinos.

4.1 Data Sample

For this analysis we use the complete CLEO II data sample. This data has been accumulated over a period of several years, starting in November 1990 up to April 1995. The total luminosity of this sample is 3.1 fb^{-1} on the $\Upsilon(4S)$ resonance (ON Resonance) corresponding to 3.27×10^6 $\Upsilon(4S) \rightarrow B\bar{B}$ events and 1.6 fb^{-1} taken $\sim$ 55 MeV below the $\Upsilon(4S)$ resonance (OFF Resonance). Over these years slightly different conditions have motivated the subdivision of this data set into smaller subsets. These have been conveniently labeled 4S2 through 4SG. They are summarized in Table 4.1 along with the approximate data taking period. These small changes are reflected in the Monte Carlo simulation of the detector. Over time, data taking remained fairly stable, meaning that there were no major hardware changes, but the process of calibrating the data for use for the various analysis evolved and better techniques were developed over the data taking period. In an effort to make uniform the data reconstruction as well as our Monte Carlo sample, the whole data set has been reprocessed to take into account our accumulated knowledge of the detector. Further improvements were a better set of drift functions as well as a better calibration of the timing information (t0's). A new track fitting method has been adopted, the Billoir Fitter, which required an extra tuning of corresponding weights. The geometry and the alignment of the various detector components have been readjusted. Overall, this reprocessed data set, emerged as what we call the recompress data. It is the one used for the present analysis.

4.2 Monte Carlo Samples

Events generated by Monte Carlo simulations of signal and background decay processes were used to understand the kinematics of these decays and to determine the optimal selection criteria. These Monte Carlo event samples are useful because it is relatively easy to generate a very large sample of any kind of decay process. These large Monte Carlo event samples make it possible to compare different selection criteria in a statistically meaningful way. In addition, since the exact decay process of a Monte Carlo event is known, it is possible to determine what processes form the dominant expected background and then find selection criteria to remove them.

The generation of Monte Carlo events has two phases. The first is to randomly generate a decay process. This entails choosing which daughter particles an unstable particle decays into as well as assigning momenta to those children. The program used by the CLEO collaboration for this first step is called QQ. The second step is to simulate the propagation of the children through the CLEO II detector. For this

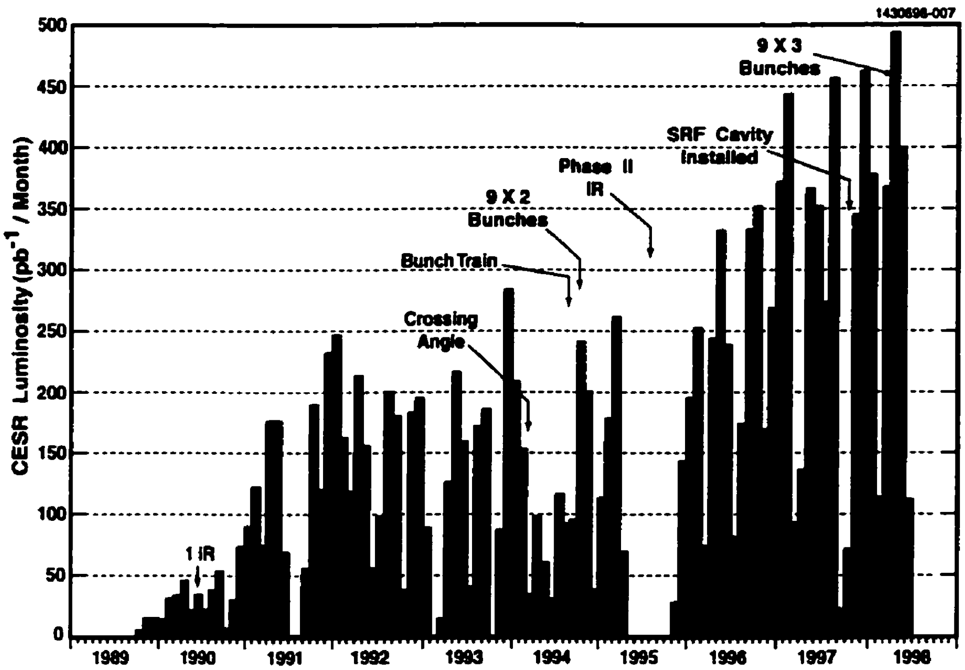

Figure 4.1: Integrated plot of monthly luminosities for the CLEO II and CLEO II.V experiments.

Data Set	Date of Data Collection	Luminosity (pb^{-1}) ON $\Upsilon(4S)$	OFF $\Upsilon(4S)$
4S2	Nov. 90 - Jun. 91	462	197
4S3	Sep. 91 - Feb. 92	436	209
4S4	Apr. 92 - May. 92	214	101
4S5	Jul. 92 - Oct. 92	216	105
4S6	Nov. 92 - Jan. 93	232	85
4S7	Mar. 93 - Jul. 93	285	177
4S8	Aug. 93 - Sep. 93	188	94
4S9	Nov. 93 - Jan. 94	230	117
4SA	Jan. 94 - Feb. 94	138	54
4SB	Mar. 94 - May. 94	85	64
4SC	Jun. 94 - Aug. 94	115	36
4SD	Sep. 94 - Oct. 94	53	50
4SE	Oct. 94 - Nov. 94	71	62
4SF	Nov. 94 - Nov. 94	89	66
4SG	Jan. 95 - Apr. 95	293	192
Total Luminosity		3107	1609

Table 4.1: Data sets summary.

second step we used the GEANT [33] based CLEOG program. CLEOG attempts to mimic the CLEO II detector's response to particles by simulating the physics of the particle detector interaction. Much effort has been expended by the CLEO collaboration to make CLEOG as accurate as possible.

To model the signal events and the various backgrounds, several MC samples were generated. The first sample consists of approximately 16×10^6 generic $B\bar{B}$ events. The second sample is the signal MC data set. It consists of 10^4 events where the B^- decays into the channel we are investigating. Also a sample of 5.2×10^6 continuum events was used to study the event type selection rules.

The generic $B\bar{B}$ MC sample corresponds approximately to 5 times the size of the actual data $B\bar{B}$ sample. The generic decay of the B meson is handled by a decay table which contains the measured and expected branching fractions of the exclusive hadronic, leptonic and semileptonic decay modes of the B meson. The simulation of the semileptonic decays of the B meson relies on the ISGW2 [22] and the G&R hybrid models as described in Chapter 2. The MC generator EvT takes into account the angular correlation among the decay products, which provides an accurate description of the decay dynamics of the semileptonic decay of a B meson. The various B, D and resonant D masses used for this analysis are listed in Table 4.2. The B semileptonic branching fractions used in the generic $B\bar{B}$ MC are listed in Table 4.3. The non-resonant (NR) as well as the higher D^{**} excitations were chosen according to current predictions and such as they saturate the inclusive semileptonic rate, $B_{SL} = 10.18\%$.

The signal MC sample was generated to measure the signal detection efficiency. This sample contains 10^4 events where $B^- \longrightarrow D^+\pi^-e^-\bar{\nu}_e$ and $D^+ \longrightarrow K^-\pi^+\pi^+$. As in the case of the first sample this decay is modeled using the G&R model. The other B in the event is allowed to decay generically and is modeled in the same way as in the first sample.

4.3 Selection Criteria Optimization

During the investigation of $D\pi$ production in B semileptonic decays, we want to select the best criteria which are as efficient as possible for accepting our signal, while retaining good rejection power for the various backgrounds. In this analysis, we mainly use our $B\bar{B}$ Monte Carlo and continuum samples to optimize the statistical significance of the signal observation. Some of the cuts used are solely based on expectations for the physics of a semileptonic B decay, and others rely on the calculations of a figure of merit (F) which maximizes signal over background. We define

$$F = \frac{S^2}{S+B}, \tag{4.1}$$

where S is the number of reconstructed signal events and B is the number of non-signal events which pass the selection cut(s) under study.

When a specific process is not well modeled by our Monte Carlo sample, sideband or wrong sign samples turn out to be reliable tools for modeling combinatorial backgrounds and optimizing their rejection. No optimization has ever been performed on data that could contain real signal events.

After carefully studying the $B\bar{B}$ Monte Carlo and continuum events, we were able to divide the backgrounds in this analysis into several well-defined components.

Charm Mesons			
Hadron Symbol	Quark Content	Mass (GeV/c^2)	$n\ ^{2S+1}L_J$
D^+	$c\bar{d}$	1.869	$1\ ^1S_0$
D^0	$c\bar{u}$	1.865	$1\ ^1S_0$
D^{*+}	$c\bar{d}$	2.010	$1\ ^3S_1$
D^{*0}	$c\bar{u}$	2.008	$1\ ^3S_1$
D_1^0	$c\bar{u}$	2.422	$1\ ^1P_1$
D_0^{*0}	$c\bar{u}$	$\sim$2.360	$1\ ^3P_0$
D_1^{*0}	$c\bar{u}$	$\sim$2.420	$1\ ^3P_1$
D_2^{*0}	$c\bar{u}$	2.459	$1\ ^3P_2$
D'	$c\bar{u}$	$\sim$2.580	$2\ ^1S_0$
$D^{*\prime}$	$c\bar{u}$	$\sim$2.640	$2\ ^3S_1$

Bottom Mesons			
Hadron Symbol	Quark Content	Mass (GeV/c^2)	$n\ ^{2S+1}L_J$
B^-	$b\bar{u}$	5.279	$1\ ^1S_0$
$\bar{B}^0$	$b\bar{d}$	5.279	$1\ ^1S_0$

Table 4.2: In this table, the principal non-strange charm and bottom mesons are listed, along with their quark composition, masses, and quantum numbers. Each meson listed has its antiparticle with the opposite quark content. The mass values are taken from the Particle Data Group compilation [1]. Only the mesons of interest in this thesis are listed. The broad states (D_0^{*0}, D_1^{*0}) and ($D', D^{*\prime}$) have not yet been observed directly and the masses given are theoretical predictions based on heavy-light spectroscopy.

State	Decay Mode	Assumed $\mathcal{B}$ (%)
$1\,^1S_0$	$\bar{B} \to D\ell\bar{\nu}_\ell$	2.00
$1\,^3S_1$	$\bar{B} \to D^*\ell\bar{\nu}_\ell$	5.40
$1\,^1P_1$	$\bar{B} \to D_1\ell\bar{\nu}_\ell$	0.66
$1\,^3P_2$	$\bar{B} \to D_2^*\ell\bar{\nu}_\ell$	0.33
$1\,^3P_1$	$\bar{B} \to D_0^*\ell\bar{\nu}_\ell$	0.11
$1\,^3P_0$	$\bar{B} \to D_1^*\ell\bar{\nu}_\ell$	0.11
$2\,^1S_0$	$\bar{B} \to D'\ell\bar{\nu}_\ell$	0.02
$2\,^3S_1$	$\bar{B} \to D^{*\prime}\ell\bar{\nu}_\ell$	0.22
NR	$\bar{B} \to D\pi\ell\bar{\nu}_\ell$	0.50
NR	$\bar{B} \to D^*\pi\ell\bar{\nu}_\ell$	0.70

Table 4.3: Assumed branching fractions for the exclusive semileptonic decays of the B meson in generic $B\bar{B}$ MC. The non-resonant contribution states are label by NR.

We also give our strategy to handle these backgrounds:

- The main background comes from mis-reconstructed D^+ mesons. This is the case where we either mis-identify a Kaon or a Pion, or actually combine three incorrect particles which still satisfy all the selection criteria for a D^+ meson. This type of background is best treated with a sideband subtraction and it will be explained in greater detail in Sections 5.2.3 and 5.3.1.

- The second background in importance comes from events that contain real D^+ mesons and a real e^- lepton but either lose a pion or select a wrong pion from the other B. These events are mostly other types of semileptonic events. This type of background can be classified by two different contributions, the uncorrelated backgrounds (background from events in which the $D^+\pi^-$ comes from the $\bar{B}$ and the lepton from the B) and correlated backgrounds (background from events in which $B^- \to D^+\pi^-e^-\bar{\nu}_e$ and the other B decays generically). In the uncorrelated type of background, the lepton comes from a cascade decay $\bar{b} \to \bar{c} \to \ell^-$ from the second B meson in the event. In the correlated type of backgrounds a real $D^+\pi^-\ell^-$ is produced and hence can mimic our signal.

- The third background that we must consider in our analysis is the continuum

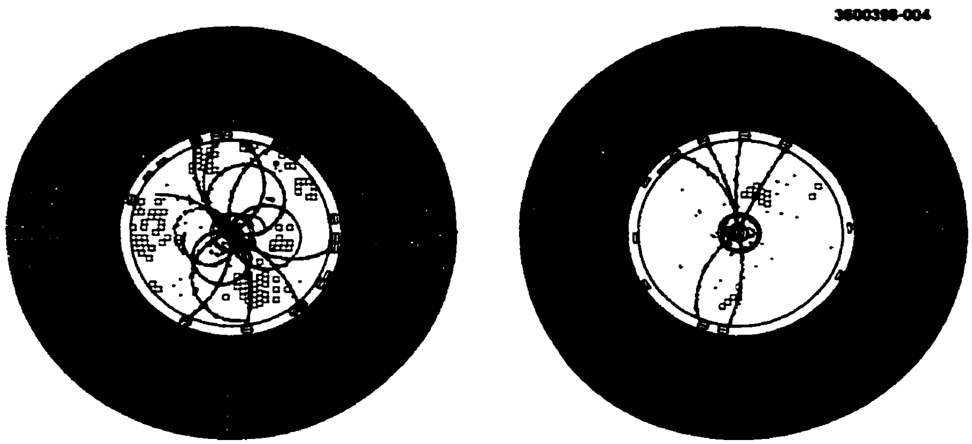

Figure 4.2: CLEO display of typical events. On the left we have one $B\bar{B}$ event and a continuum event on the right.

background (or non-$B\bar{B}$ background). This background is modeled by measuring the signal yield using OFF Resonance data.

- Another background arises from fake leptons. The fake lepton background is the contribution in which a $D^+\pi^-$ is paired with a hadron misidentified as a lepton. This contribution is estimated by performing an analysis where non-leptons are treated as leptons and the result re-normalized using known estimates of the fake rates.

4.4 Global Event Shape Criteria

We are in the presence of a 3 to 1 dominance of continuum data under $B\bar{B}$ events. It is important that we restrict ourself to the selection of the latter events. In Figure 4.2 we can see the major difference between $B\bar{B}$ events which tend to have decay particles more uniformly distributed and continuum events which are more jet-like in distribution. To restrict our samples to only consider $B\bar{B}$ events we use two important criteria to reject continuum events. The first is an event class cut (called KLASGL) and the second an event shape cut (called R2GL).

An event is classified as a possible hadronic final state according to KLASGL if the following requirements are met.

- The event must contain a minimum of three charged tracks.
- The total visible energy in the event must be greater than 15% of the total center-of-mass energy.
- The energy observed in the calorimeter has to be between 15% and 90% of the total center-of-mass energy.
- The location of the primary vertex for the event must be within $\pm$ 2 cm and $\pm$ 5 cm of the beam spot in the $r-\phi$ plane and z-direction respectively.

To further reduce non-$B\bar{B}$ background, each event is required to satisfy the ratio of Fox-Wolfram [34] moments. The Fox-Wolfram moment H_i is given by

$$H_i = \sum_a \sum_b \frac{|\vec{p}_a||\vec{p}_b|}{E_{cm}^2} P_i(\cos\phi_{ab}), \tag{4.2}$$

where P_i is the ith Legendre polynomial with respect to the angle ϕ between the two particles a and b. All legitimate charged tracks and calorimeter showers (as determined by `TMNG` and `SPLITF` defined below) are used in the sum. We then use the ratio of Fox-Wolfram moments $R_2 \equiv H_2/H_0$. R_2 is a measure of the isotropy of the momentum distribution. The smaller the value of R_2, the more isotropic the event. The R_2 parameter is then very useful for distinguishing $B\bar{B}$ events, which tend to be isotropic, from continuum events, which tend to be more jet-like. The distributions of R_2 for $B\bar{B}$ and continuum events are shown in Figure 4.3. We select events with $R_2 < 0.4$ for this analysis. This requirement is 98.0% efficient for the signal mode, and 65.5% efficient for generic continuum events.

4.5 Track Selection

Charged particle detection is crucial in the present analysis. In Appendix C, we give a description of the CLEO variables used for track selection. All charged tracks must meet the following criteria.

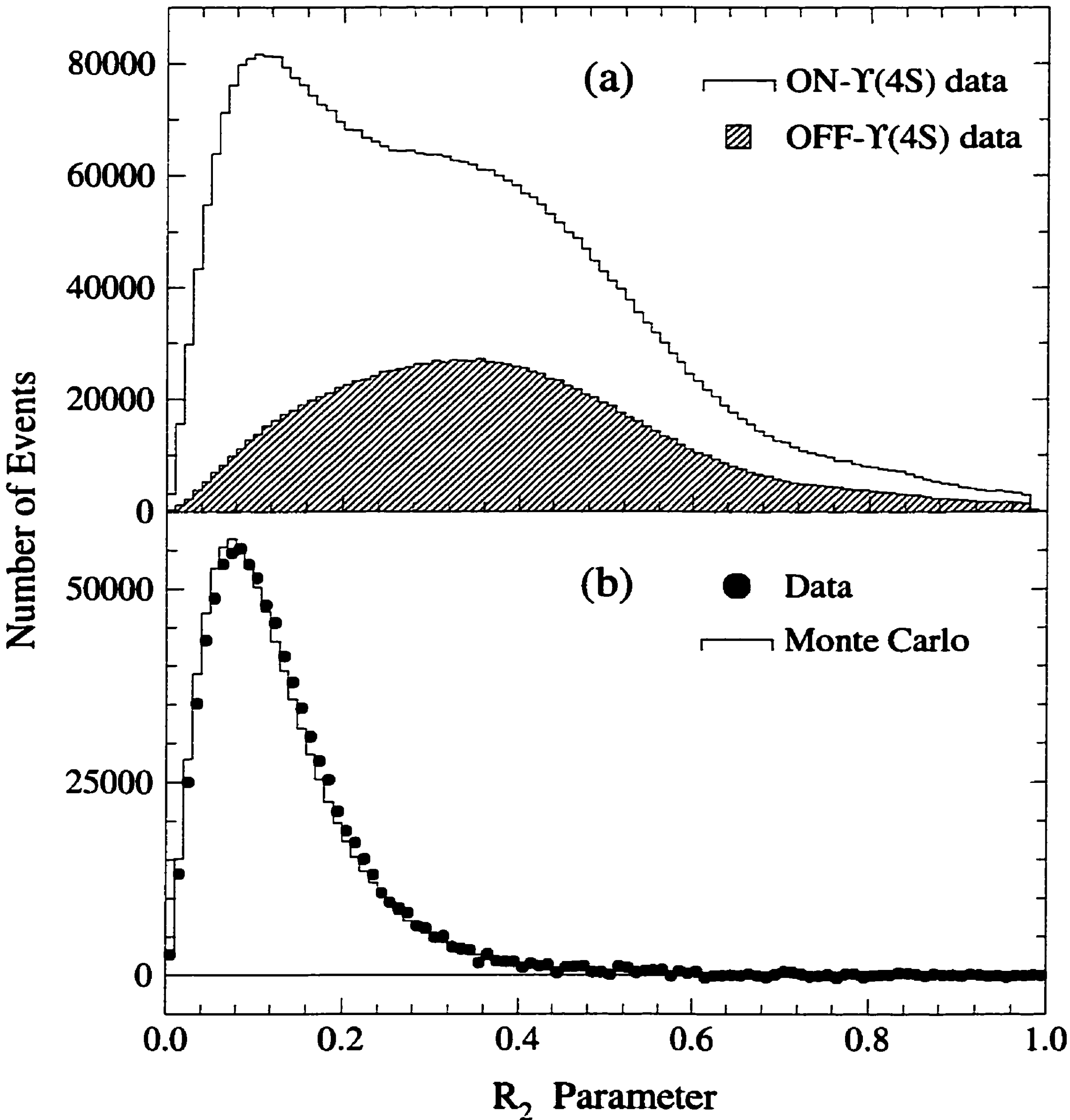

Figure 4.3: The R_2 distribution in data and MC simulation: (a) R_2 distributions derived from ON Resonance data (unshaded) and OFF Resonance data (shaded). (b) R_2 distribution of $\Upsilon(4S) \rightarrow B\bar{B}$ decays derived after scaled continuum subtraction (data points). The superimposed histogram shows the same distribution derived from generic $B\bar{B}$ MC simulation. We require $R_2 < 0.4$. Source [35].

- The track must be in the fiducial volume of the drift chambers: $|\cos\theta| < 0.92$. The angle θ is the angle of the track with respect to the beam line.

- The track must originate from the vicinity of the e^+e^- interaction point. We require: DBCD $<$ 5 mm and Z0CD $<$ 5 cm and KINCD $=$ 0. The impact parameters DBCD and Z0CD are measured in the $r - \phi$ plane and along the z-direction respectively. The vertex flag KINCD $=$ 0 selects tracks from the primary vertex.

- The track must pass the `TMNG` requirements [36, 37, 38]. The software package `TMNG` eliminates spurious ghost pairs, curlers, back splash, and scattered tracks[1].

- The track must have good dE/dx information.

- Two conditions on the global track selection are used to get rid of badly reconstructed tracks. Tracks tagged as Dredge or Z-escape by the reconstruction algorithm are now rejected. Dredge is just another term for badly reconstructed track in the CLEO jargon, while Z-escape describes a track which has no z-information.

All particles, not just photons, deposit energy in the calorimeter. We need to separate the photon showers from those created by other particles. From the energy deposited in the calorimeter and from the matching algorithm between calorimeter showers and charged tracks we are able to accomplish this quite accurately since photons do not leave tracks in the tracking chambers. The main algorithm for crystal shower reconstruction [39] is used to get rid of fake photons. This is especially important for this analysis as will be explained in the section on neutrino reconstruction.

[1] A ghost pair is made of two tracks fitted to the same set of hits. A track with insufficient momentum to reach the outer edge of the main drift chamber may spiral many times in the tracking chambers. Multiple tracks formed from the spirals are called curlers. A track with enough momentum can exit the main drift chamber, enter the calorimeter, lose energy and reenter the drift chambers. Such tracks are called back splash. Occasionally, a particle will scatter in the material of the detector and kink. Sometimes it will interact with the material and might create many other charged particles. Some other times it may simply decay in flight. In each of these three latter cases, one or several tracks may intersect the point of scatter or decay: such tracks are classified as scattered tracks. The role of `TMNG` is to map a set of hits to only one track.

This algorithm is not perfect though and special care needs to be taken for showers not associated with hadronic tracks yet in the vicinity of some charged tracks. Most of these special showers are produced from hadronic split offs. Particles associated with charged tracks interact with the material inside of the detector and produce some extra photons that are not found in the near vicinity of these charged tracks shower clusters. These extra crystal showers would be identified as photons instead of being associated with the charged track if we were not careful enough.

We try to perform a shower-shower matching based on the distribution of energy within a cluster. This is accomplished with the `SPLITF` algorithm [40, 36]. `SPLITF` makes use of neural nets to distinguish split offs from photons. A neural net is an approach to the problem of using many different variables to separate two types of objects, in our case real photons from hadronic split offs. Each shower that is associated with a charged track is considered as a possible parent shower, and every other shower is considered as a possible split off shower. Several variables are defined for a candidate parent-split off pair and the net is then trained on Monte Carlo samples of the two different objects, so it can devise the most optimal way of weighting these input variables. Finally one output variable is generated which ranges from -1 to 1. The final requirement chosen on that variable to separate split offs and photons depends on the energy of the split off candidate, its angle of separation from the parent shower, and whether the shower is in the barrel or the end cap.

The `SPLITF` rejection removes about half of the remaining hadronic energy of calorimeter showers that are not matched to tracks by our main crystal shower reconstruction algorithm, while removing only about 2% of the photon energy [40].

4.6 Lepton Identification

The identification of leptons is essential to our analysis. At the $\Upsilon(4S)$, the detection of a fast lepton strongly suggests the presence of a B semileptonic decay. Electrons and muons produce very distinctive signatures in the CLEO II detector through their characteristic interactions with matter. The electrons and the muons leave tracks in the drift chambers and their charges and momenta are calculated from the curvature

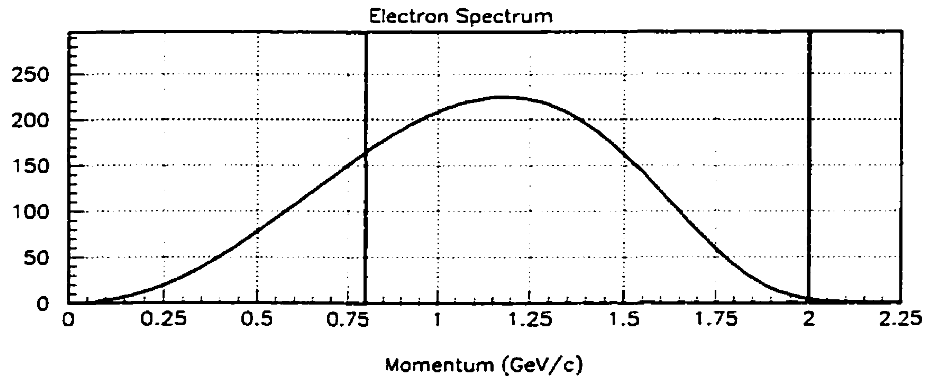

Figure 4.4: Electron momentum distribution from the Goity & Roberts model.

of these tracks. The electrons deposit essentially all their energy in the CsI calorimeter while the muons leave trails in the muon chambers.

Any track passing all the above cuts and having a momentum above 0.6 GeV/c is counted as an electron.

For the lepton counting process, tracks identified as muons are required to have a $DPTHMU \geq 3$ (defined below) and a momentum above 1.0 GeV/c.

The analysis is based on the neutrino reconstruction technique [40, 41]. We therefore demand one lepton per event, since any extra lepton would likely be accompanied by an extra neutrino. This extra neutrino would then complicate the use of energy-momentum constraint and hence make it impossible to reconstruct the neutrino momentum accurately.

When all counting is done we require only one lepton in the event, but more specifically, we keep only events with one electron in the following momentum range (see Figure 4.4):

$$0.8 \text{ GeV/c} < |\vec{P}_\ell| < 2.0 \text{ GeV/c} \tag{4.3}$$

The lower limit is chosen so as to reduce contamination from secondary leptons from charm decay and the upper limit is obtained from phase space saturation.

Lengthy studies were done to optimize these cuts.

4.6.1 Electron Identification

Electron identification relies primarily upon several independent measured quantities [42]:

E/p The most sensitive variable for identifying electrons is the ratio of the energy (E) deposited in the calorimeter to the momentum ($p \equiv |\mathbf{p}|$) of the track pointing to the cluster. The quantity E/p is close to one for electrons, and smaller for all other charged particles. The discrimination of electrons from hadrons or muons from the ratio E/p is illustrated in Figure 4.5.

dE/dx The specific ionization (dE/dx) measured in the drift chambers is also a powerful piece of information for identifying electrons (see Figure 4.7). The difference between the measured and the predicted ionization loss for an electron peaks at zero, whereas the hadron response is shifted lower by about two standard deviations.

Track match Another quantity useful in electron identification is the distance between the projection of the track and the calorimeter shower. A matching requirement between the track and the shower provides good discrimination between electrons and other neutral and charged particles.

Cluster shape The last quantity used for electron detection is the shape of the shower. Electromagnetic showers tend to deposit all their energy in a few crystals very close to the center of the cluster. We use variables which measure the lateral development of the shower to distinguish electrons from hadrons.

For studying efficiencies and rejections rates, distributions for each of these variables are made for electrons and non-electrons separately. The electron sample comes from embedding radiative Bhabha events into hadronic events where the event topology is close to that for an electron from B semileptonic decays. The non-electron

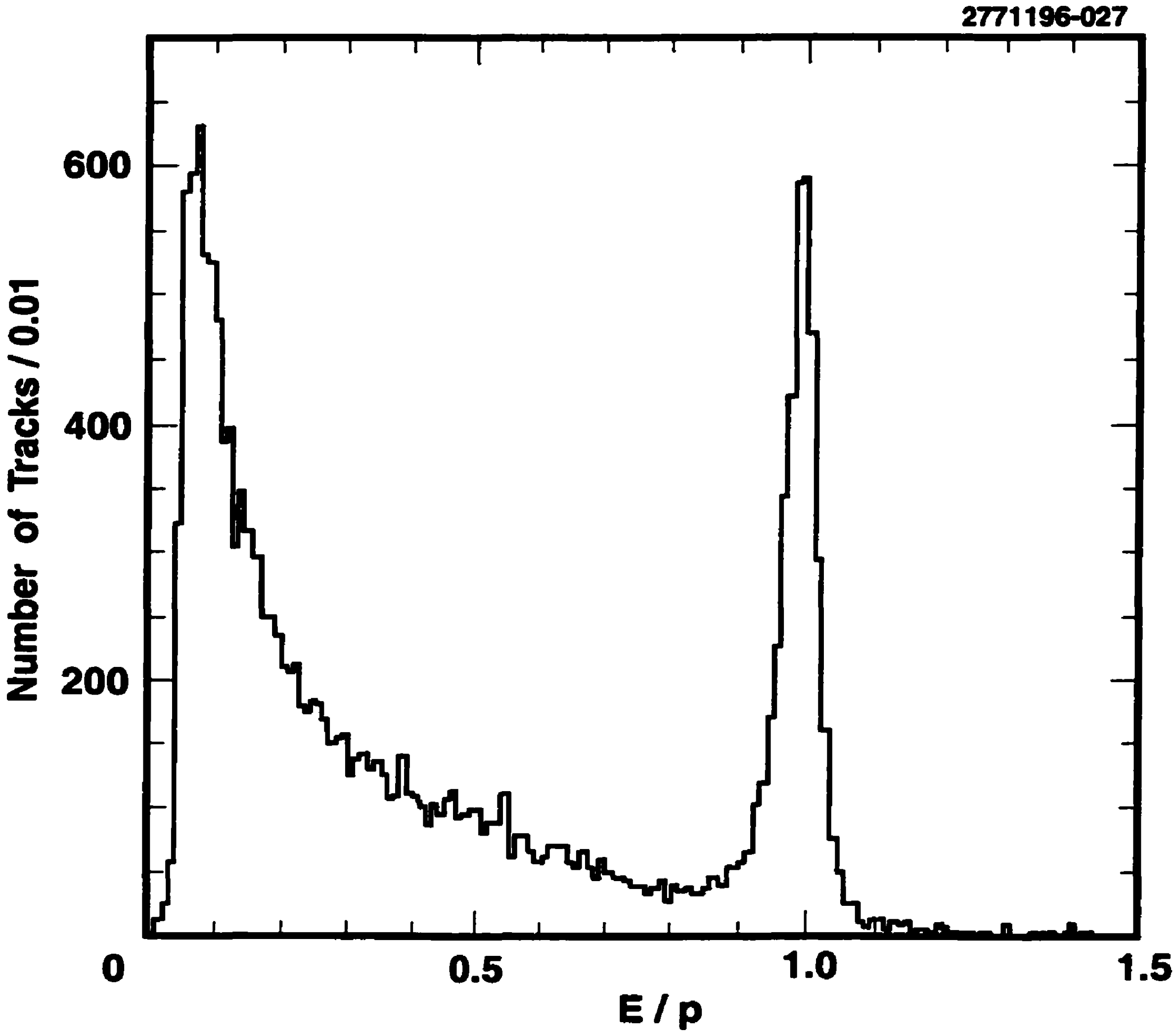

Figure 4.5: The ratio of the EM cluster energy to the momentum of the track pointing to the cluster. The peak at $E/p = 1$ is due to electron and the tail for $E/p < 1$ is due to hadrons and muons.

sample comes from $\Upsilon(1S)$ hadronic events which are known to have very few leptons in them.

For each charged track the probabilities of being an electron (P_e) and non-electron ($P_{\not e}$) are calculated for all variables. We then combine this information by computing a log-likelihood ratio defined as:

$$\mathcal{L}_e = \sum_{\text{variables}} \ln\left(\frac{P_e}{P_{\not e}}\right). \tag{4.4}$$

For a track to be identified as an electron we require $\mathcal{L}_e$ to be greater than 3.0 and $|\cos\theta| < 0.92$. We demand the electron momentum to be between 0.8 GeV/c and 2.0 GeV/c. The lower bound is set to minimize the contribution from secondary leptons from charm decays (*c.f.*, Figure 2.10). The upper bound is just below the kinematic limit for $B^- \to D^+\pi^-\ell^-\bar{\nu}_\ell$ (see Figure 4.4).

The electron detection efficiency is about 94% in the momentum range of 0.8 GeV/$c \leq |\mathbf{p}| < 2.0$ GeV/c [43]. Electron efficiencies are obtained from embedding Bhabha events in non-leptonic $\Upsilon(4S)$ events. The probabilities of misidentifying a hadron as an electron (called fake rates) are obtained from $\Upsilon(1S)$ hadronic events. The typical fake rate is found to be 0.1% to 0.2% per track [44].

4.6.2 Muon Identification

Muon identification relies upon the ability of muons to penetrate through the layers of iron absorber to the various levels of the muon chambers. Each super layer of the muon chambers is preceded by approximately two nuclear absorption lengths of iron. This arrangement leads to a muon-penetration threshold of 1.0 GeV/c to the first super layer, 1.5 GeV/c to the second super layer, and 2.0 GeV/c to the third super layer. We used the MUTR package for the basic muon identification. MUTR provides us with DPTHMU and MUQUAL. DPTHMU is the depth that the muon traveled, *i.e.*, the number of nuclear absorption lengths (λ) that the muon traveled. MUQUAL is a track quality flag which correlates hit patterns in the muon detector with the projected trajectories of the particles found in the central tracking detector. In the track matching algorithm, multiple scattering in the calorimeter and the iron, and the deflection caused by the magnetic field in the flux return are taken into account.

In this analysis, muons are required to have a good match (MUQUAL=0) between hits registered in the muon chambers and the extrapolated drift chamber track. Furthermore, muon candidates must satisfy the following acceptance cut:

- DPTHMU > 3
- $|\mathbf{p}| \geq 1.0$
- $|\cos\theta| < 0.92$

where θ is the angle of the muon candidate with respect to the beam axis. The angular and momentum coverage are constrained by the acceptance of the muon counters [45].

The muon detection efficiency for the different levels of the muon chambers, as a function of the muon momentum, is shown in Figure 4.6. The probabilities of misidentifying a hadron as a muon are much higher than the probabilities of misidentifying a hadron as an electron. The individual fake probabilities are determined by running the muon identification package on hadronic tracks. The hadron fake probabilities are found to be around $2-3\%$ for tracks with $3 \leq$ DPTHMU < 5, 1.0 GeV/$c \leq |\mathbf{p}| < 1.5$ GeV/c and below 1% for tracks with DPTHMU ≥ 5, $|\mathbf{p}| \geq 1.5$ GeV/c [46].

4.7 Charged Hadron Identification

As discussed in Chapter 3, two types of detectors are used for the identification of the charged tracks: the ToF counters and the drift chamber for the measurements of dE/dx. In this analysis we use both sources of information to get the best PID (particle identification) possible. First we describe how this information is extracted and next how these are combined into a qualitative measure that allows us to distinguish the various particles.

A relativistic particle passing through argon-ethane (50:50) at atmospheric pressure makes a collision about every 200 μm and transfers energy to the gas via ionization. In practice, we measure the amount of charge (converted to the pulse height in the data acquisition chain) collected on every wire and normalize it to the

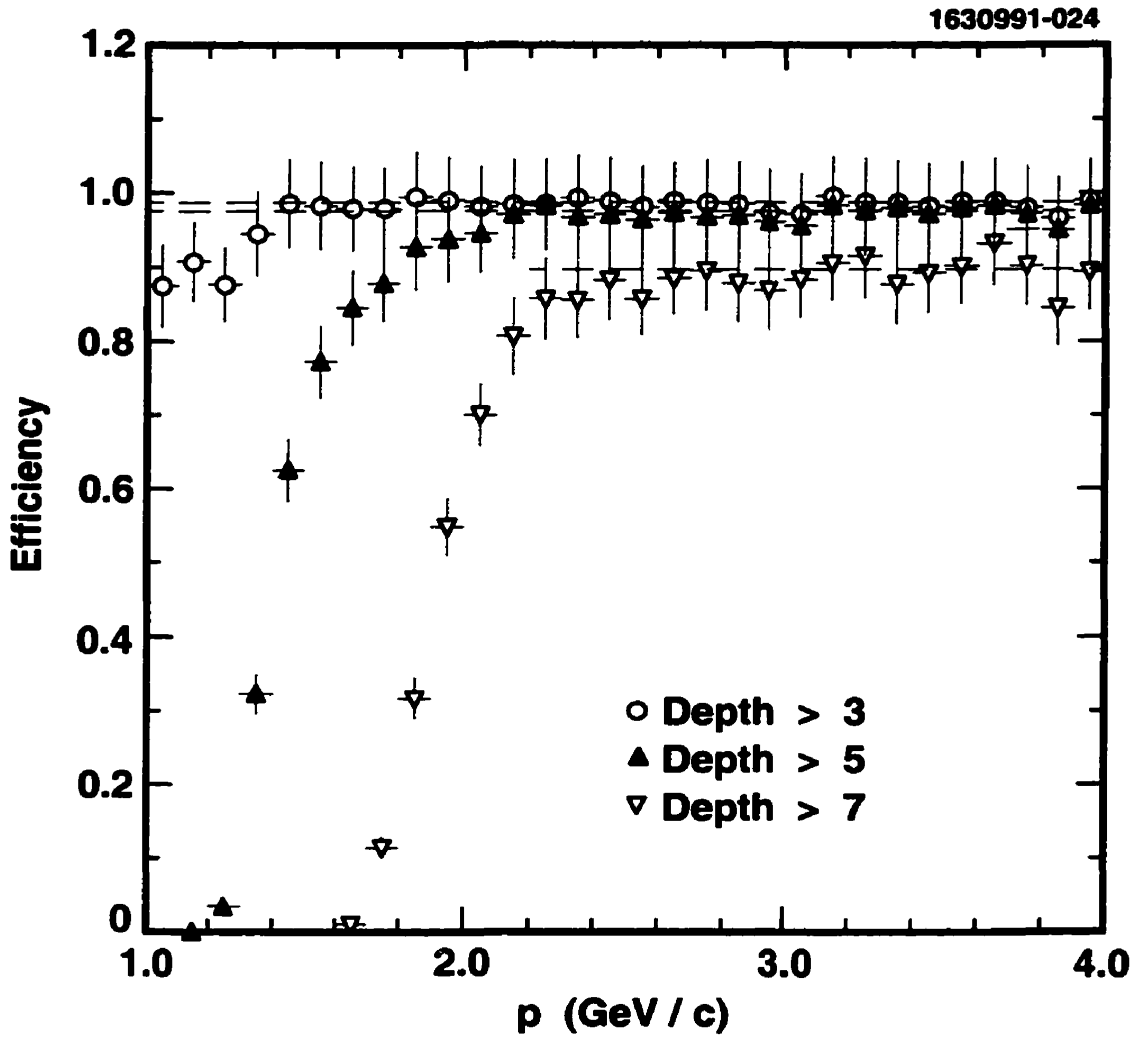

Figure 4.6: Muon identification efficiency versus momentum for three different depth requirements [30]: DPTHMU > 3, DPTHMU > 5, and DPTHMU > 7.

estimated track-length in the cell. Then, the specific ionization of a hadron candidate is determined by computing the truncated mean of the normalized pulse height over the ensemble of cells associated with the track. Using the truncated mean eliminates the long tail to high depositions created by the Landau distribution and leads to a more Gaussian behavior for the mean dE/dx result. For each measurement of the energy-loss, we require the hadron candidate to pass through at least four drift cells.

The specific ionization depends on the speed or $\beta\gamma$ of a relativistic particle [47]. Since the momentum of the particle is related to its mass by $|\mathbf{p}| = \beta\gamma m$, one can parameterize the energy-loss of the particle versus its momentum and then determine its mass. Figure 4.7 shows dE/dx as a function of momentum for different types of particles at CLEO II. As one can see, the dE/dx measurements yield good separation of kaons from pions up to momenta of roughly 700 MeV/c. These particle identification capabilities are useful for the reduction of the $\pi - K$ combinatoric backgrounds.

We obtain the timing information for a particular track by the time it traveled from the interaction region to the ToF detector. Since we can obtain the length from the known geometry of the detector, we can derive the velocity of the particle based on the time-of-flight of the particles. This information is then compared with the β from $p = M\beta\gamma$ to see which choice of M is best. Figure 4.8 shows a scatter plot of $1/\beta$ derived from the ToF versus momentum for various particles. The separation is good in the lower momentum region $p < 1.2$ GeV.

Whenever the information from each of these devices is available, it is quoted as the number of standard deviations from the measurement of the expected value for a given particle hypothesis. Both piece of information are combined into a single χ^2 for each charged track using:

$$\chi_i^2 = [\frac{(dE/dx)_{meas} - (dE/dx)_{exp}}{\sigma_{dE/dx}}]^2 + [\frac{(ToF)_{meas} - (ToF)_{exp}}{\sigma_{ToF}}]^2. \tag{4.5}$$

where i stands for the five different particle hypothesis.

For the particle ID, PID, we use the likelihood method based on these χ^2. First the probability distributions is obtained from:

$$P_{xx} = Prob(\chi^2_{Pid}, 2) \tag{4.6}$$

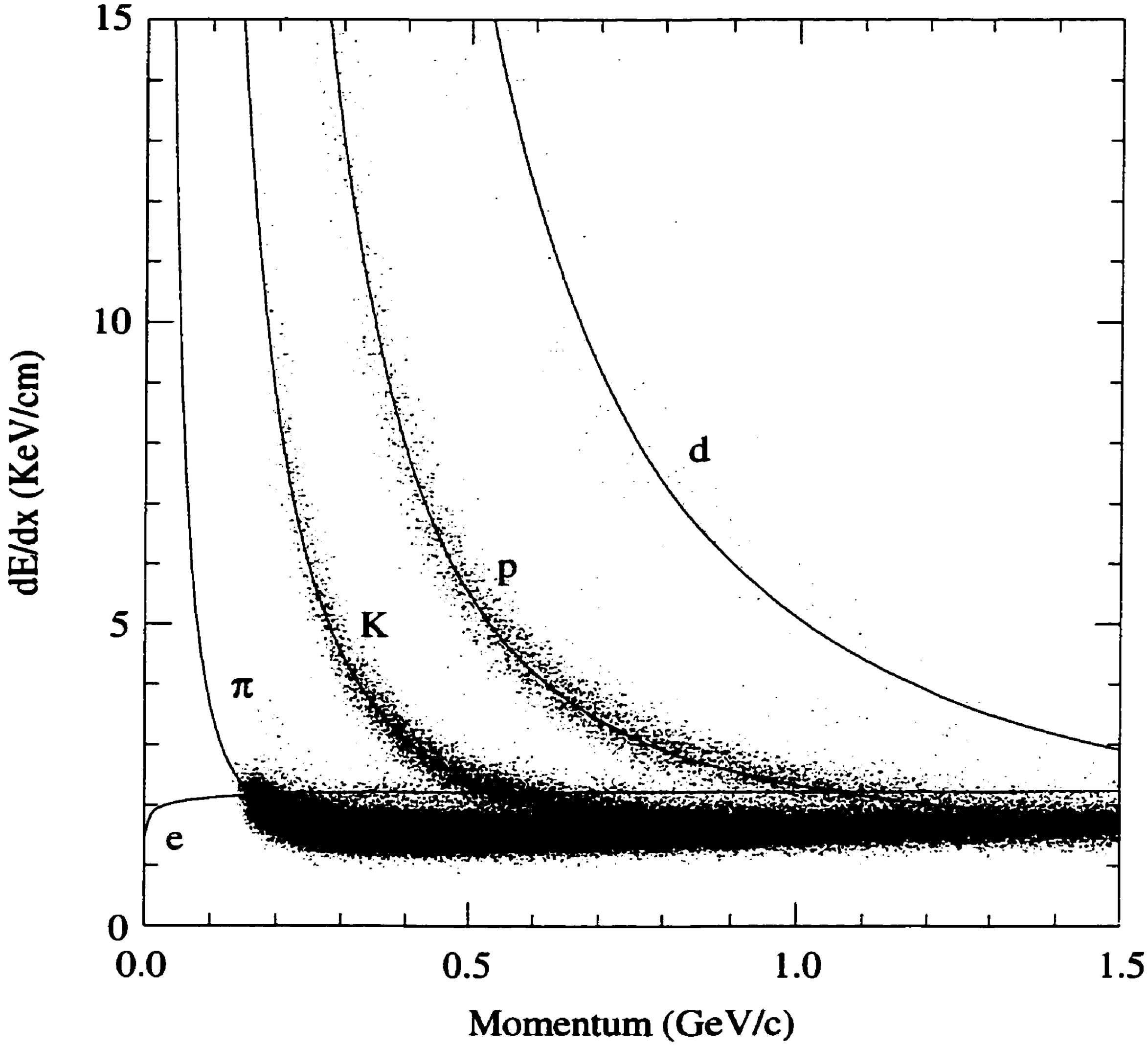

Figure 4.7: Specific ionization curves versus momentum for various species of hadron. One can identify bands corresponding to electrons, pions, kaons, protons and deuterons. The latter are produced predominantly through beam-wall interactions.

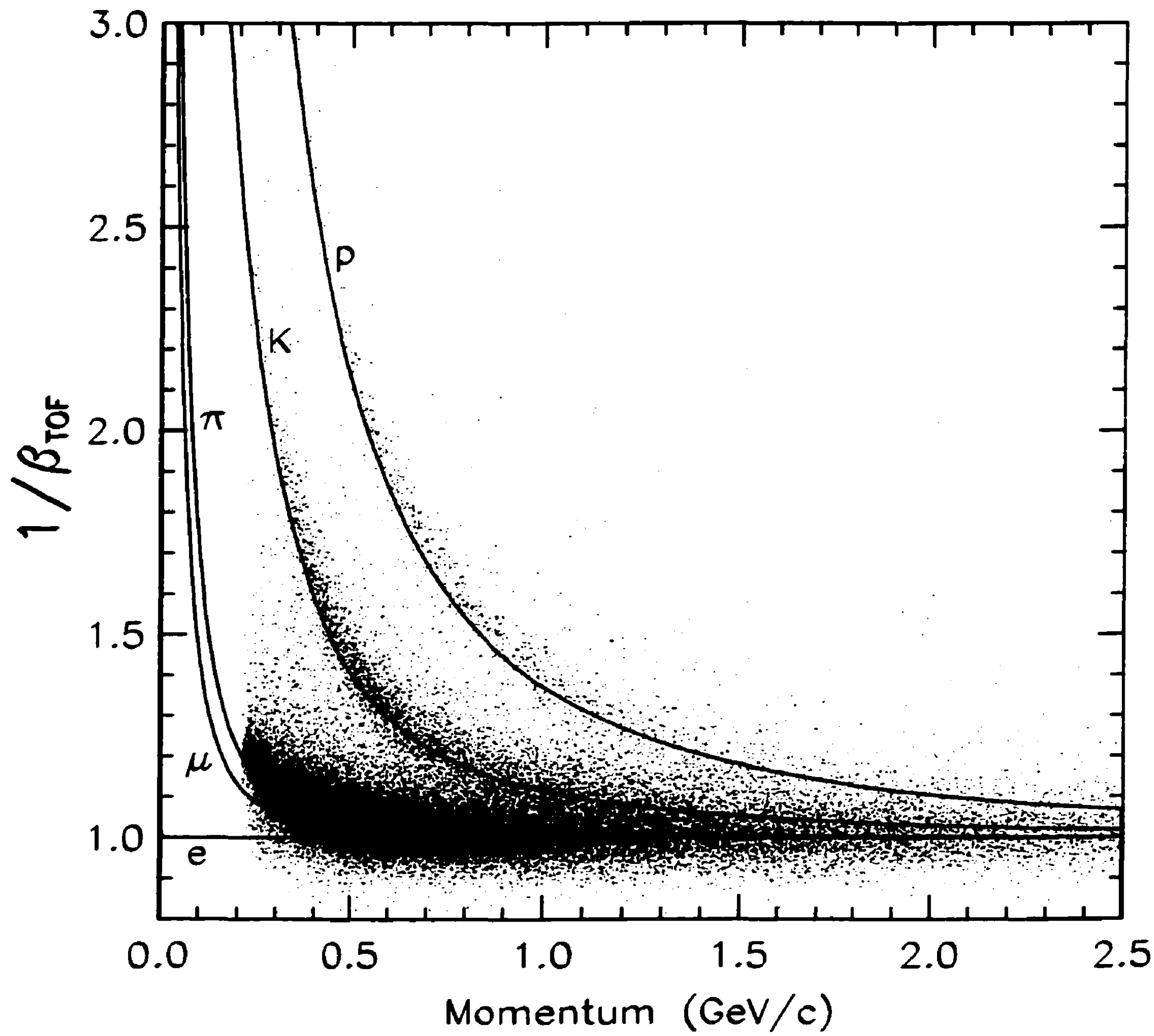

Figure 4.8: Time of Flight $1/\beta$ measurements versus momentum for various species of hadron. The mean of the different particle hypothesis, electrons, muons, pions, kaons and protons, are shown.

where $xx = e, \mu, \pi, K, p$. *Prob* is the probability function for the χ^2 with two degrees of freedom. In general:

$$Prob(\chi^2, n) = \int_0^{\chi^2} \frac{z^{n/2-1}e^{-z/2}}{2^{n/2}\Gamma(n/2)} dz \tag{4.7}$$

From the various probabilities we compute the likelihood for a track to be of a specific hypothesis using:

$$lh_{xx} = \frac{n_{xx}P_{xx}}{\sum_{j=1}^{5} n_j P_j}. \tag{4.8}$$

The different n_{xx} are defined as $n_p = n_K = n_e = n_\mu = 1, n_\pi = 5$. The justification for this is that there are 5 times as many pions per event as the other particles in a $B\bar{B}$ event. So we scale the probabilities accordingly.

Once each track has the likelihood computed we simply require the likelihoods $lh_\pi > 0.01$ and $lh_K > 0.01$ respectively for the PID of the pion and kaon.

4.8 D^+ Reconstruction

Once all the leptons and the hadrons have been reconstructed we are in a position where we can go ahead and reconstruct the D^+ meson. We consider the mode where $D^+ \to K^-\pi^+\pi^+$. During the selection of the tracks from the pion and kaon banks we explicitly require the correct charge to be selected. Thus in this case we select one track identified as a K^- and two tracks identified as π^+. The D^+ candidates are required to have a scaled momentum which is kinematically allowed for a D^+ meson from the signal:

$$x_D = \frac{|\vec{P_D}|}{\sqrt{E^2_{Beam} - M^2_D}} < 0.5 \tag{4.9}$$

This scaled momentum requirement is used to suppress fast D^+s from continuum events.

The invariant mass $M(K^-\pi^+\pi^+)$ for candidates which pass all the selection criteria described above is shown in Figure 4.9. The $K^-\pi^+\pi^+$ combinations are required to have an invariant mass within 15 MeV/c^2 (2.5σ) of the nominal D^+ mass

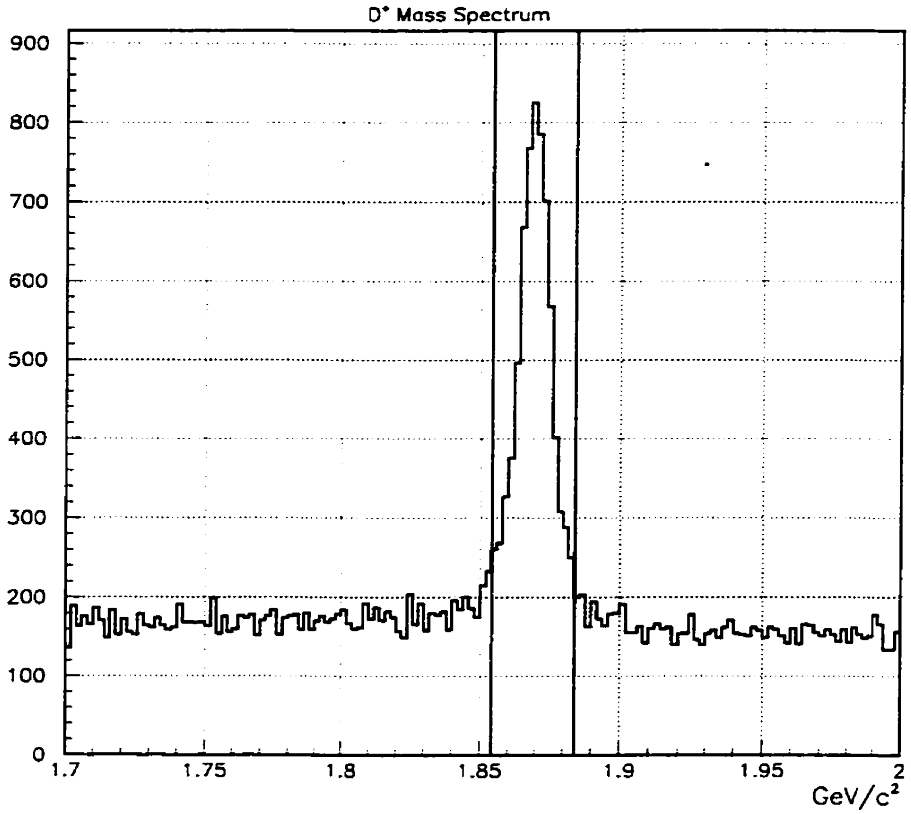

Figure 4.9: $K^-\pi^+\pi^+$ mass distribution. Events which are within ± 15 MeV/c^2 of the nominal D^+ mass are accepted as D^+ mesons candidates.

[1].

$$M(K^-\pi^+\pi^+) - M(D^+) < 15 \text{ MeV/c}^2 \tag{4.10}$$

We do not perform a kinematical fit to the D^+ meson candidate which usually improves the momentum measurement of the D^+ meson since the main degradation of the reconstructed B meson mass resolution arises later on during the process where we reconstruct the neutrino. None the less, we did study the effect of refitting the D^+ mesons to confirm this statement and effectively no improvement has been obtained from this extra procedure.

4.9 $D\pi e$ Candidates

The next step is to combine the electron candidate and any reconstructed D^+ meson in the event with an additional pion of the correct charge. Again we make use of implicit charge correlation while combining the different particles. We then further define a scaled momentum cut for the $D\pi$ combination as:

$$x_{D\pi} = |\vec{P}_{D\pi}|/\sqrt{E^2_{Beam} - M^2_{D\pi}} \tag{4.11}$$

and require $x_{D\pi} < 0.5$.

Due to the abundance of slow pions in our samples a great deal of background events can be rejected by selecting the pions above a certain momentum threshold. One has to be very careful though in cutting on the momentum since it is very model dependent. We do not want to optimize this cut in the usual way since this could bias us in the wrong direction. Our signal event pions are usually fast pions. Following this reasoning we decided to accept pions above 200 MeV since 99% of the signal sample events fall above this cut. This allows us to get rid of 30% of the background events.

One possible source of contamination for D^+ mesons in this decay channel would be from decays $D^{*+} \to D^+\pi^0$. In this case if we would drop the π^0 and pick up a π^+ from the rest of the event, we would have a hard time realizing this later on during the reconstruction process. We therefore define a D^* veto for each event where we attempt to reconstruct a D^{*+} using each D^+ in the event. To accomplish this we first need to find a π^0 in the event.

To reconstruct π^0's we combine two photons in the event with the following criteria:

- $E_\gamma > 50$ MeV
- $|\cos\theta_\gamma| \leq 0.95$
- The reconstructed π^0 must have $M_{\gamma\gamma}$ within 2σ of the π^0 mass.

Once we have all the possible π^0 candidates in an event predefined, we combine these with every D^+ candidate found previously. The final veto is based on the following expression:

$$[M(D^+\pi^0) - M(D^+)] - [M_{PDG}(D^{*0}) - M_{PDG}(D^+)] < 3 \text{ MeV/c}^2 \tag{4.12}$$

We simply calculate the mass difference of the D^* and the D. Similarly we evaluate this difference using PDG values. If the difference between the measured mass difference and the PDG mass difference is smaller than 3 MeV/c^2 we veto this event. In the signal region 2% of the events are rejected after all the analysis cuts have been applied while 13% of the events are rejected from the background.

4.10 Full Reconstruction

In this section we will give the outline of the formalism of full reconstruction. It is based on taking into account all the daughter particles of the B meson. Each individual track is reconstructed separately and then combined with all the others in a particular decay chain. This allows us then to completely reconstruct the B meson.

As we found out in Chapter 3, CESR has symmetric beam energies. This has the consequence that the energy of each B meson is the energy of the beams $E_B = E_{\text{beam}}$. Since the beam energy is well known we can deduce the momentum of the B. We can measure the magnitude of $\vec{P_B}$ but not its direction. From the beam energy measurements we know that $|\vec{P_B}| \simeq 325$ MeV.

The key variables for the full reconstruction are ΔE and M_B:

$$\Delta E \equiv E_{\text{beam}} - \sum E_i \tag{4.13}$$

$$M_B \equiv \sqrt{E^2_{\text{beam}} - |\sum \vec{P_i}|^2} \tag{4.14}$$

where the sums are over all the daughter particles of the B meson.

The variable ΔE expresses energy conservation while the variable M_B expresses momentum conservation. A feature of the variable ΔE is that it peaks at zero for real events. It is sensitive to missing particles and to misidentified pions and kaons.

This method is used extensively for hadronic decays. It can also be applied to semileptonic decay modes where the neutrino is inferred from global 4-momentum balance. This method will be discussed in the following section.

4.11 Neutrino Reconstruction

We assume initially that CLEO is an almost perfect hermetic detector that can correctly measure the momentum and energy of all particles except neutrinos and a few other types like antineutrons and K_L^0. We can then reconstruct the neutrino 4-vector from all the particles in the event. The total energy and momentum that can be measured are just the sums of the energies and momenta of all tracks and showers in the tracking chamber and calorimeter. The momentum of charged particles is measured by fitting their tracks. To determine the energy of charged particles, we must assign a mass to each particle track. Every track in the detector is attributed its best PID hypothesis and then assigned the mass of the associated particle. The energy of neutral particles is measured by the calorimeter. We assumed that all showers that are not matched to tracks and are not split off showers are due to photons. These could be primary photons, or secondary ones coming from the decay of other neutral particles, such as π^0 or η mesons.

If there are no neutrinos in an event in the almost perfect detector, the observed energy and momentum would equal the total energy and momentum of the event. If there are neutrinos, there would be a mismatch. Since we already have the tracks associated with the D, π and e tagged we can use this information with the remaining tracks in the event and sum the energy and momentum associated with each track and each unassociated neutral cluster. The missing energy and missing momentum are then defined as:

$$E_{miss} = 2E_{beam} - E_{D\pi e} - E_{rest} \tag{4.15}$$

$$\vec{P}_{miss} = -\vec{P}_{D\pi e} - \vec{P}_{rest} \tag{4.16}$$

where $E_{rest} \equiv \sum_{track\ cluster} E_i$ and $\vec{P}_{rest} \equiv \sum_{track\ drift\ chamber} \vec{P}_i$. If a single neutrino is the only unobserved particle in the event, we must have $E_\nu = E_{miss}$ and $\vec{P}_\nu = \vec{P}_{miss}$.

Unfortunately, CLEO is not a perfect detector. Some particles are lost while nonexistent particles are found. This causes a distortion of the E_{miss} and $\vec{P}_{miss}$. To get the best measurement of the neutrino momentum, and therefore the best information about the B meson decay, we need to eliminate these fake particles from the events and eliminate events with missing particles. Section 4.5 already described the process of rejecting extra tracks and showers using the requirements set by `TMNG` and `SPLITF` packages respectively.

If a particle in addition to the neutrino is lost, we will overestimate the missing energy and momentum, so such events should be discarded from our sample. Eliminating events with lost particles is more difficult, since there is no easy way of finding out that something was supposed to be there in the first place. However, circumstantial evidence can be used to make some rules about which events should be rejected. One instance is that leptons in hadronic events are almost always produced through charged current weak decays in association with neutrinos. An exception to this statement is the decay of a $\psi \rightarrow \ell^+\ell^-$, but since $(\mathcal{B}(B \rightarrow \psi X))(\mathcal{B}(\psi \rightarrow \ell^+\ell^-)) = 0.137\%$ [1], it is rare enough to be ignored. Hence an event with multiple leptons has multiple neutrinos, and therefore more than one missing particle. As described in Sections 4.6, 4.6.1 and 4.6.2 we make sure that only one lepton per event is selected. This requirement of rejecting events with more than one lepton removes 42% of the events. This rejection process cannot be perfect since we are unable to identify leptons with low momenta. There are also inefficiencies in the lepton identification for higher momenta.

Conservation of charge gives us another method of finding events with lost particles. Figure 4.10 shows the measured total charge (ΔQ) of signal Monte-Carlo sample events. Since our events are produced in e^+e^- collisions, the total charge of the event should be zero. If a charged particle is lost, or an extra particle is found, the total charge will be different from zero. In this analysis, we require $|\Delta Q| \leq 1$. A lost charged particle is most likely to have had low momentum, because of the turn-on of track finding efficiency with momentum. Losing a low momentum particle will not cause a bad overestimate of the missing momentum. The gain in efficiency from relaxing the total charge requirement from $|\Delta Q| = 0$ increases $S^2/(S+B)$. This requirement is 79% efficient for signal Monte Carlo events.

In Figure 4.11 we have the resolution on the missing momentum and energy where we plot $E_{\text{miss}} - (E_\nu)_{MC}$ and $P_{\text{miss}} - (P_\nu)_{MC}$. In general we tend to overestimate the missing momentum and energy, because the split off rejection algorithm is not perfectly efficient. The resolution on the missing momentum is better than the resolution on the missing energy, because the missing momentum is a vector sum, and mistakes tend to cancel. We measure $\sigma_{\vec{p}_{miss}} = 110$ MeV/c and $\sigma_{E_{miss}} = 260$MeV. We want to note that $\sigma_{\vec{p}_{miss}} < |\vec{p}_B| \simeq 320$MeV/c. This improvement on the resolution of the neutrino can be used to better separate signal $B^- \to D^+\pi^-e^-\bar{\nu}_e$ from more common background events.

Since the missing momentum measurement is better than our missing energy measurement, we define our neutrino energy using the magnitude of the missing momentum vector:

$$E_\nu \equiv |\vec{P}_{miss}| \text{ and } \vec{\mathrm{P}}_\nu \equiv \vec{\mathrm{P}}_{\text{miss}}. \tag{4.17}$$

In case some particles travel in the direction of the beam pipe and are misinterpreted as a neutrino, we require that the reconstructed neutrino points away from the beam pipe. This is accomplished by requiring that $|\cos\theta_\nu| < 0.95$, where θ is the polar angle.

Previous analyses [40, 41, 48] made use of the angle between the B momentum vector and $D\ell$, $D^*\ell$ or $D^{**}\ell$ (also known as the cosBY or cosBW cuts). In our case, this cut unfortunately sculpts the background into a peak at the B mass. We therefore decided not to use this cut in the present analysis.

4.11.1 Neutrino Quality

We do not have a similar conservation law to eliminate events with missing neutral particles. These remaining missing particle events are events containing K_L and extra neutrinos [40]. The K_L do interact in the calorimeter, and deposit some of their energy, but not all of it. The resulting showers are assumed to be photon showers, and the net measured energy in the calorimeter will then be underestimated. This in turn underestimates the missing energy. An attempt at eliminating events with

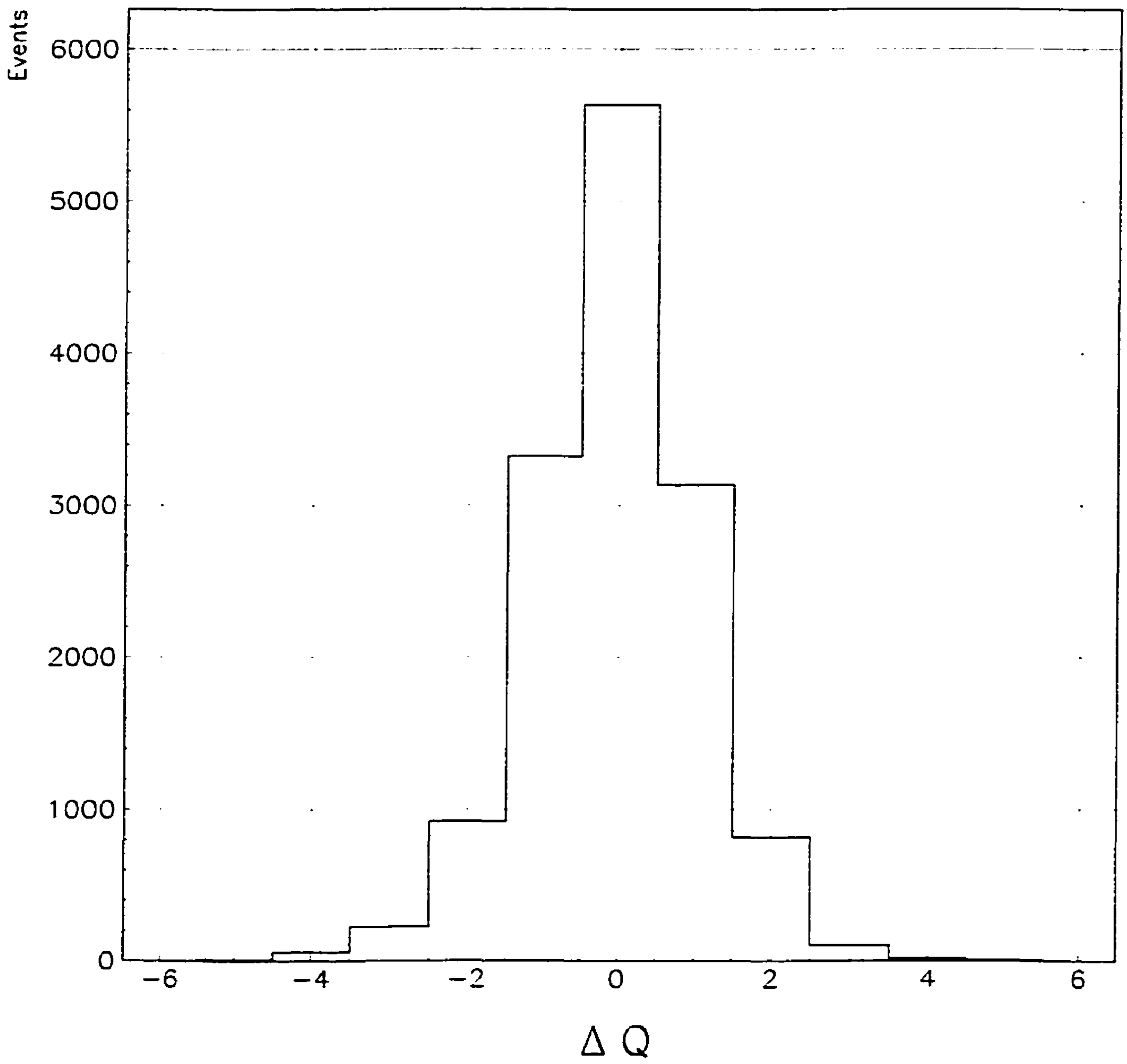

Figure 4.10: Net charge distribution for $B^- \longrightarrow D^+\pi^-e^-\bar{\nu}_e$ events.

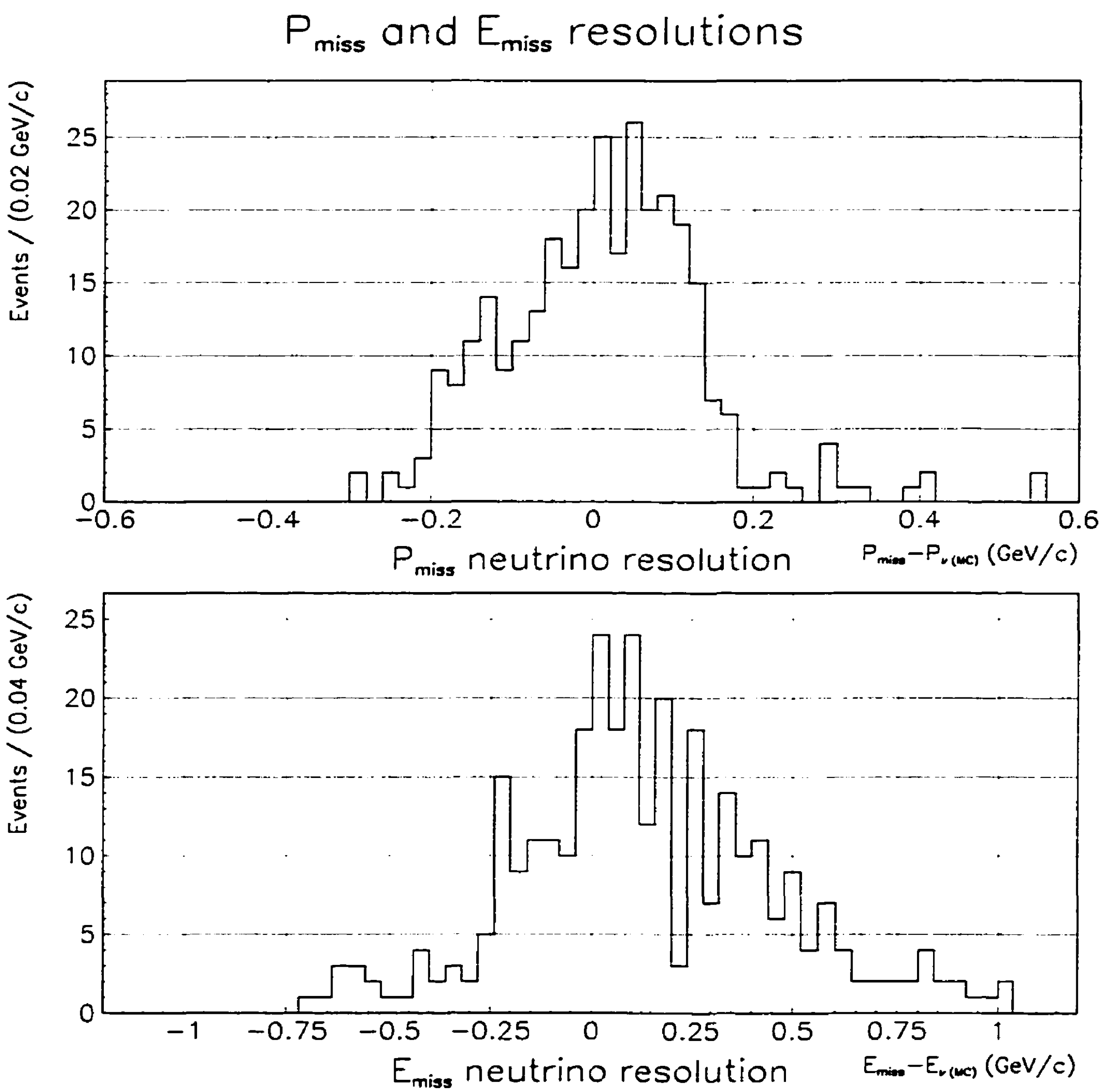

Figure 4.11: Resolution on $P_{\text{miss}} - (P_\nu)_{MC}$ and $E_{\text{miss}} - (E_\nu)_{MC}$ for the neutrino reconstruction technique.

additional missing particles, and to improve the missing momentum resolution, we use the fact that neutrinos are, within the resolution of our measurement, massless. The missing mass squared can be defined as:

$$M^2_{Miss} = E^2_{miss} - |\vec{P}^2_{miss}|. \tag{4.18}$$

which in the case of a single missing neutrino will be consistent with zero.

In previous B semileptonic analyses, this neutrino quality rule used to be called the V-cut and was defined as $M^2_{Miss}/2E_{miss}$. It had originally been designed for the $B \to \pi\ell\bar{\nu}_\ell$ analysis [40] where the neutrino is more energetic. We had lots of problems trying to prove that this V-cut could optimize the statistical significance of the signal over background. Hence a new cut was designed by studying the E^2_{miss} vs M^2_{miss} distribution. In this plot a linear relationship results and we require a cut on

$$X = E^2_{miss} + M^2_{miss} \tag{4.19}$$

The optimization of this cut is done using the $S^2/(S + B)$ method. Signal events are tagged and the background sample consists of the generic Monte Carlo sample. Since we have some combinatoric background present in our signal Monte Carlo events we add the antitagged signal to the background samples. By antitag we mean that the signal MC events are tagged for Monte Carlo true particle identity in the correct decay channel and then removed from the sample. Whatever is left is considered as background.

We then optimize:

$$\mathcal{F} = S^2_{tag}/(S_{tag} + (B_{generic} + S_{antitag})). \tag{4.20}$$

The cut has been optimized to : $X < 5$ GeV^2 using this method.

Figure 4.12 shows the distribution E^2_{miss} vs M^2_{Miss} for signal and background events. We can see that most of the signal events are found within the cut defined by the line $E^2_{miss} + M^2_{Miss} \geq 5$ GeV^2 while background events tend to populate the region outside the cut defined by the line. Figure 4.13 shows more detailed distributions of Figure 4.12. Figure 4.13a and 4.13b are for signal Monte Carlo events and 4.13c and 4.13d for background Monte Carlo events. Plots 4.13a and 4.13c have only events with one ν_e. Plots 4.13b and 4.13d have events with more than one neutrino, one K_L or one neutrino and one K_L. From 4.13a we can see that most signal events with only one neutrino fall in the optimized region. From 4.13d we can see that most background events with extra missing particles tend to be rejected by this cut.

Figure 4.14 shows the plot that illustrates the optimization process. The Y axis of the plot represents the value of F from equation 4.20 while the X-axis represents the value of the X cut. F is maximum for $X = 5$ GeV^2. All events falling below this cut are accepted, all the ones falling above are rejected. Figure 4.15 shows the effect of this cut on the B mass distributions of signal and background Monte Carlo. This cut is very effective. The Monte Carlo signal sample is reduced by 24% while the background Monte Carlo sample within the signal region is reduced by 58%.

4.11.2 ΔE of the Event

Finally we define the two key variables for the full reconstruction technique as described in Section 4.10. We will first look at the ΔE variable that defines the conservation of energy which provides some useful information about the decay. The ΔE cut is defined for the particle combination as follows :

$$\Delta E = E_{beam} - (E_{D\pi e} + E_{\nu}) = E_{beam} - (E_{D\pi e} + |\vec{P}_{miss}|) \tag{4.21}$$

ΔE should be close to zero for signal events. For hadronic decays, the resolution varies from 10 to 50 MeV, depending on the decay mode [49]. In the case with a neutrino present in the decay chain this resolution will be much larger, of the order of 200 MeV. Nevertheless it is a very good indicator for missing particles. If a pion is missing from a group of candidate particles, ΔE will be too large by at least 130 MeV which is large enough to show a significant shift in the ΔE distribution. Similarly if we gain an extra pion that should not have been in the decay in the first place as in the channel $B^- \longrightarrow D^0 e^- \bar{\nu}_e$ we will underestimate ΔE by at least 130 MeV.

As in the case of the $(E^2_{miss} + M^2_{Miss})$ cut, we optimize the ΔE cut using the $S^2/(S+B)$ method. In this case we set two floating boundaries for the optimization. The upper and lower boundary are respectively positive and negative. A three dimensional representation of this optimization process can be seen in Figure 4.16

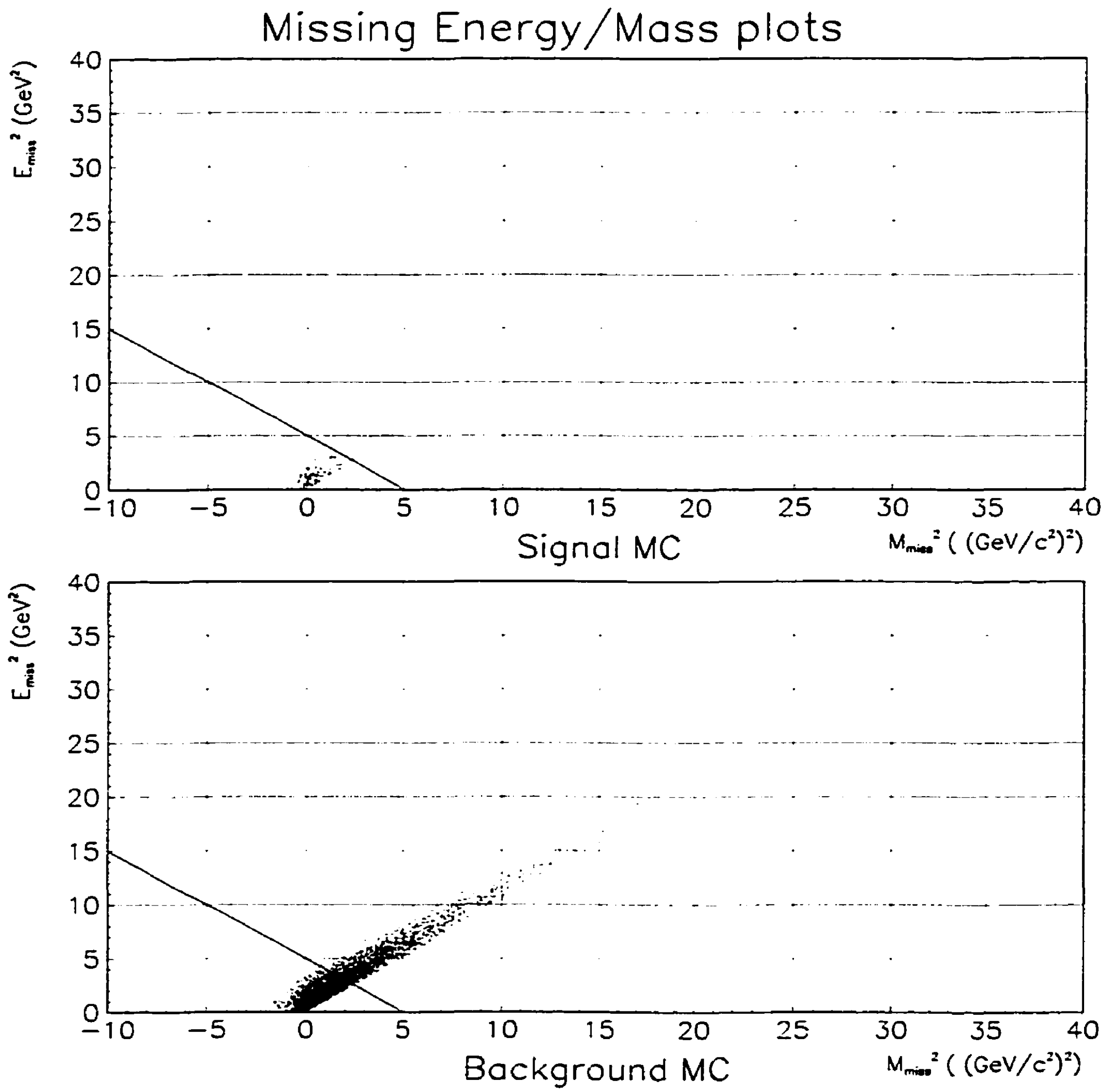

Figure 4.12: 2D plot of E_{miss}^2 vs M_{Miss}^2 for signal and background events. The line represents the rejection cut $E_{miss}^2 + M_{Miss}^2 \geq 5$ GeV^2.

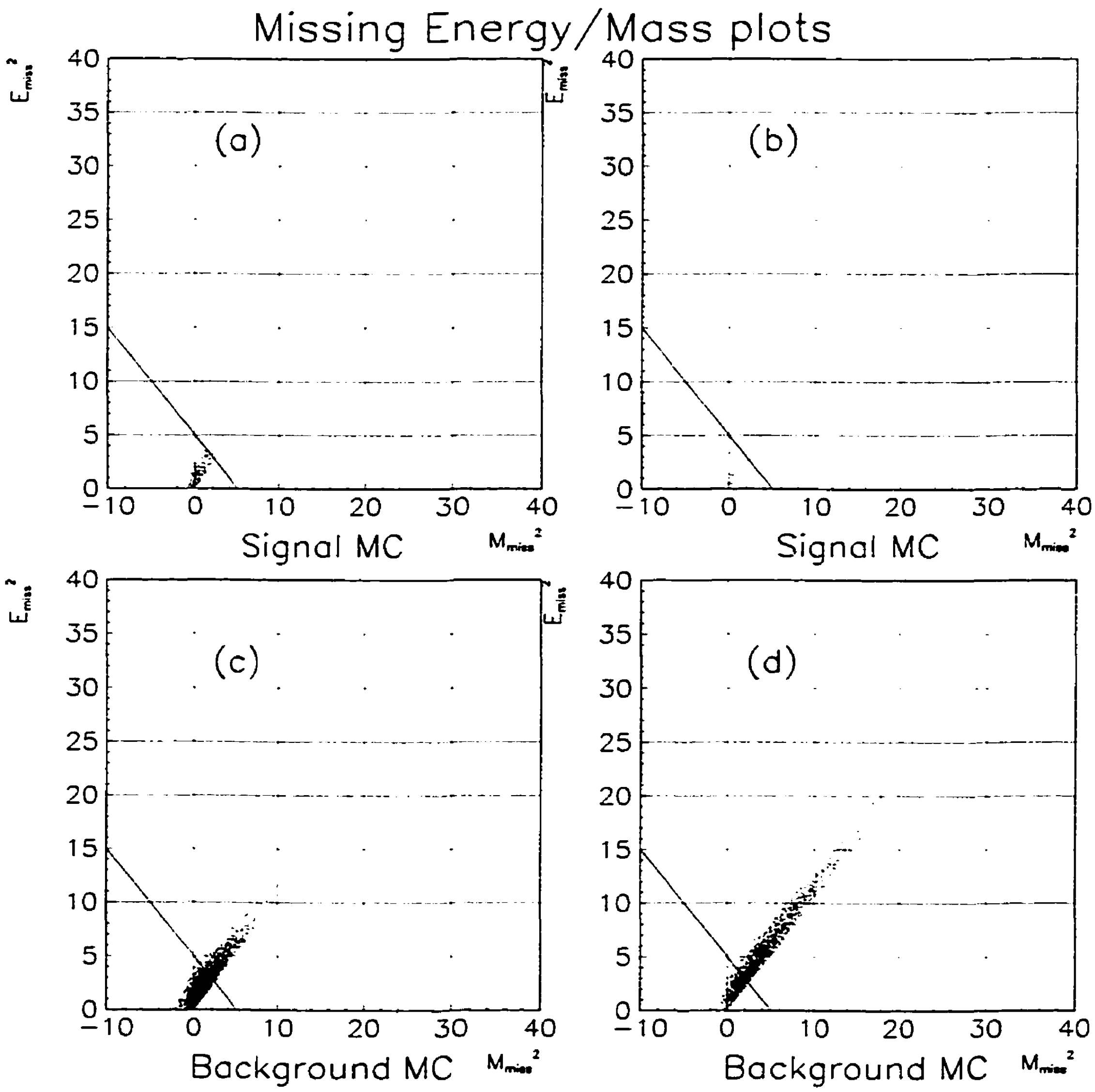

Figure 4.13: Detailed missing Energy/Mass plots. Plots (a) and (b) are for signal events, plots (c) and (d) for background events. Plots (a) and (c) have only events with one ν_e. Plots (b) and (d) have events with more than one neutrino, one K_L or one neutrino and one K_L.

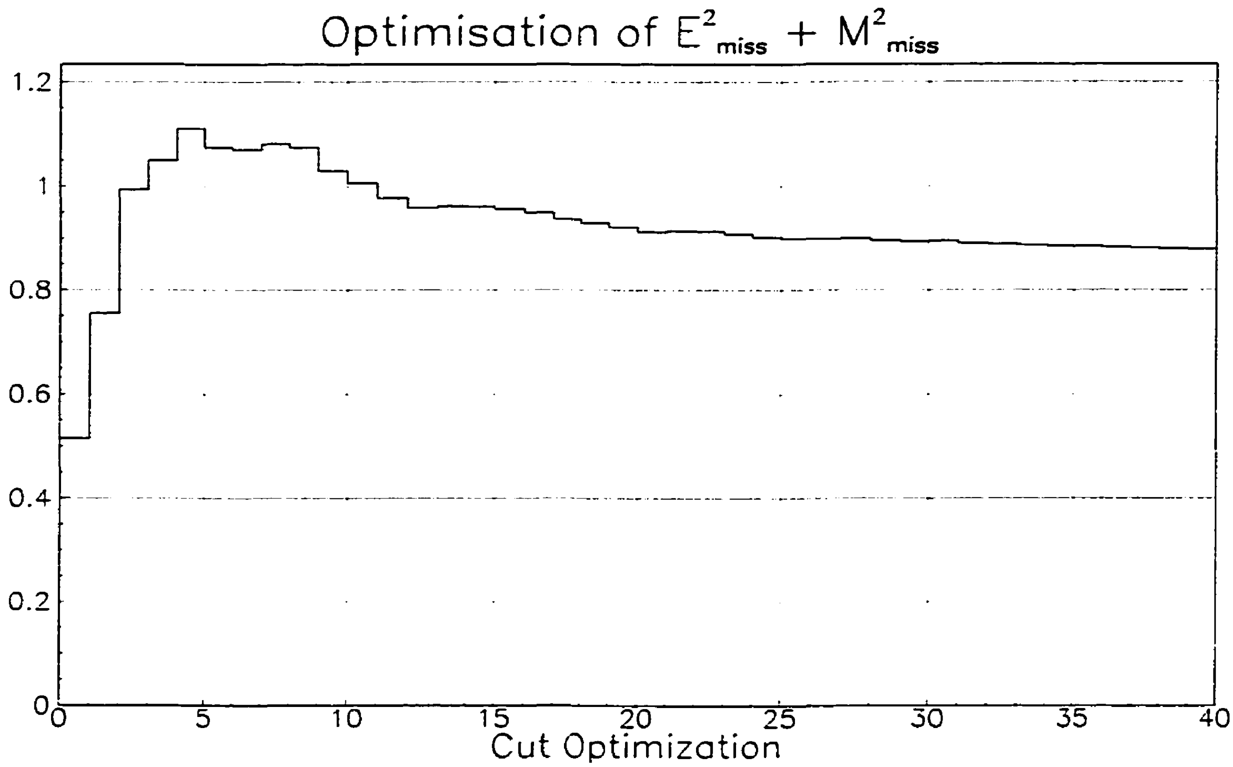

Figure 4.14: This plot shows the optimization process of the X cut where $X = E^2_{miss} + M^2_{Miss}$. The y axis represents the value of $\mathcal{F}$ (see text). The x axis represents the value of the X cut.

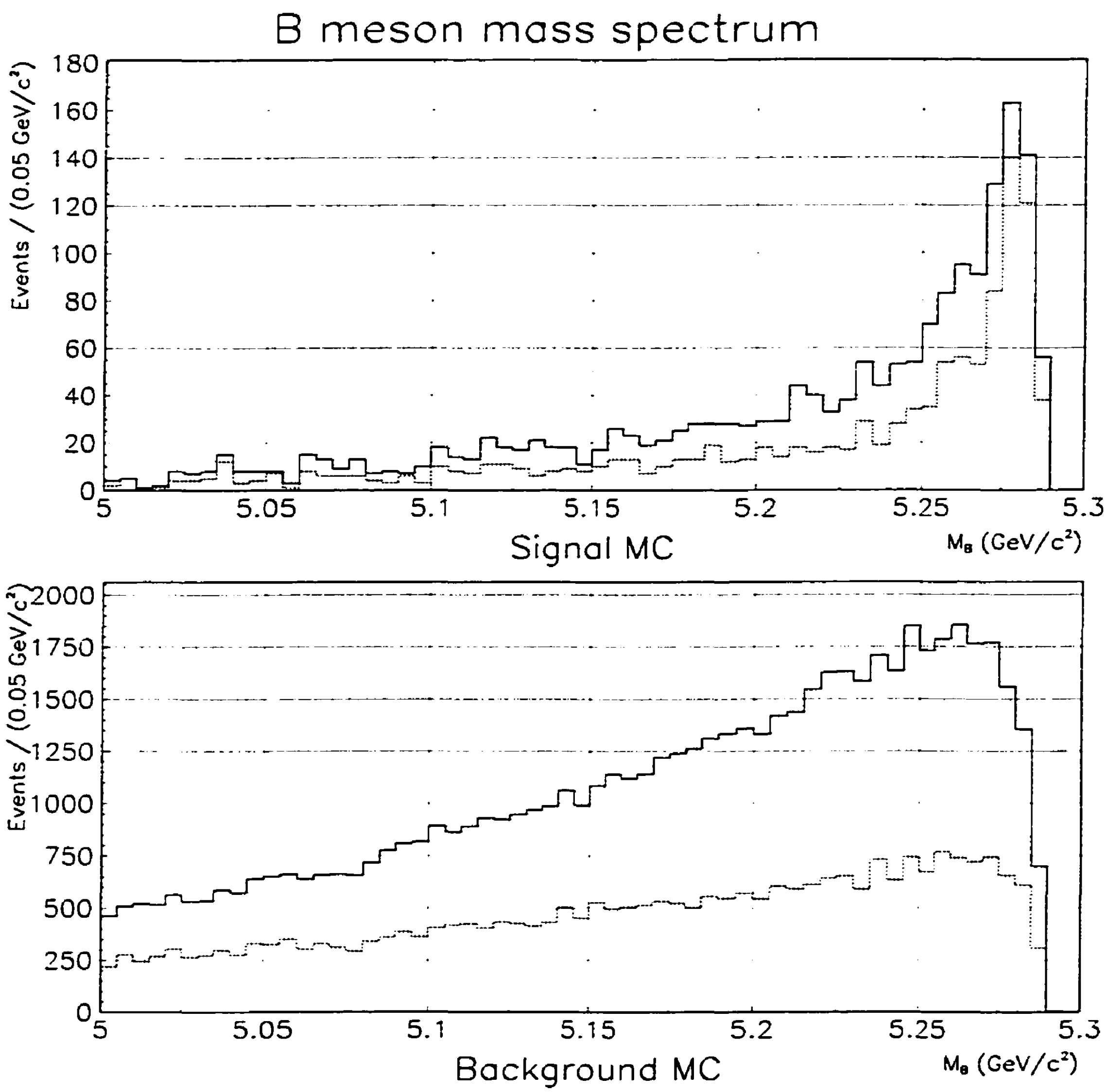

Figure 4.15: The effect of the X cut on the B mass distributions. The full line is before the cut, the dashed line is after the cut.

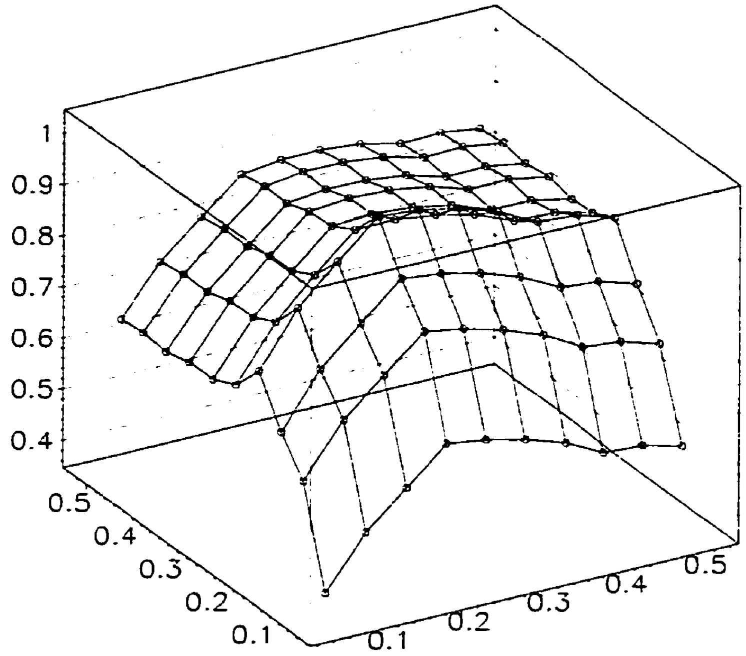

Figure 4.16: ΔE cut optimization. The x and y axis are the two extreme values of the ΔE cut, and the z-axis is the value of the optimization $\mathcal{F}$.

The optimal value for this variable is found to be where F is maximal and that is the case for -0.20 GeV $< \Delta E < 0.2$ GeV.

Figure 4.17 shows the ΔE distribution for signal and background events. As expected the signal events are nicely peaking around of $\Delta E = 0$ MeV while background events peak around $\Delta E = -400$ MeV, meaning that we tend to overestimate the energy in selecting the decay channel from background events. Figure 4.17 also outlines the values of the optimized cut on ΔE. This cut is 61% efficient for signal events and 27% efficient for background events.

4.12 B Mass Constraint

The last step in the reconstruction of the decay channel that we are investigating is to compute the B meson mass. We accomplish this using the beam constrained B mass calculation. This is based on the fact that the energy of the B meson has to be the energy of our beams. Instead of using the reconstructed energy of the B we replace it by E_{beam}, the beam energy which we are able to measure very accurately on a run by run basis. The precision is determined to be about 2 MeV by measuring the currents in the CESR electromagnets. The expression for the mass of the B is then:

$$M_B = \sqrt{E_{beam}^2 - \mid \vec{p}_{D^+} + \vec{p}_\pi + \vec{p}_e + \alpha\vec{p}_\nu \mid^2} \tag{4.22}$$

where $\alpha = 1 + \Delta E / |\vec{P}_{miss}|$. This re-scales the neutrino momentum such that $\Delta E = 0$ in the calculation of M_B, which is a first order correction to the neutrino momentum measurement. This re-scaling of the neutrino momentum improves the resolution on M_B.

Figure 4.18 shows the M_B distribution of our signal events. There is a clear peak near $M_B = 5.29$ GeV, which has a width of 8 MeV. The resolution in semileptonic decays on M_B is worse than in hadronic events (which have a resolution ≈ 3 MeV), because the resolution on the neutrino momentum is much worse than that for the momenta of any other particle. The bins that define our signal region are chosen

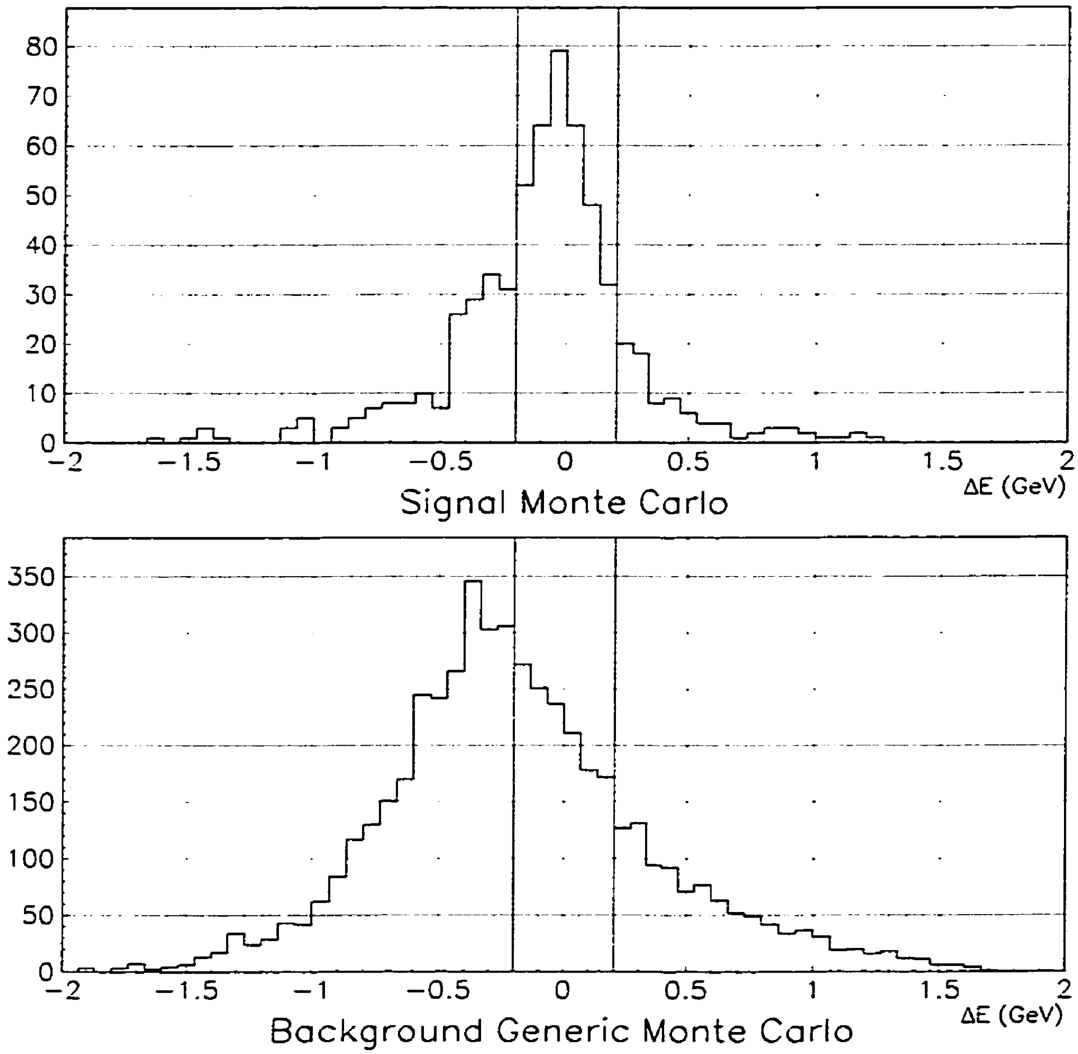

Figure 4.17: ΔE distribution for signal and background events. The lines represent the optimal values for the cut on ΔE.

to be:

$$5.2650 \leq M_B < 5.2875 \text{ GeV}. \qquad (4.23)$$

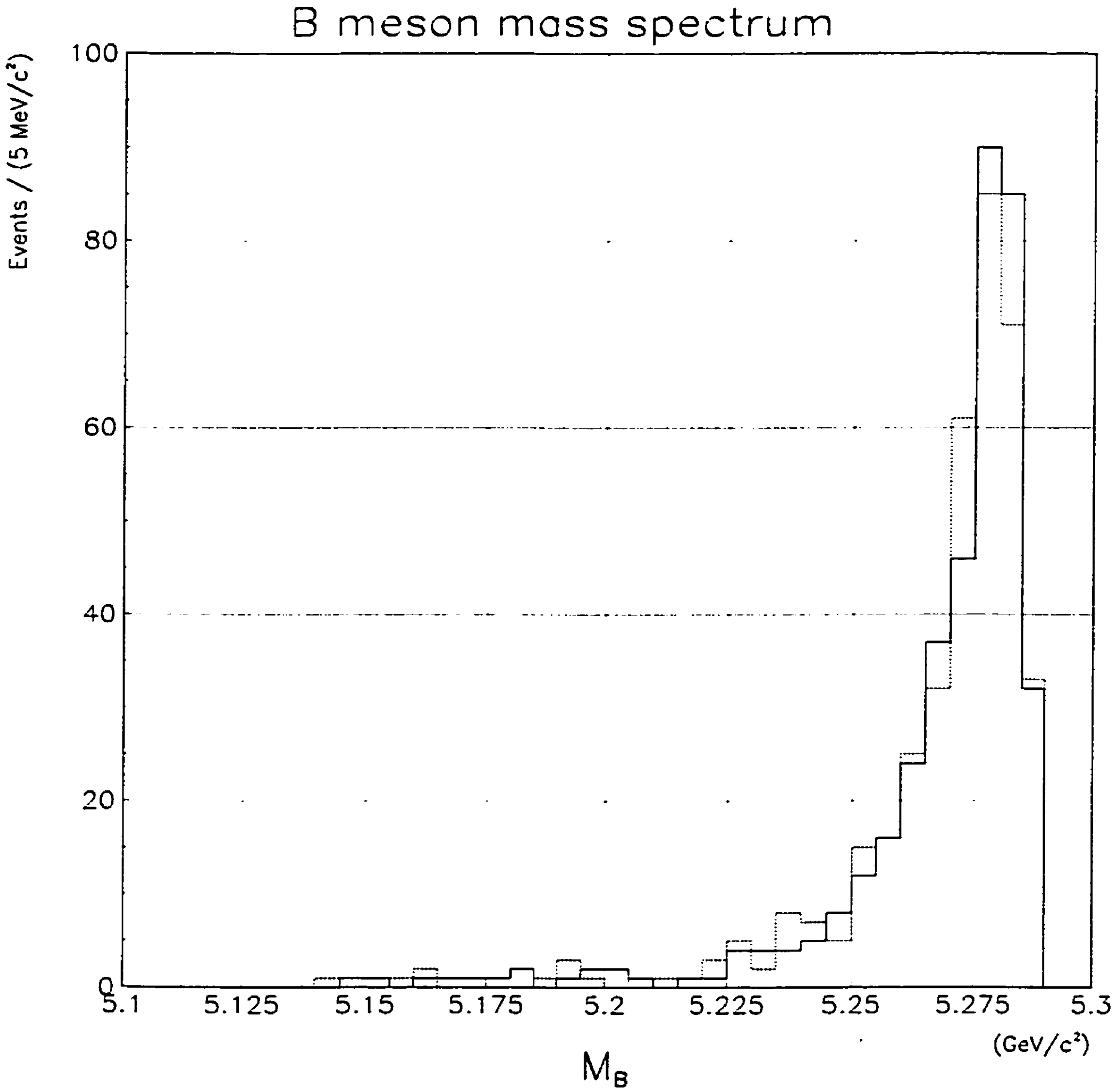

Figure 4.18: Mass spectrum for candidate particles reconstructed in the decay $B^- \rightarrow D^+\pi^-e^-\bar{\nu}_e$ for the signal Monte Carlo sample. The full line represents the rescaled M_B distribution and the dashed, broader curve, represents the unscaled M_B distribution.

Chapter 5

Experimental Results

The previous chapter concentrated on the detailed description of the different event selection criteria as well as the reconstruction of the various components of the B meson decay channel under study, the D^+, π^-, e^- and the $\bar{\nu}_e$. Of course, we used MC simulations extensively. In this section we look at the more quantitative aspect of extracting a measurement for the branching fraction $B^- \to D^+\pi^-e^-\bar{\nu}_e$ from the data sample. We also present the various tests we performed to assure us that the method we used is the correct one and that it provides us with a reliable result.

Once all the selection rules are applied, we calculate the beam-constrained B mass for each $D^+\pi^-e^-\bar{\nu}_e$ combination. From there we have two methods for extracting the signal which we will describe in detail. Both of these methods rely on how we parameterize our remaining backgrounds. A section will be dedicated to this part of the analysis.

5.1 Data Search For The B Mass Spectrum.

After applying all the selection requirements and calculating the mass of the B meson candidate the evidence for $B^- \to D^+\pi^-e^-\bar{\nu}_e$ would be seen as an enhancement in the signal region defined by Equation 4.23. We therefore process all the data events available and display this calculated B meson candidate mass. Figure 5.1 shows the resulting mass spectrum.

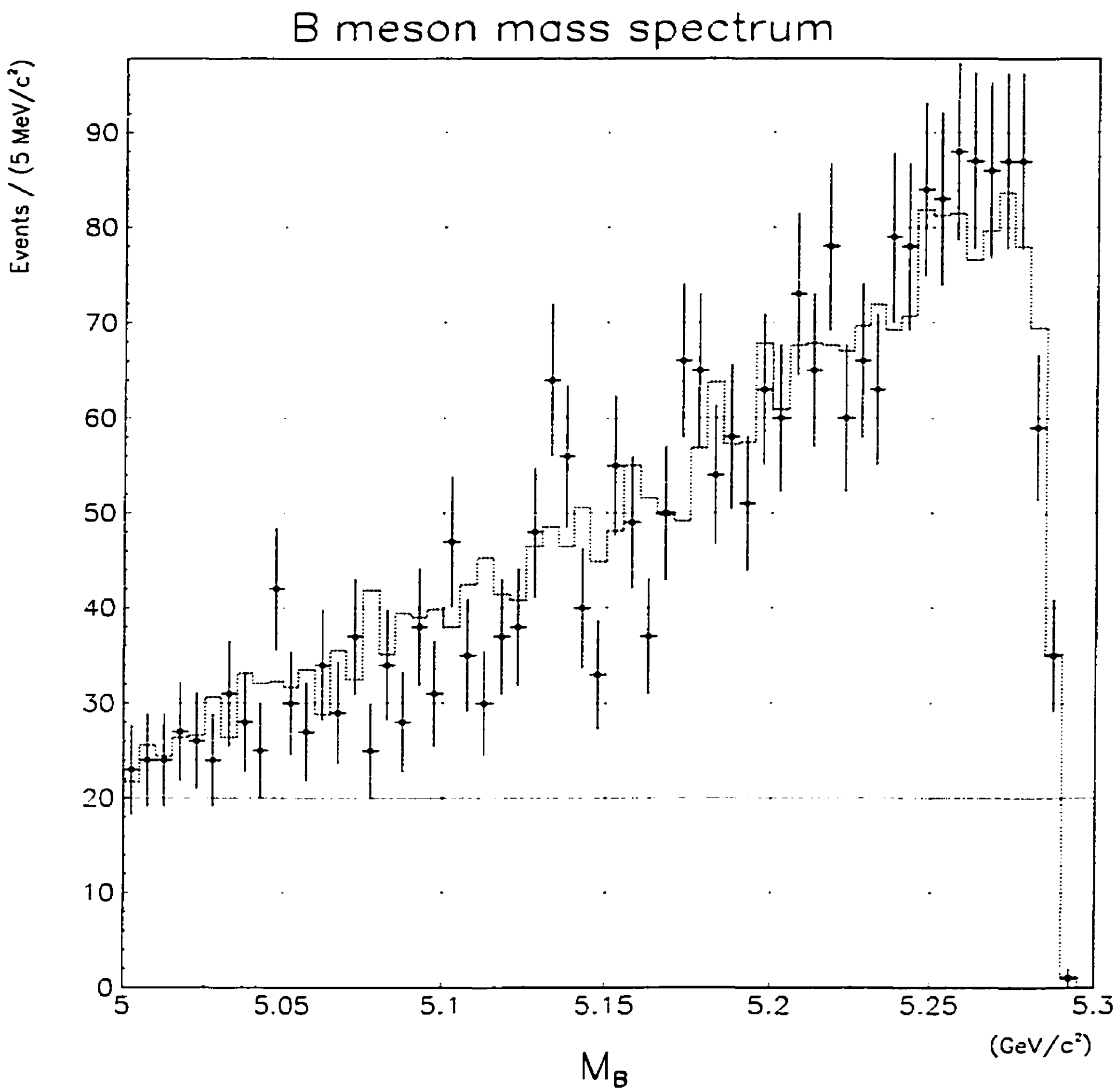

Figure 5.1: B meson mass spectrum. The data plot is continuum subtracted and the bars on the events represent the statistical error only. The dashed line is the scaled generic Monte Carlo background.

Overlayed on top of the data points is the expected background as estimated from our generic Monte Carlo background sample. A scaling of 0.2031 is applied to the Monte Carlo sample since this sample is generated approximately five times the luminosity of the data sample. This scaling is obtained from the ratio of the luminosities of the two samples.

5.2 Background Studies

Despite strenuous efforts, it is impossible to entirely remove background events from our sample through our event selection requirements. Instead, we find ways to estimate the rates for backgrounds that remain. Any remaining events not accounted for afterwards are presumably $B^- \to D^+\pi^-e^-\bar{\nu}_e$ decays.

We also look at what events are in our background sample. From the M_B bin we get the decay modes and fractional compositions of these as shown in Table 5.1 and Figure 5.2. These are after all the analysis cuts have been applied. The dominant contribution is from $D^*\ell\bar{\nu}_\ell$ events. The $B^- \to D_1^0e^-\bar{\nu}_e$ and $B^- \to D^0e^-\bar{\nu}_e$ are the next most important contributions. We also have the other $D\pi\ell\bar{\nu}_\ell$ $D^*\pi\ell\bar{\nu}_\ell$ non-resonant modes that contribute. These modes explicitly exclude the signal channel.

Table 5.1: Composition of the background events found in the M_B region.

Decay Mode	Fraction of total
$De\nu$	14.3%
$D^*e\nu$	44.4%
$D^{**}e\nu$	16.1%
$D\pi e\nu$	4.7%
$D^*\pi e\nu$	9.8%
secondary leptons	10.7%

These studies confirm that there is a significant amount of background events present in our data sample. As outlined in Section 4.3, we have subdivided our backgrounds into 4 different categories which we will now treat separately. First we will deal with the backgrounds from continuum and fake leptons. The next step

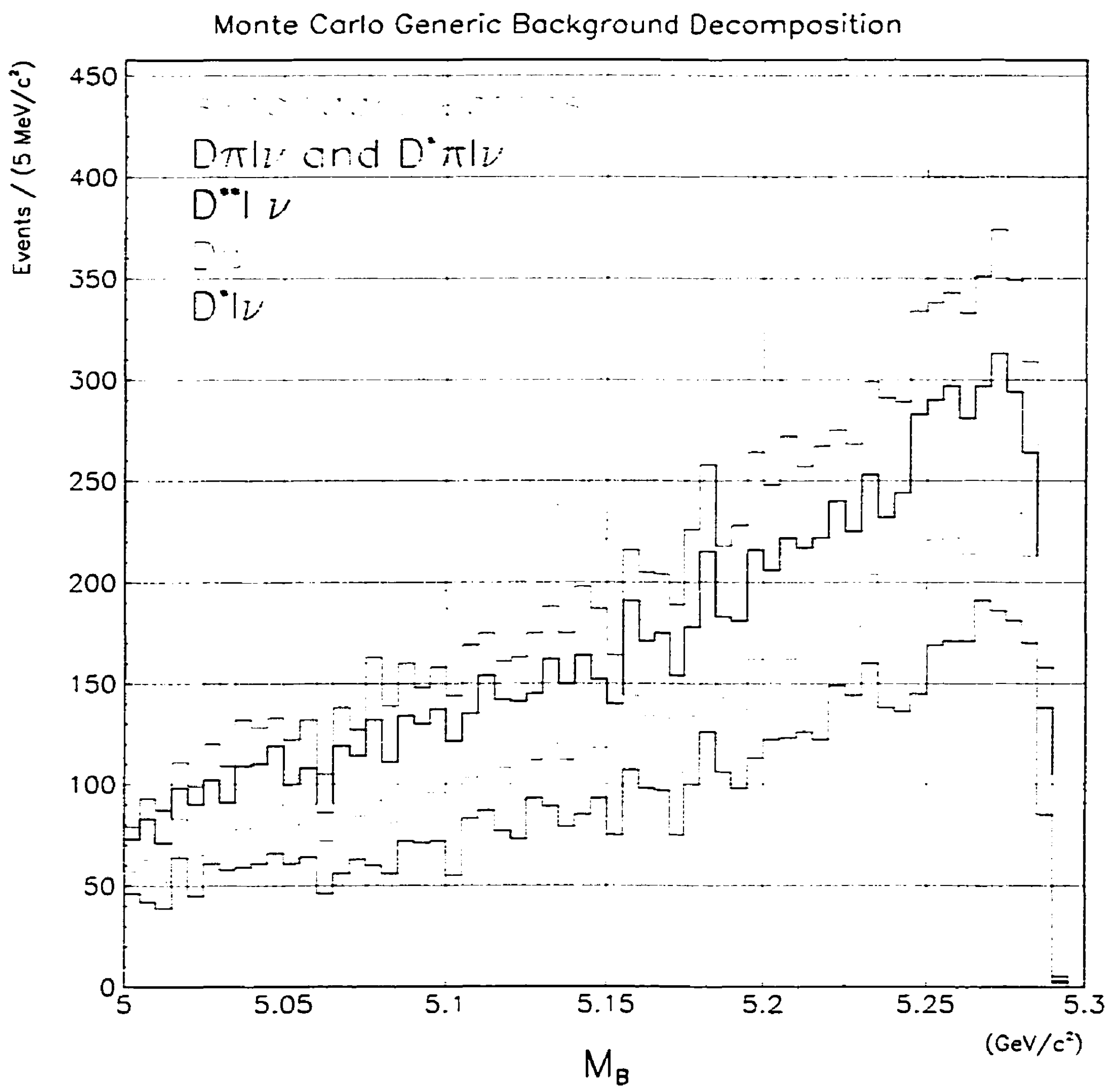

Figure 5.2: B meson mass spectrum for background Monte Carlo distributions. The various exclusive channels are displayed cumulatively. Each interval displays the corresponding contribution to the total background plot.

will be to remove the combinatoric backgrounds coming from misreconstructed D^+ mesons. This will be an important step, since the major portion of the remaining backgrounds can be accounted for using this subtraction process. The remaining events will have true De combinations. We have two methods to deal with these type of backgrounds and we will explain both of them even though only one will be used for this analysis for practical reasons.

5.2.1 Continuum Backgrounds

Our data are taken on the $\Upsilon(4S)$, but we have seen that there is a significant contribution to the total hadronic cross section at that energy from continuum $q\bar{q}$ production and some $\tau^+\tau^-$ production. Therefore not all of the events we select are necessarily $B\bar{B}$ decays. The presence of a high-momentum lepton (which indicates the change of flavour required in B decay, rather than hadronisation) and the requirement on R_2 enhance the $B\bar{B}$ content of our sample, but they do not ensure that the events are $B\bar{B}$ decays.

This fake B background, also called continuum background, is easily modeled using the OFF resonance CLEO data sample. Since events in this sample arise only from $q\bar{q}$ and $\tau^+\tau^-$ production, which is exactly the background we wish to study. We therefore use this sample for our fake B meson background.

We apply all the cuts as described in Chapter 4 on the data sample. We then subtract this continuum contamination. This is accomplished using off resonance events in the data that pass all our selection criteria except for the M_B cut and have $E_{beam} < 5.28$ GeV. The following transformation is applied to the events to map them into the right M_B range :

$$M'_B = M_B + (5.289 - E_{beam}). \tag{5.1}$$

This is to take into account the fact that our continuum sample is taken at ~ 55 MeV below the $\Upsilon(4S)$ resonance and that our calculated M_B depends on the measured E_{beam}. The final plot has to be scaled to take into account the ratio of luminosities of ON/OFF 4S data and the slight difference in the beam energies. This normalization of the continuum background is given by

$$s(4S) = \frac{L_{tot}(ON)E^2_{beam}(OFF)}{L_{tot}(OFF)E^2_{beam}(ON)} \tag{5.2}$$

where the meaning of ON and OFF is on and off resonance for each quantity, L is for the different luminosities. In our case we obtain a continuum scaling of 1.92.

5.2.2 Fake Lepton Backgrounds

Lepton identification is not perfect, as some hadrons can accidentally mimic the energy loss and E/p characteristics of electrons, and some have sufficient momentum to penetrate the muon chambers. To determine the average probabilities of misidentification for hadrons in B decays, we need to know the individual misidentification probabilities for pions, kaons, and protons, and their relative abundances. These studies have been done before and are summarized in References [19, 50] along with the corresponding lepton fake rates. These fake rates can be used in conjunction with the data to estimate the number of events passing our requirements that contain fake leptons.

The fake rates for electrons is around 0.1%. After all analysis cuts, the number of fake electrons from misidentified hadrons is in fact consistent with zero. Converted photons are also a source of fake electrons. We estimate the number of converted photons with Monte Carlo simulations and find no significant contribution to the yield for fast electrons with momenta between 0.8GeV/c and 2.0GeV/c. Thus, no contribution from fake electrons (misidentified hadrons and converted photons) is subtracted from the final results.

5.2.3 Combinatoric Backgrounds

After the continuum and fake leptons have been accounted for, all of our remaining candidate $B^- \longrightarrow D^+\pi^-e^-\bar{\nu}_e$ events contain a real B meson, a real lepton, and a real neutrino. However, these events can still contain fake D mesons. These arise from random combinations of tracks that just happen to have an invariant mass satisfying our requirements, and is therefore called combinatoric background. Figure 5.3 shows the $K^-\pi^+\pi^+$ invariant mass distribution for generic Monte Carlo events passing all requirements except for that on the invariant D^+ mass. If there were no combinatoric background, we would only see a peak centered at the D^+ mass value and no further entries in the histogram. (The peak has a finite width because the D has a finite lifetime, and because of detector resolution.) Instead, there are many additional events, both under the peak and on either side of it.

We assume that the combinatoric background events in our analysis sample can be modeled by events which fall just outside the requirements in $K^-\pi^+\pi^+$ invariant mass, because these events also contain random combinations of particles. This technique is known as a "sideband subtraction." The D lower sideband is defined as the region between $1.8243 < M_{K^-\pi^+\pi^+} < 1.8393$, and the upper sideband as the region between $1.8993 < M_{K^-\pi^+\pi^+} < 1.9143$. It is divided such that the interval of M_D candidate masses in the sidebands is equivalent to the interval of M_D masses in the central band signal region. This choice is quite arbitrary since one could decide to define sidebands as large one likes, except that farther away from the central band the physics processes contributing to the background may differ from those contributing near the D mass. So we restrict ourselves to these regions. This problem of deciding on how to define the sidebands is also true in the case of the other studies performed at CLEO on this technique. In summary, care is necessary in not picking sidebands too far away from the region of interest.

The number of events under the peak is determined by assuming that the amount of combinatoric background is linear in $K^-\pi^+\pi^+$ mass. Figure 5.3 also shows fits of the distribution with a Gaussian shape for the peak and a linear function for the combinatoric background. We can see that this linear parametrization of the shape of the background is modeled quite well.

All the backgrounds described up to now have been modeled with data. We are deliberately not relying on Monte Carlo simulations for this. This means that these background rates will have small systematic uncertainties due to any sort of modeling assumptions. There will, however, be significant statistical uncertainties, because our samples of continuum data and sideband events are limited.

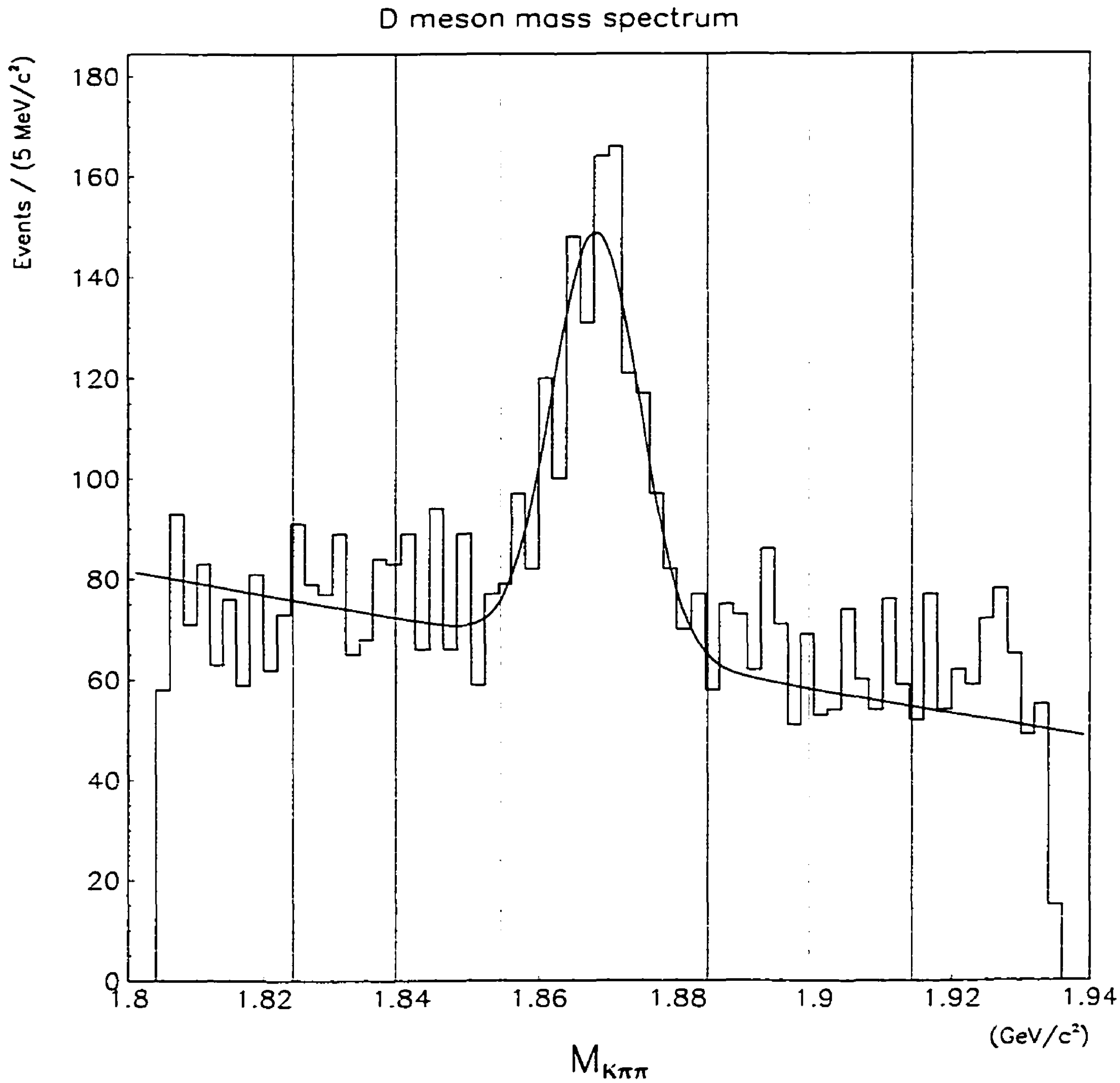

Figure 5.3: $K^-\pi^+\pi^+$ invariant distribution for events passing the $B^- \rightarrow D^+\pi^-e^-\bar{\nu}_e$ requirements in the generic Monte Carlo sample. The vertical lines indicate the central band signal region and the two sidebands used for the subtraction. We also show the fit to the histogram. We use a linear plus a Gaussian function for the fit.

5.2.4 Real *De* Backgrounds

After the previous step, the remaining backgrounds will have a real D, a real e, and a real neutrino, but may have either misidentified the extra pion or picked the wrong one from the event. Actually there are a few combinations that are possible. In the case of real $B^- \longrightarrow D^0 e^- \bar{\nu}_e$ decays we add an extra pion, in the case of $B^- \longrightarrow D_1^0 e^- \bar{\nu}_e$ events we either lose one pion or we lose two pions and gain one. In the case of $B^- \longrightarrow D^{*0} e^- \bar{\nu}_e$ events we always lose one pion and gain another one from the rest of the event.

We have two solutions to deal with this remaining background. The first method relies on our Monte Carlo sample. We simply tag events with a real D and e in them and then use these events to produce the B meson mass distribution using all the analysis cuts. This final distribution is then subtracted from the events that remain after the D sideband events have been removed. Section 5.3 describes extensively all the tests done to make sure that this is a valid method.

We also have a second method to extract this remaining background. It makes use of events formed by $D^+ \pi^+ e^-$, where the charge of the pion has been inverted with respect to the original analysis. This is the wrong sign pion sample. This type of sample is used when one is dealing with a combinatoric background of the type originating entirely from the "other" B in a $B\bar{B}$ event. This has to do with various charge correlations involved within the event, where one assumes that there are an equal number of positively charged tracks as there are negatively charged ones. If it can be shown that our background originates from a combinatoric π^- coming from the other B than an equivalent distribution can be generated using π^+s within the event coming similarly from the other B.

There are a few important considerations that have to be satisfied for right-sign/wrong-sign background symmetry to be valid, the first of these is that we are only dealing with $B\bar{B}$ background. Also the D and e must be correctly reconstructed and come from the same B. The other B's inclusive charge π spectrum must be charge symmetric. There should not be a significant misidentification of pions and kaons in the event. If all these conditions are satisfied then we should expect that this wrong sign parametrization of the background should work in our case. This is the case for background from the $B^- \to D^0 e^- \bar{\nu}_e$ and $B^- \to D^{*0} e^- \bar{\nu}_e$ decays, but unfortunately not in the case of $B^- \to D_1^0 e^- \bar{\nu}_e$ where there is one pion that gets lost and the other one is used in the reconstruction of the decay channel. There is also the question when the D and e come from different B's that we cannot answer with 100% certitude. Figure 5.4 shows the M_B distribution for right and wrong sign π. The two plots agree quite well except in the M_B signal region. From further studies, it turns out that the major part of this discrepancy is explained by the D^{**} events, including the D_1^0. Figure 5.5 is the same plot but now for the $M_{D\pi}$ distribution. Again we can see small discrepancies in this plot and they are explained by the D^{**}.

Based on these arguments it was tempting to use this method on data events because the whole analysis would not require any background estimates from Monte Carlo. Unfortunately, there were problems with this method. To work perfectly, it requires criteria described above which we could not satisfy. There would be a need for a more involved parametrization of the background than was originally imagined. We therefore did not use this method and concentrated on using the first method.

5.3 Sideband Studies

To make sure that the method outlined in the previous section gives us a reliable result we made several studies first to gain some confidence over its validity. First of all we did some Monte Carlo studies only using the generic Monte Carlo sample. The next step was to use the various sidebands in the data and compare these to our description of the background in the Monte Carlo.

More precisely, we have three types of sideband studies. First of all, we consider the D meson sidebands. These have been defined in Section 5.2.3 and are studied in Section 5.3.1. We then study the ΔE sidebands in Section 5.3.2. Of course, we work first of all with Monte Carlo events *only* and *then* with data sidebands. We then study the M_B sideband in Section 5.3.3 by looking at the ΔE distributions. As for the ΔE sidebands we first consider Monte Carlo events *only* and *then* look at the data M_B sideband. Finally in Section 5.3.4 we summarize the results of this section and give an overview of the results we obtained.

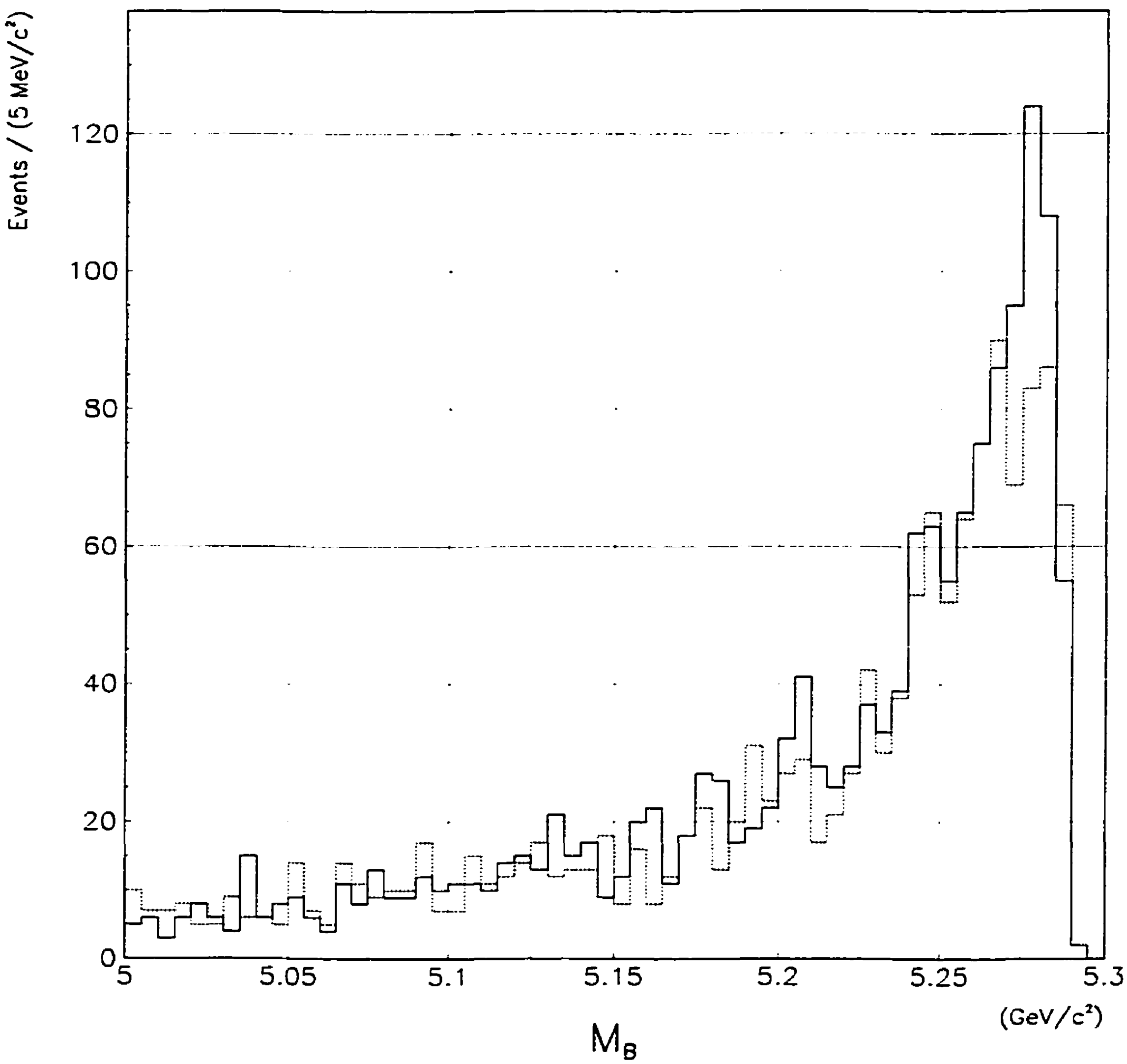

Figure 5.4: M_B plot comparing the right (full line) and wrong (dashed line) sign pion distribution.

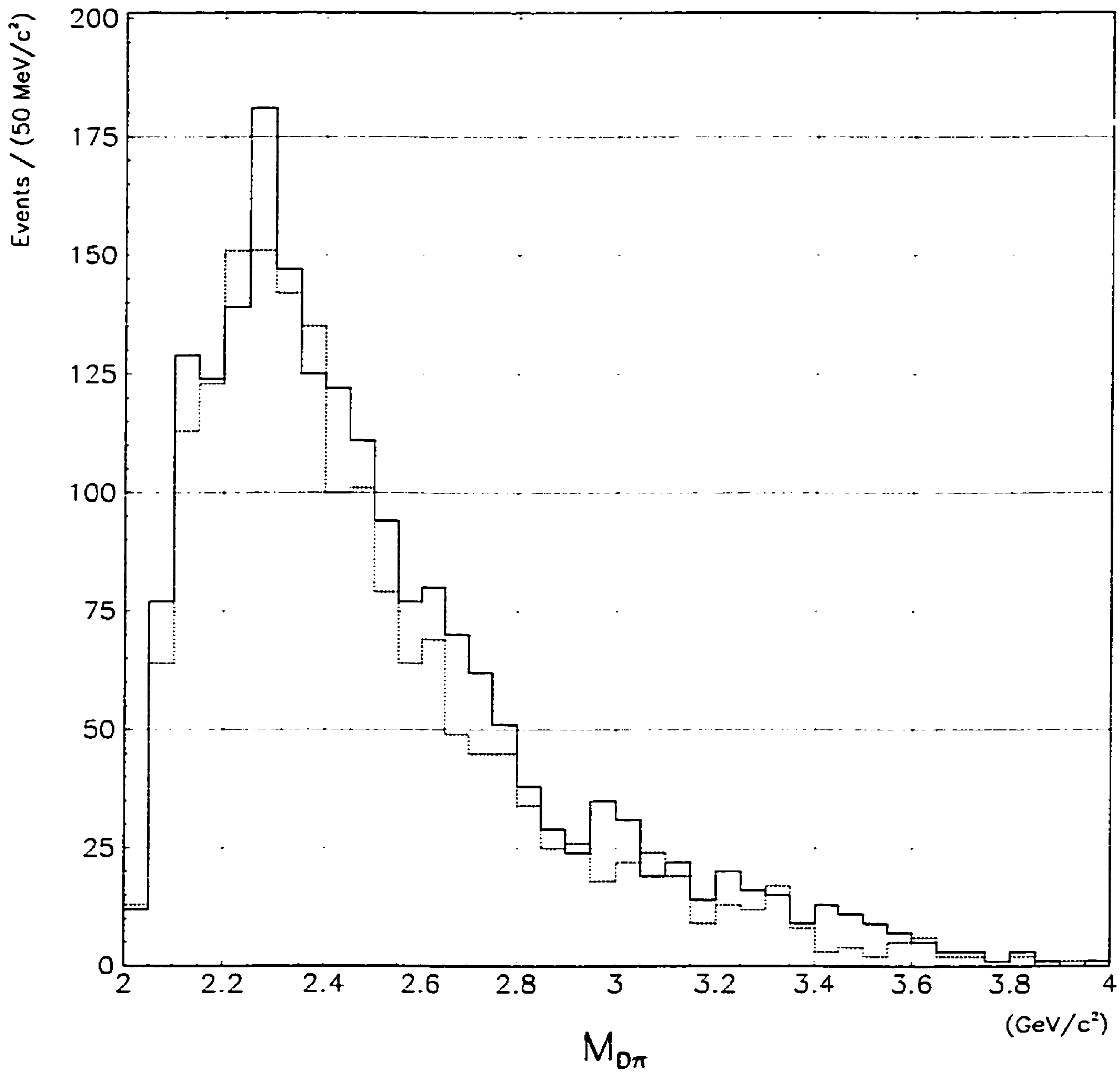

Figure 5.5: $M_{D\pi}$ plot comparing the right (full line) and wrong (dashed line) sign pion distribution.

5.3.1 D Sidebands

For the D sidebands we first look at the Monte Carlo sample. In Figure 5.6 we display how the D sidebands almost saturate the central band D background. All $B^- \to D^+\pi^-e^-\bar{\nu}_e$ have been vetoed in this Figure. The full line represents the central band D generic Monte Carlo. The dashed line represents the combined two Monte Carlo sidebands. The dotted line represents the D background tagged from the Monte Carlo. In Figure 5.7 the two background descriptions we intend to use (the D sidebands plot and the D's tagged from the Monte Carlo) are summed together and compared to our D central band Monte Carlo. As can be seen from this Figure these two plots agree very well. The overall normalization of the two plots is 1.03 which means that the two plots have a good agreement on the total number of events. Also the Kolmogorov test [51] used for similarity tests between the two different histograms gives a 84.4% probability that these two distributions have the same parent distribution. The probability measurement obtained from the Kolmogorov test should be interpreted in a similar manner as the probability given by the Equation 4.7. The value of the probability returned by the Kolmogorov test is calculated such that it will be uniformly distributed between zero and one for compatible histograms. As is the case here, these two plots therefore agree quite well. This is a big step forward for using this method as a way of parameterizing our backgrounds when it will come to extracting the signal contribution from the data.

Before we go ahead we would like to know what the composition of these D's tagged from the Monte Carlo sample is. We plot these in Figures 5.8 and 5.9. In both of these figures the full line represents the sum of all the individual components. As can be seen from Figure 5.8 the major source of these backgrounds comes from the well known decays $B^- \to D^{*0}e^-\bar{\nu}_e$ and $B^- \to D^0e^-\bar{\nu}_e$ (dashed and dotted line respectively). This is a good thing to know since we are confident about the way these decays have been generated. In Figure 5.9 we show the other type of backgrounds not as well modeled by our Monte Carlo, the $B^- \to D^{**}e^-\bar{\nu}_e$ and the other non-resonant semileptonic decays plus the secondary lepton channels. These are quite small when compared to the others and will inflict only a minimal inaccuracy on our final result. We shall consider these channels again in more detail later on when estimating the

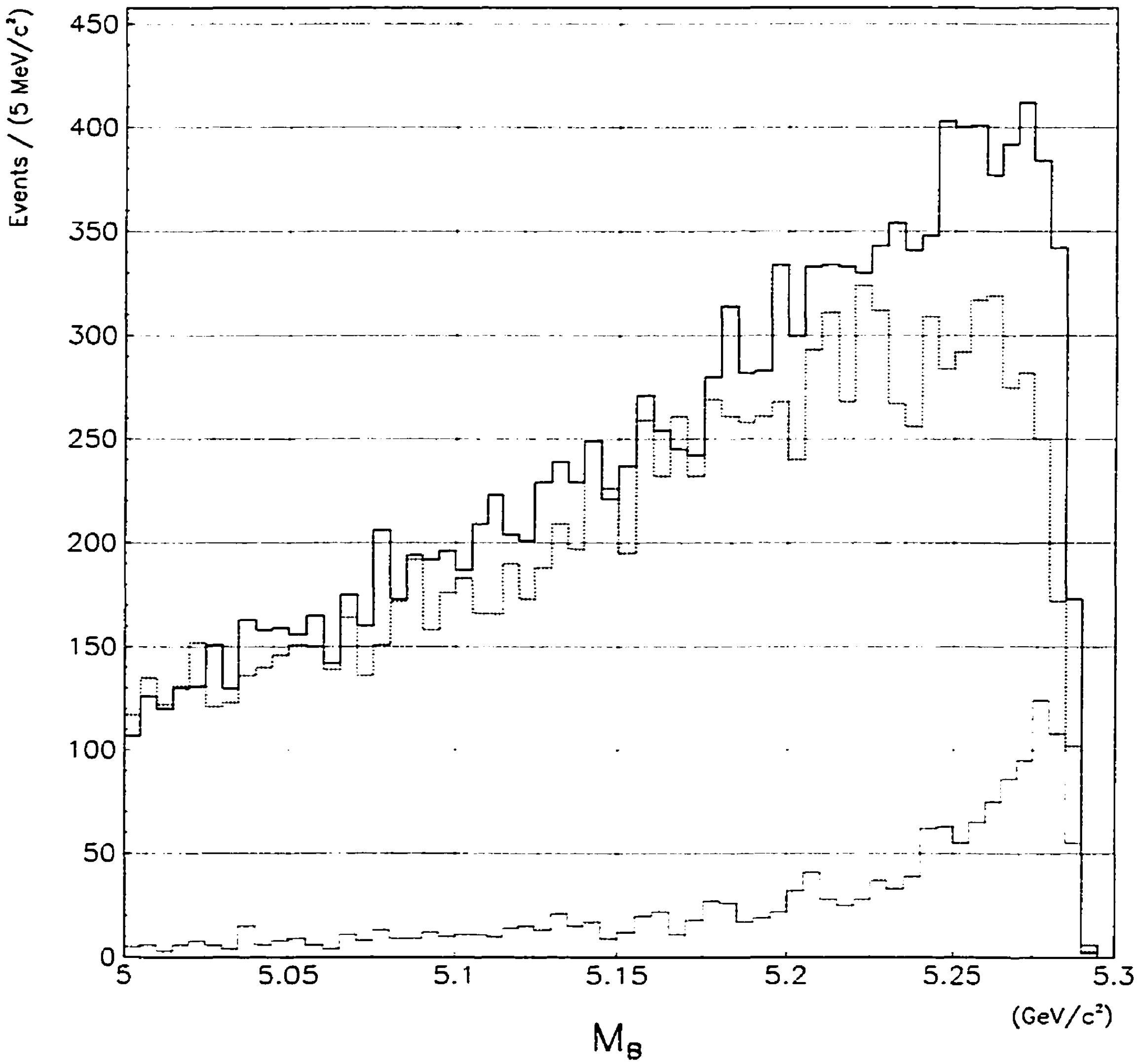

Figure 5.6: M_B plot for the Monte Carlo distribution of D central band (full line), D sideband (dashed line), and tagged Monte Carlo D (dotted line).

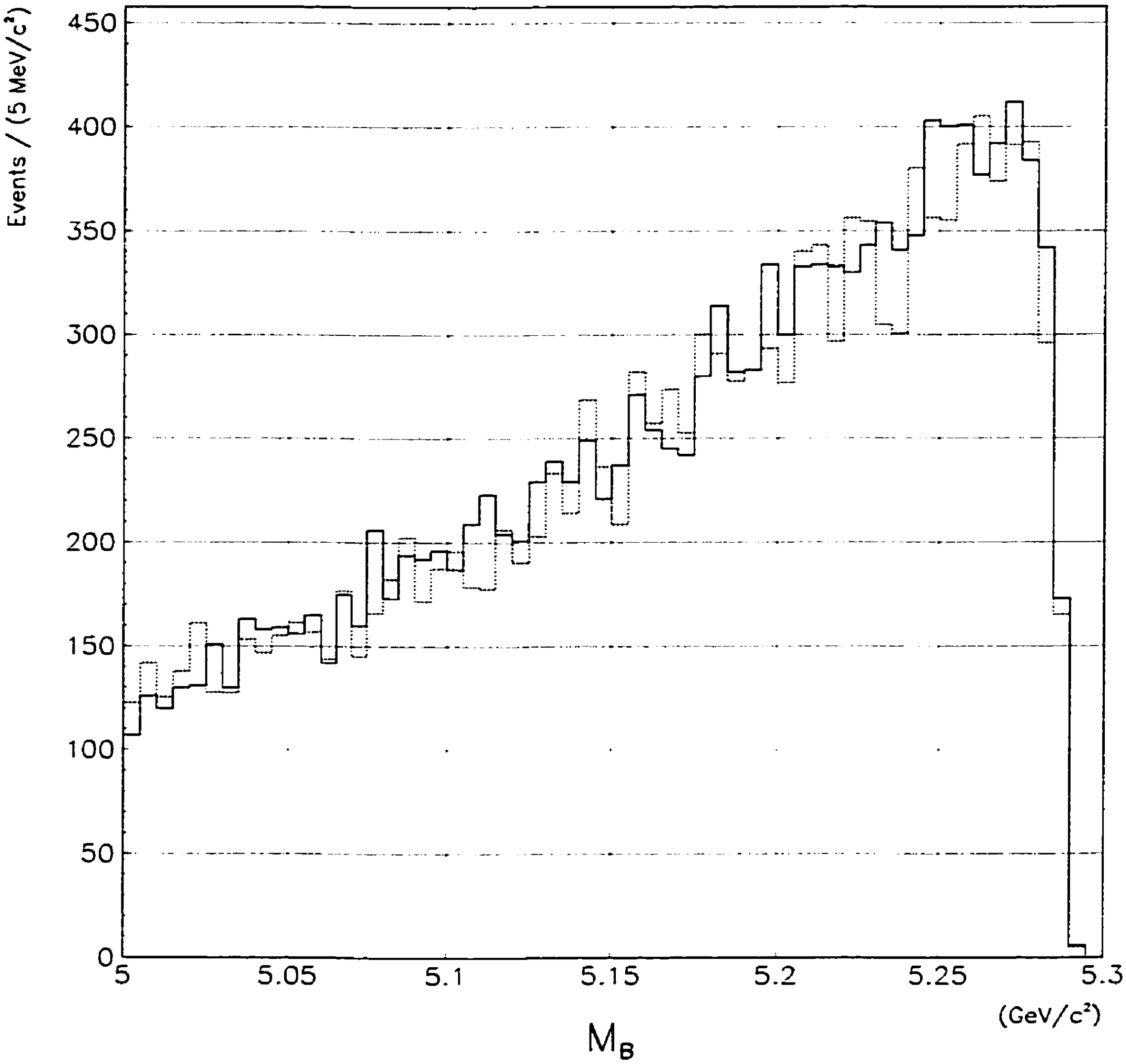

Figure 5.7: M_B plot for the Monte Carlo distribution of D central band (full line), and the sum of sidebands and tagged D's (dashed line). The two plots agree very well when comparing their shape and normalization.

systematic errors on our measurement.

So overall these D sideband studies made us more confident about the validity of using the proposed method for parameterizing the remaining backgrounds. We are also confident about the use of the Monte Carlo sample since the major channels have been studied extensively before and are thus well known. Moreover, our Monte Carlo models these decays quite well. We therefore go ahead with this method and look at the other sideband distributions before we use this method on the data sample for the final measurement.

5.3.2 ΔE Sidebands

The ΔE sideband also has two components, a positive sideband $0.4 < \Delta E < 0.8$ and a negative sideband $-0.8 < \Delta E < -0.4$. The combination of these two sidebands has to be scaled down by 0.5 when comparing these with the central band ΔE region defined as $-0.2 < \Delta E < 0.2$.

It is expected that these two sidebands will have different physical events contributing. So we will study each of these sidebands separately. First the positive ΔE sideband, which is shown in Figure 5.10. It is a M_B plot where we look only for events in the selected region corresponding to $0.4 < \Delta E < 0.8$. The full line corresponds to the D central band and the dashed line to the D sidebands. The dotted line corresponds to the tagged D^+ events. In Figure 5.11 we add up the dashed and dotted curves, representing our background description in this ΔE region and compare it to the signal region, again in this ΔE region. Both curves agree quite well. The similarity probability given by the Kolmogorov test is 72.7%. The normalization factor in this case is 1.03.

The negative sideband is shown in Figure 5.12. Again each line has the same meaning as before. In this case it can be seen that the contribution from the tagged D backgrounds is more important than in the previous case. In Figure 5.13 we add up again the two curves describing the backgrounds in this ΔE sideband and compare it to the corresponding D central band signal region. From the Kolmogorov similarity test we obtain a probability of 50.9% and an overall normalization scaling of 1.02.

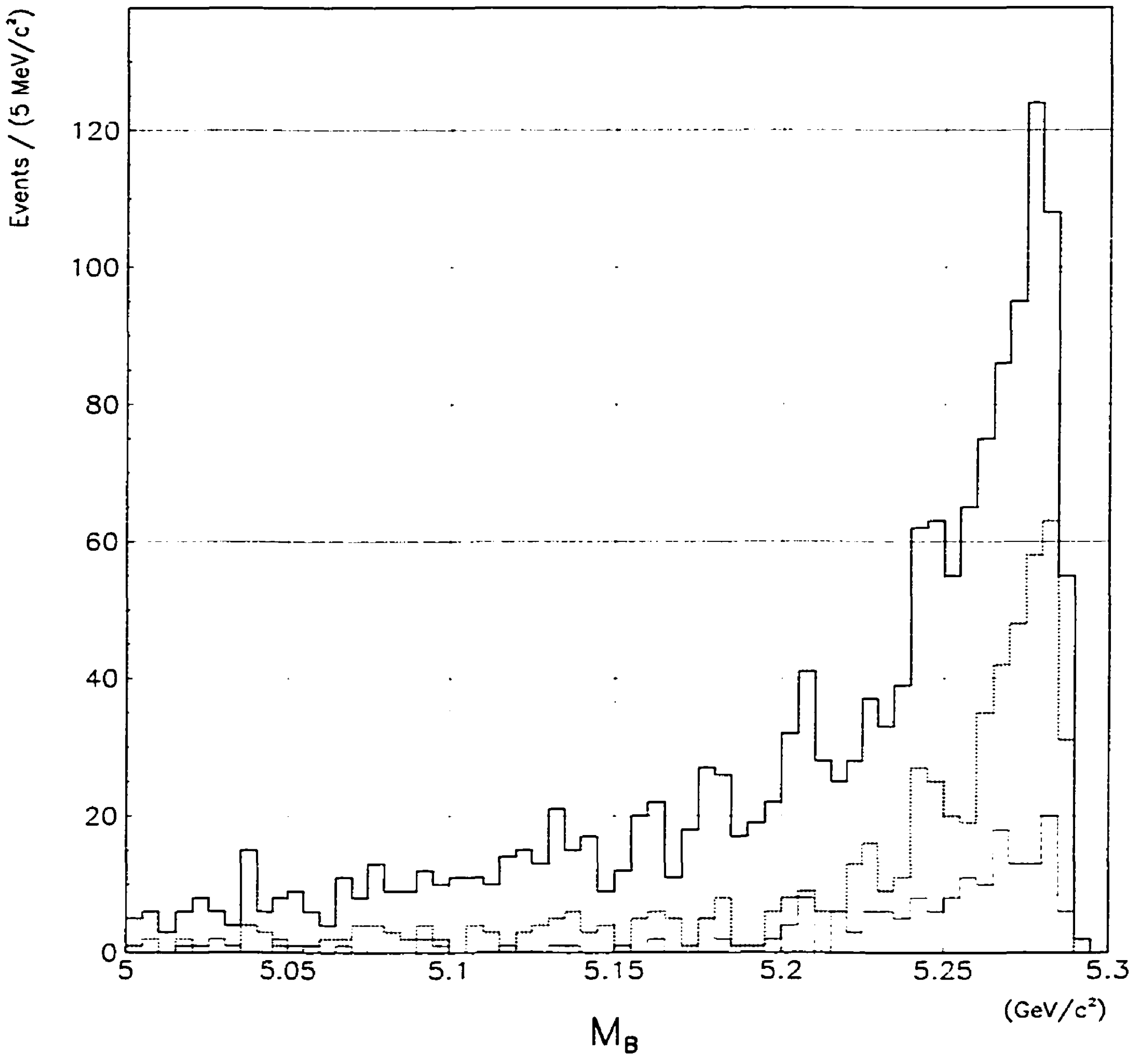

Figure 5.8: Detailed description of our well understood tagged Monte Carlo D's. The full line represents the sum of all the contributions. The dashed line is for $B^- \longrightarrow D^{*0}e^-\bar{\nu}_e$ contribution and the dotted line is for $B^- \longrightarrow D^0e^-\bar{\nu}_e$ contribution.

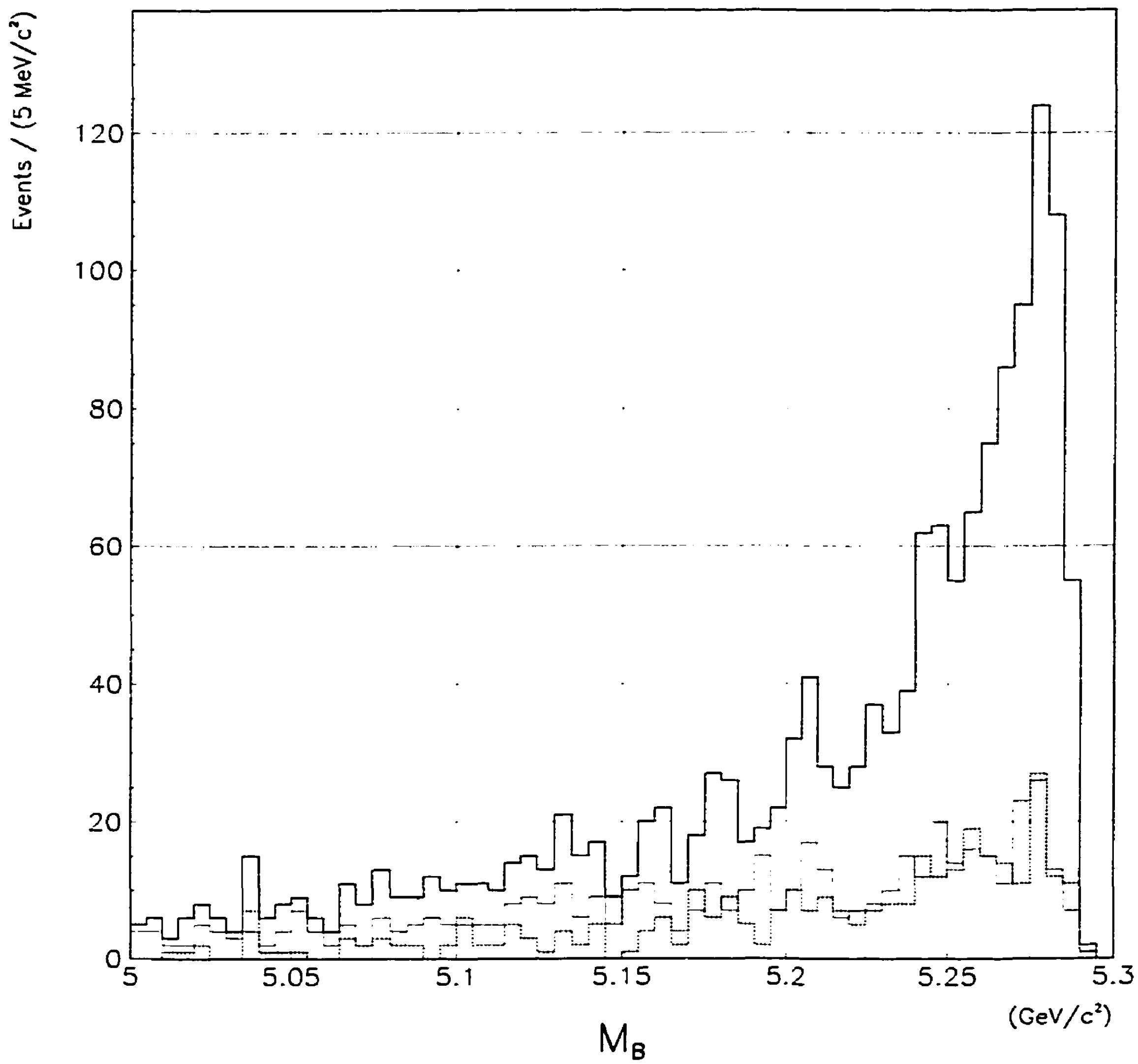

Figure 5.9: Detailed description of our less understood tagged D's. The full line represents the sum of all the contributions. The dashed line is for $B^- \longrightarrow D_1^0 e^- \bar{\nu}_e$ contribution and the dotted line is for the other non-resonant semileptonic decays and secondary lepton channels contributions.

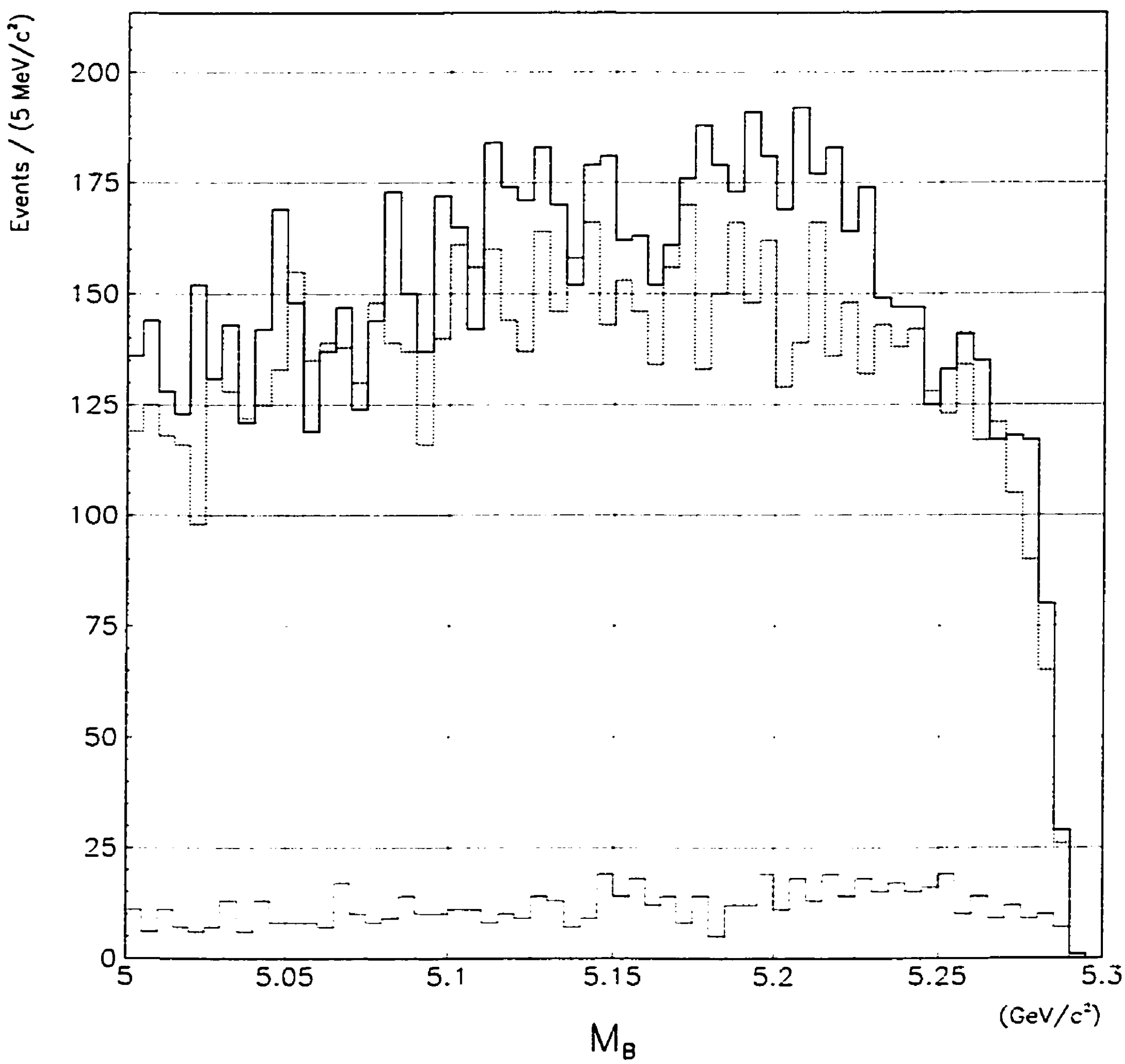

Figure 5.10: M_B plot for the Monte Carlo positive ΔE sideband, $0.4 < \Delta E < 0.8$. The full line represents the D central band, the dashed line is the D sideband and the dotted line is the tagged Monte Carlo D.

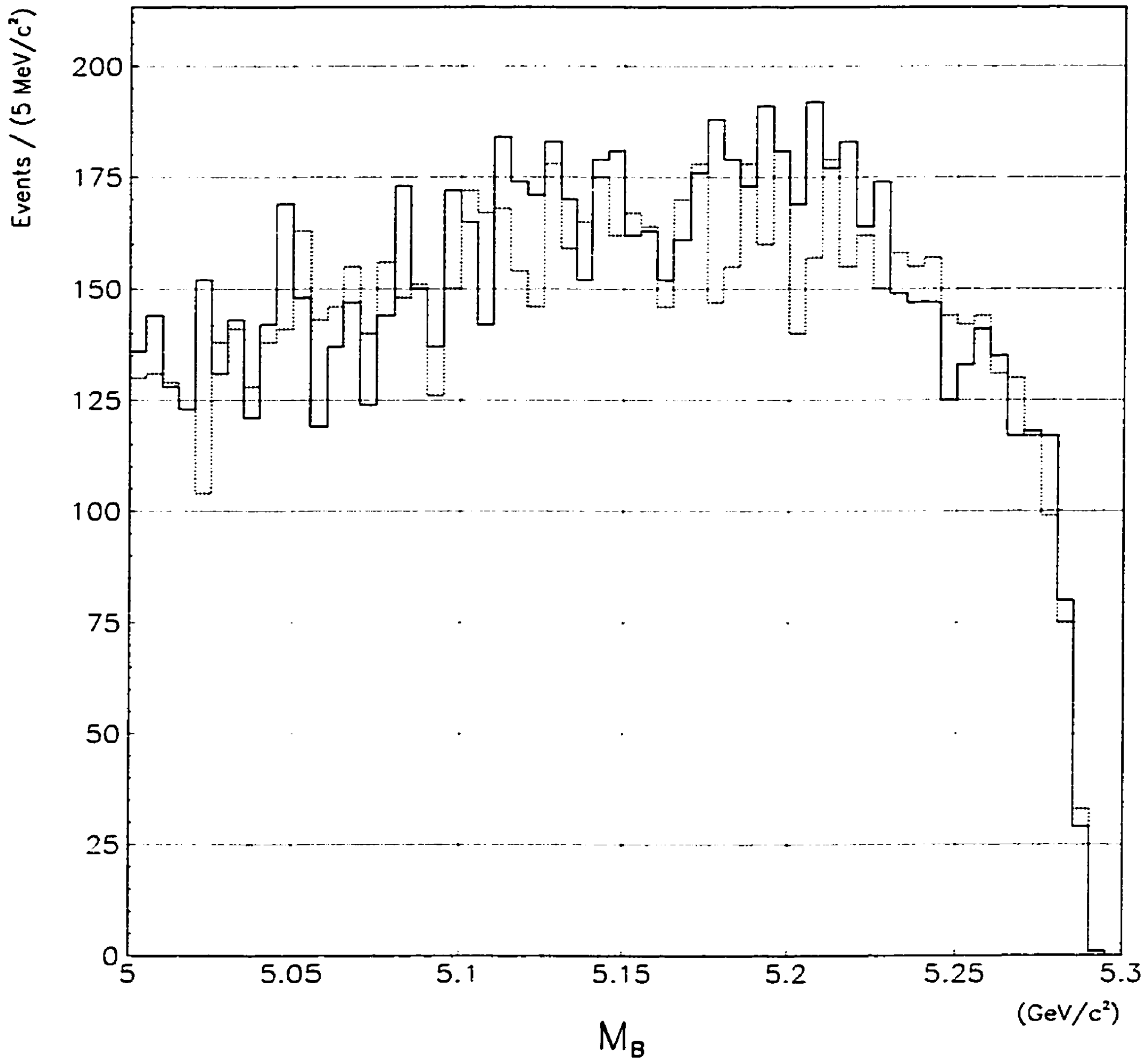

Figure 5.11: M_B plot for the Monte Carlo positive ΔE sideband, $0.4 < \Delta E < 0.8$ of D central band (full line), and the sum of sidebands and tagged D's (dashed line). The two plots agree very well when comparing their shape and normalization.

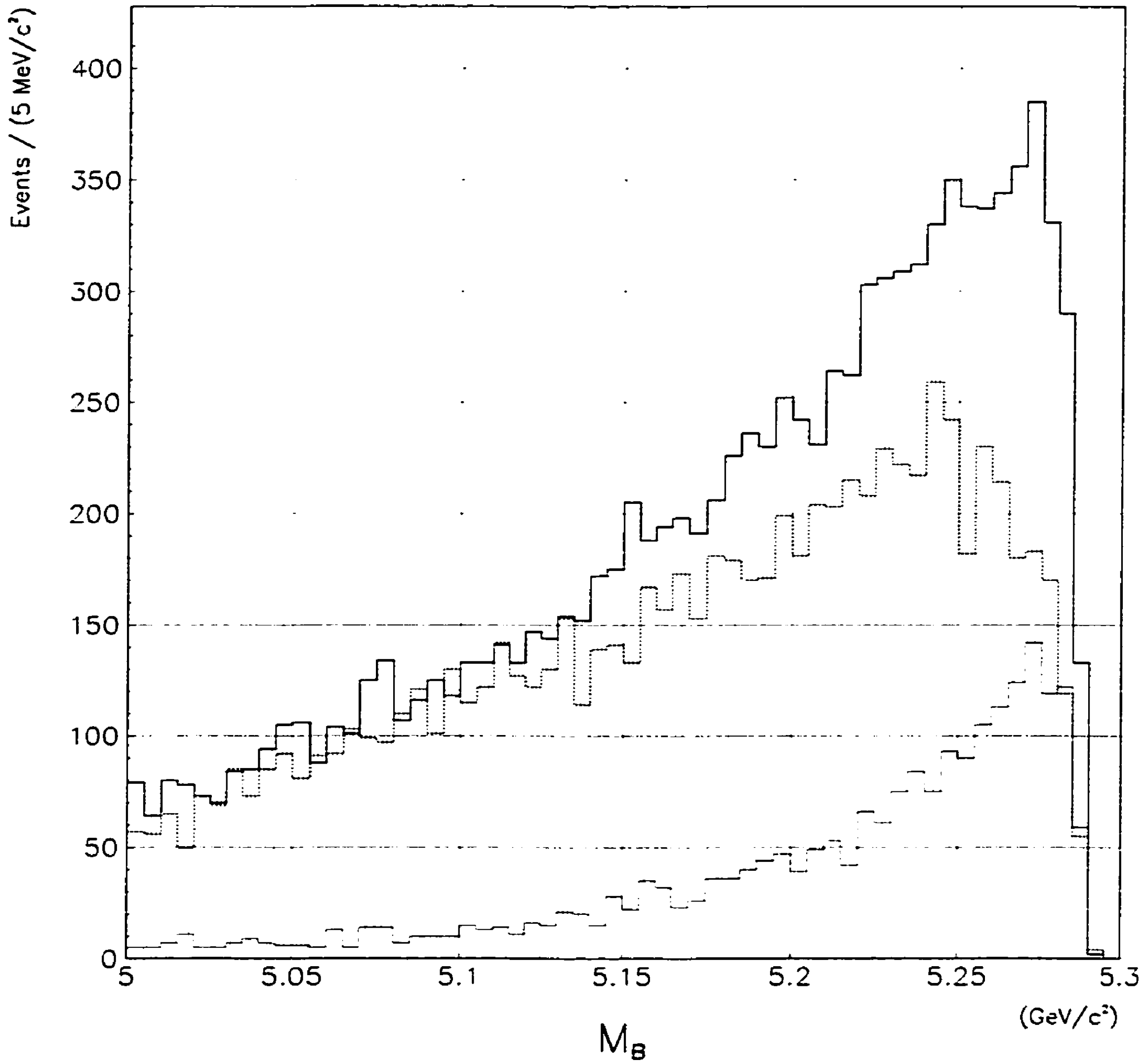

Figure 5.12: M_B plot for the Monte Carlo negative ΔE sideband, $-0.8 < \Delta E < -0.4$. The full line represents the D central band, the dashed line is the D sideband and the dotted line is the tagged Monte Carlo D.

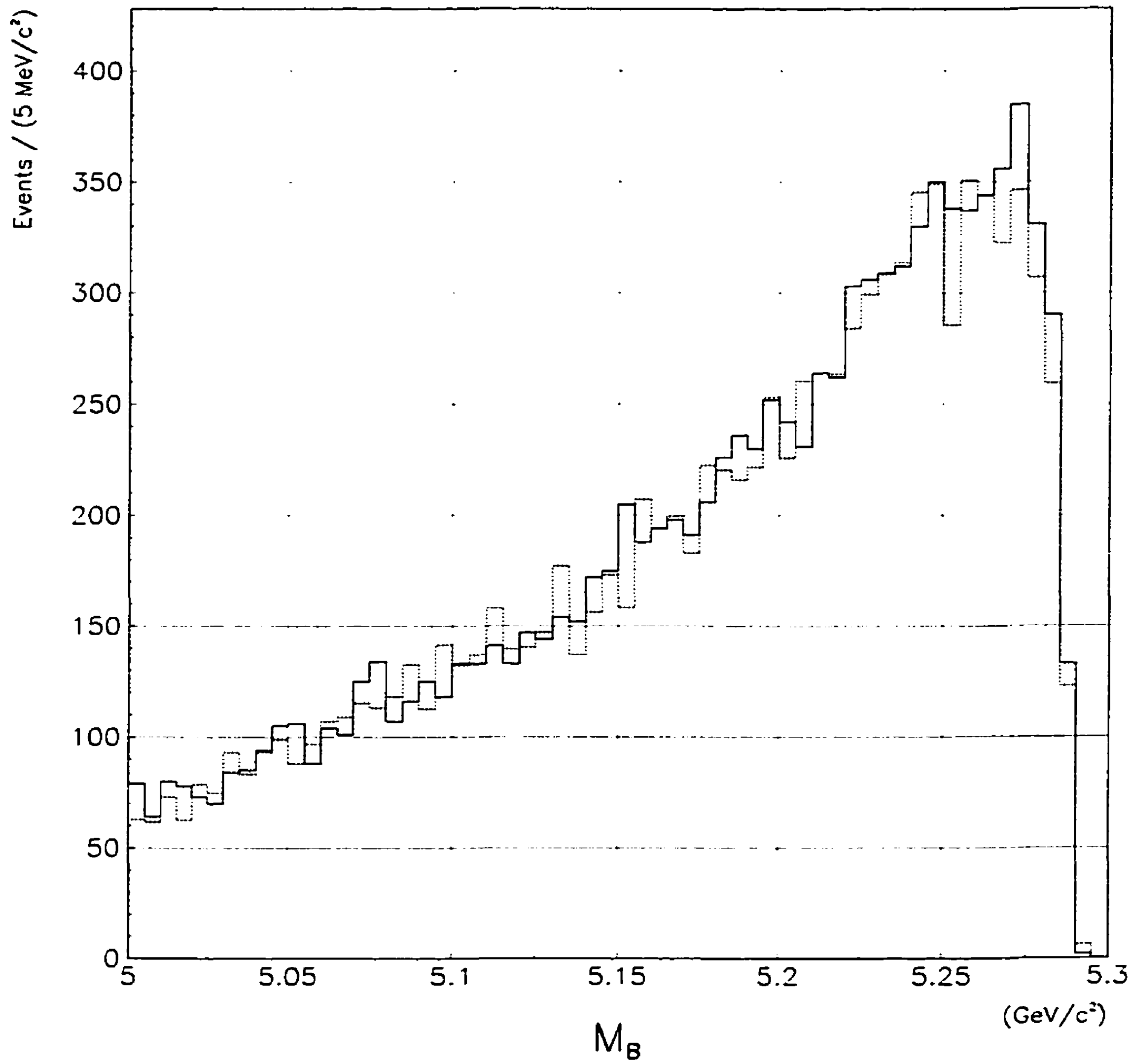

Figure 5.13: M_B plot for the Monte Carlo negative ΔE sideband, $-0.8 < \Delta E < -0.4$ of D central band (full line), and the sum of sidebands and tagged D's (dashed line). The two plots agree very well when comparing their shape and normalization.

As can be seen both ΔE sidebands agree quite well.

We now also look at the ΔE sidebands in the data sample and compare them again to our method outlined for dealing with the backgrounds. This means that in this case we will use the data D sidebands from the corresponding ΔE region with the tagged D's sample from this same ΔE region from the generic Monte Carlo sample. Since we are dealing with data events, both samples (the central band D's as well as the sideband D's) have to be corrected for continuum events. We perform the same subtraction as outlined in Section 5.2.1, again considering the respective ΔE sideband when doing this subtraction. These two final curves will then be the background to our signal in the ΔE sideband.

In Figure 5.14 we have the positive ΔE sideband. The full, dashed and dotted lines represent respectively the D central band, the D sidebands and the tagged Monte Carlo D events. This Monte Carlo sample has to be scaled to our data set since we have ~ 5 times more MC events than data events. The exact scaling using the luminosities of each sample is 0.2031 which is used whenever we scale the MC to the data. Figure 5.15 shows the positive ΔE sideband signal plot overlayed with our description of the backgrounds. Due to the scaling of the Monte Carlo sample to the data sample the Kolmogorov test is not applicable. We only have the overall normalization factor available as a comparison for these two curves. The scaling is 1.02 which is again a very good agreement between the two distributions.

In Figure 5.16 we have the negative ΔE sideband. Each line has the same meaning as in Figure 5.14. We add up the two lines describing our backgrounds in this ΔE sideband and overlay it on top of the central band D's describing our signal in this region in Figure 5.17. The overall normalization factor for this plot is 1.11 which is slightly worse than the other tests, but still in good agreement.

5.3.3 M_B Sidebands

The M_B sideband is defined as the region between $5.0 < M_B < 5.2$. It is quite away from the region where one would expect a B meson but if we can have a good agreement in this region using our background parameterization then we can be

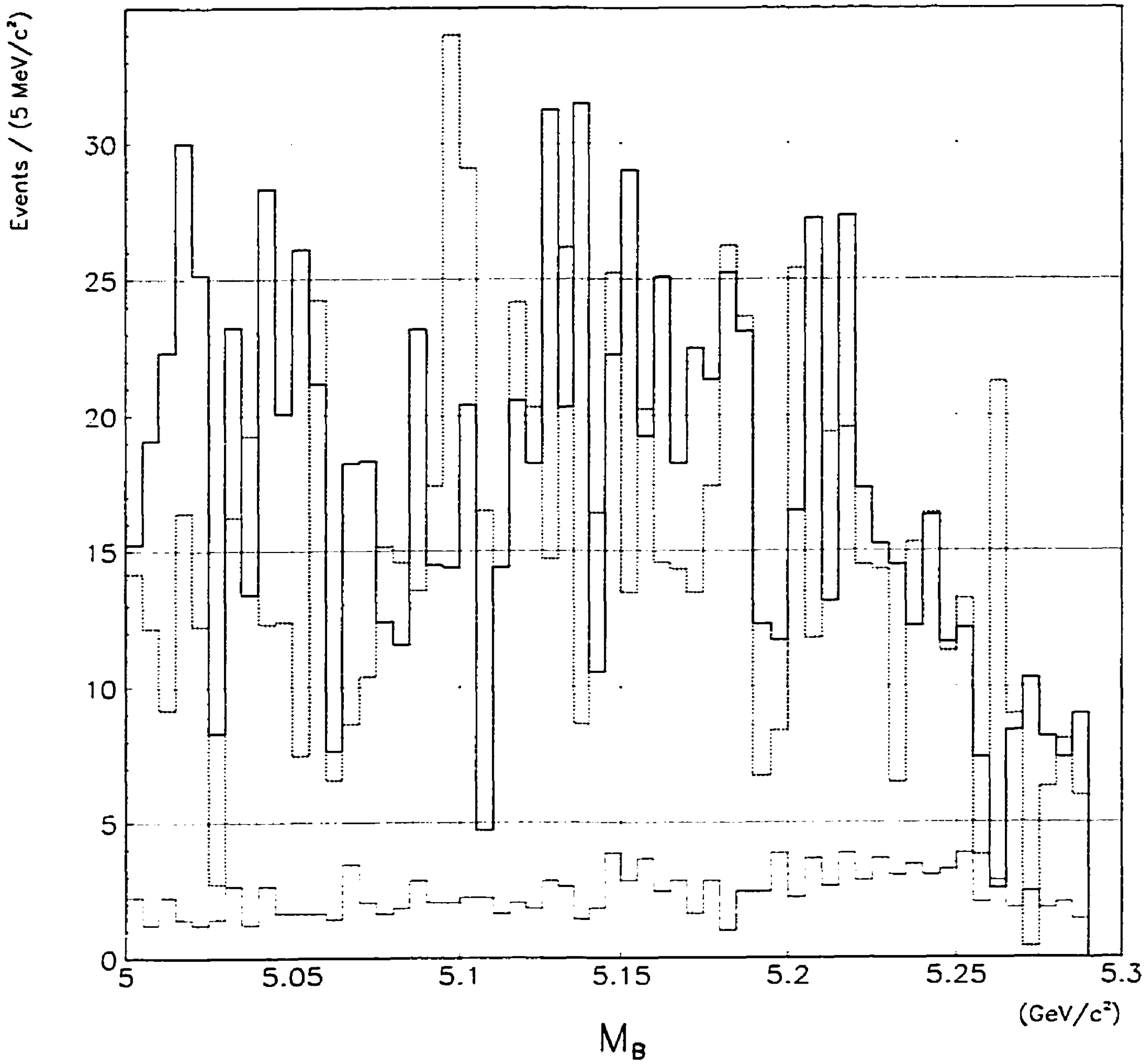

Figure 5.14: M_B plot for the data positive ΔE sideband, $0.4 < \Delta E < 0.8$. The full line represents the D central band in the data sample, the dashed line is the D sideband in the data sample and the dotted line is the tagged Monte Carlo D sample.

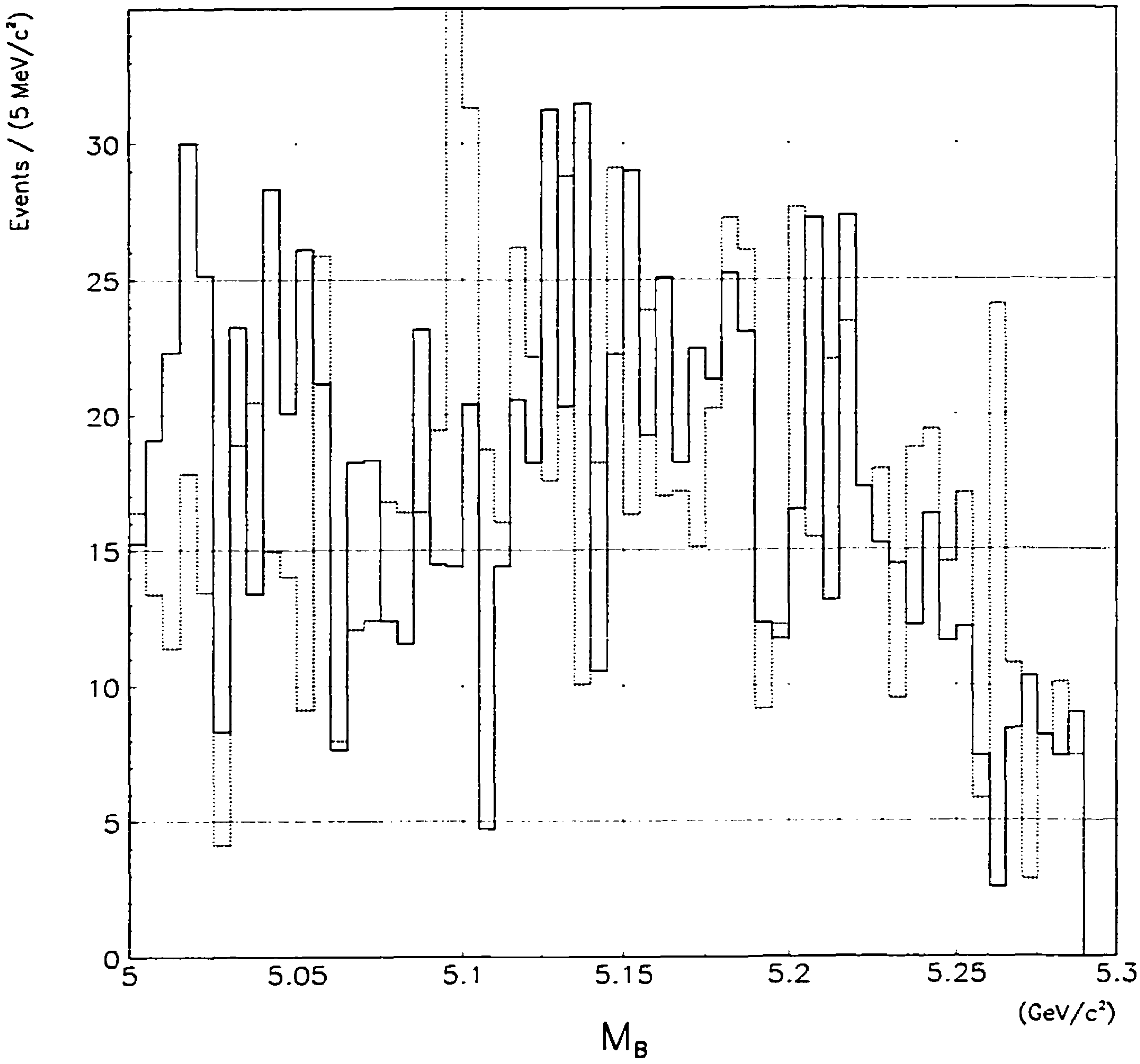

Figure 5.15: M_B plot for the data positive ΔE sideband, $0.4 < \Delta E < 0.8$ of D central band (full line), and the sum of the data sidebands and tagged Monte Carlo D's (dashed line).The two plots agree very well when comparing their normalization.

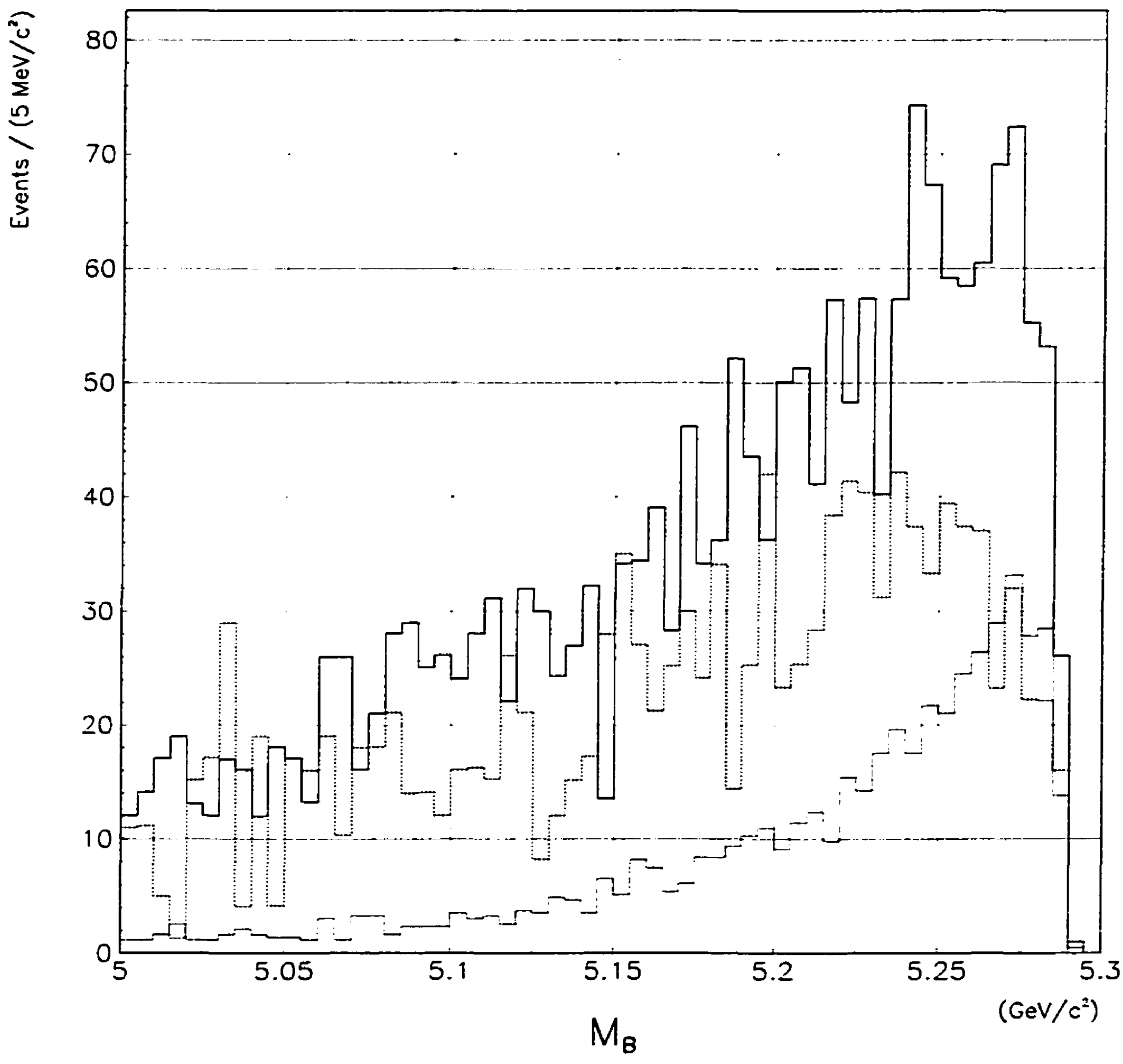

Figure 5.16: M_B plot for the data negative ΔE sideband, $-0.8 < \Delta E < -0.4$. The full line represents the D central band in the data sample, the dashed line is the D sideband in the data sample and the dotted line is the tagged Monte Carlo D.

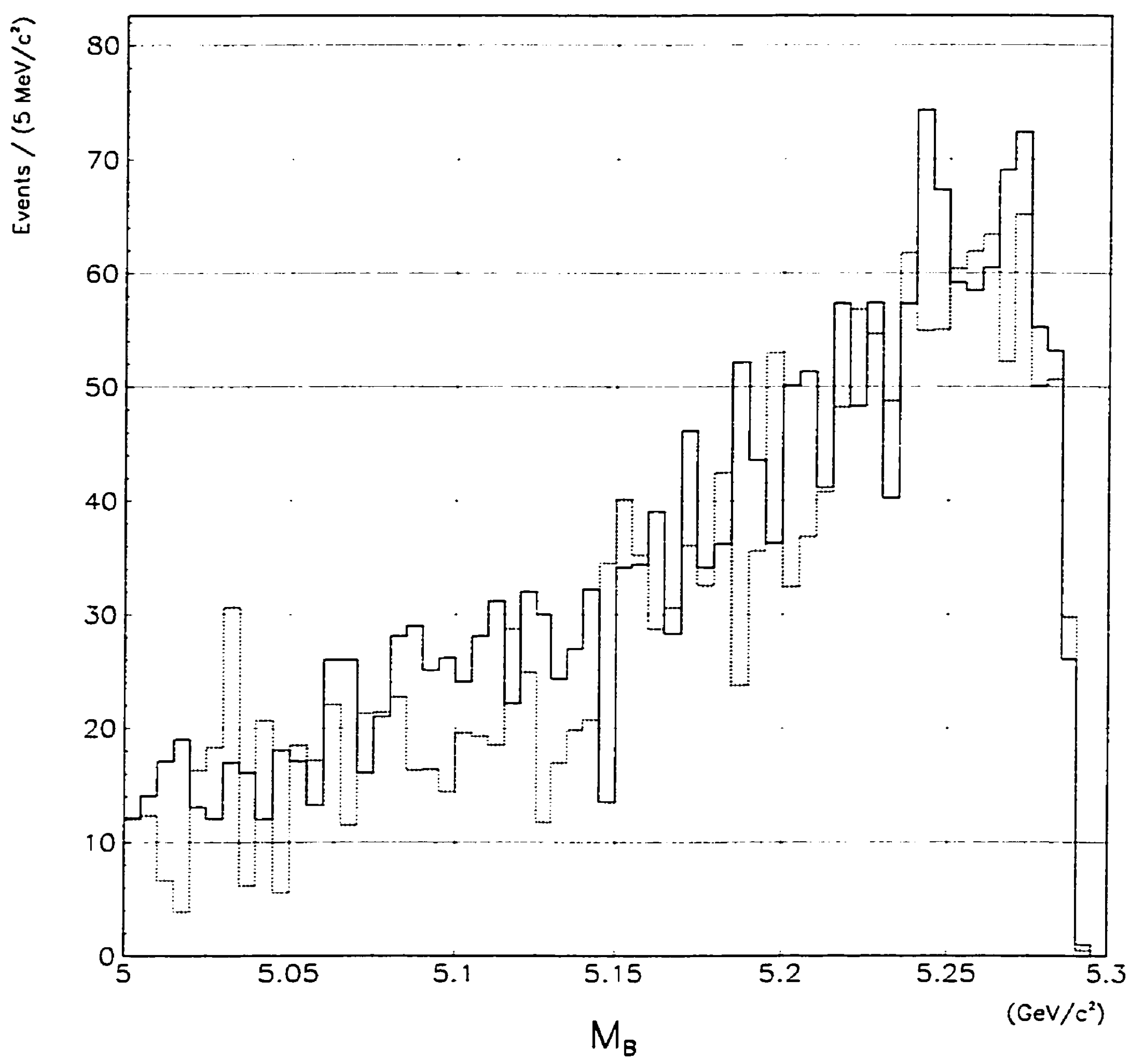

Figure 5.17: M_B plot for the data negative ΔE sideband, $-0.8 < \Delta E < -0.4$ of D central band (full line), and the sum of the data sidebands and tagged Monte Carlo D's (dashed line). The two plots agree very well when comparing their normalization.

confident that the signal region will be well modeled too. For this step we do all the analysis cuts except the ΔE cut which we plot here for the study.

In Figure 5.18 we have the plot for Monte Carlo events where we parameterize the backgrounds as explained before. The full line is the D central band and the dashed line represents the D sidebands. The dotted curve is for the Monte Carlo tagged D's found in this M_B sideband. As before we add up the two background curves and compare them to the signal curve in Figure 5.19. The full line is is the signal and the dashed line is the background. The Kolmogorov probability is 23% that these two distributions are coming from the same originating parent distribution and the overall scaling between these two plots is of 1.02 which is a good agreement.

We then do the same exercise but for the data M_B sideband. Figure 5.20 shows the corresponding curves that have the same meaning as before. The scaling of the tagged D Monte Carlo events is scaled by the factor 0.2031 to take into account the difference of the two sample sizes. Figure 5.21 then compares the overall background shape to the signal shape for this sideband. The Kolmogorov test doesn't work here for the same reason as in the case of the ΔE sideband, due to the relative scaling of the MC sample. The overall normalization factor for these two plots is 1.01 which is very good.

For completeness we also look at the actual signal M_B region in the Monte Carlo only. Figure 5.22 shows the various components for the background parameterization. Here no scaling is necessary when plotting the tagged D Monte Carlo events since it comes from the same sample of events as the D sideband events. Summing these two background contributions and overlaying them over the signal central band D's we obtain Figure 5.23. Here the Kolmogorov similarity test gives us a probability of 36% that these two distributions are the same and the overall normalization scaling is 1.01 which is very good again.

5.3.4 Conclusion About Background And Sideband Studies.

We summarize the procedures detailed above. The method we proposed to extract the signal out of the data sample was to characterize our background. We did this by using

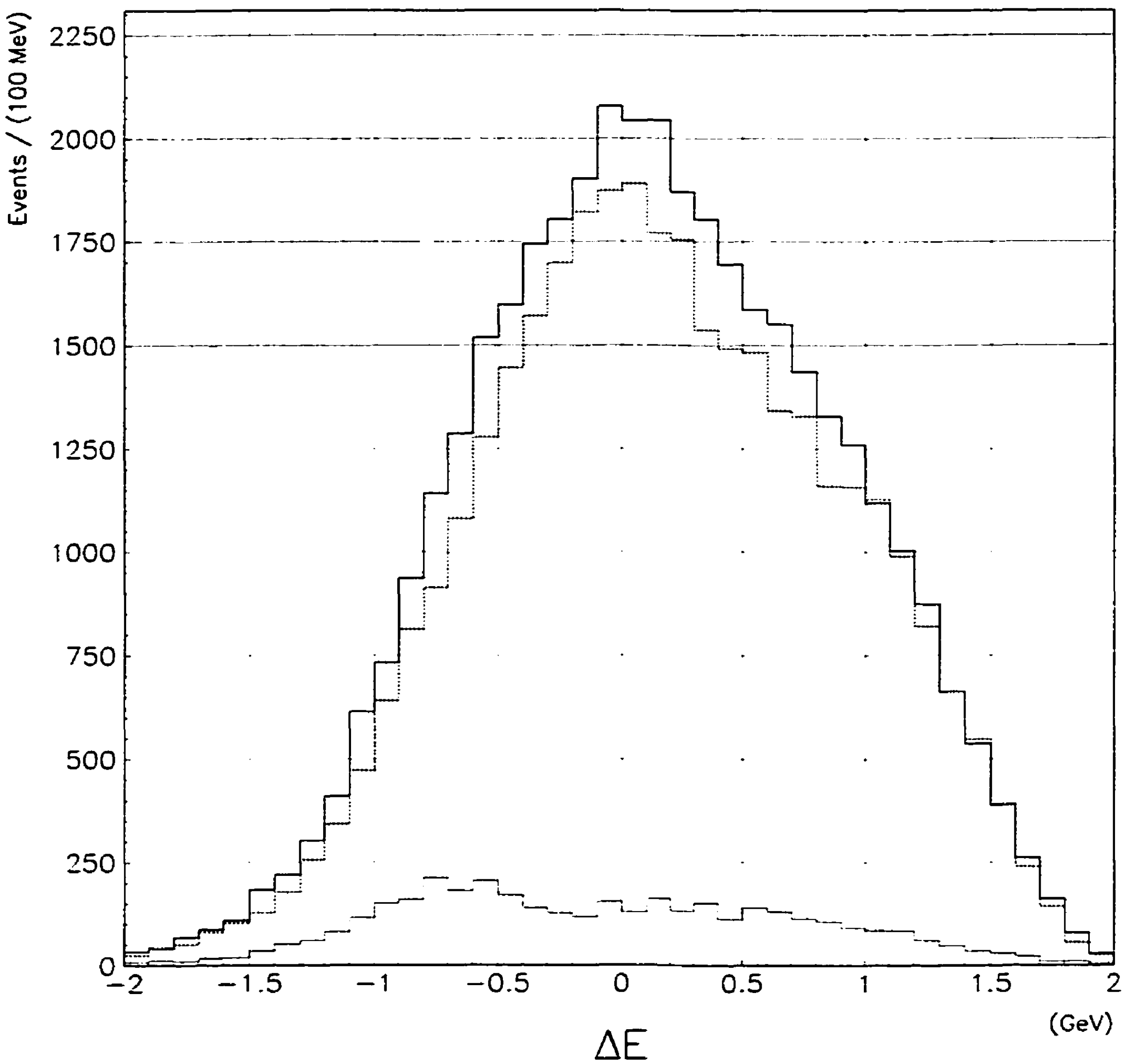

Figure 5.18: ΔE plot for the Monte Carlo M_B sideband. The full line represents the D central band, the dashed line is the D sideband and the dotted line is the tagged Monte Carlo D.

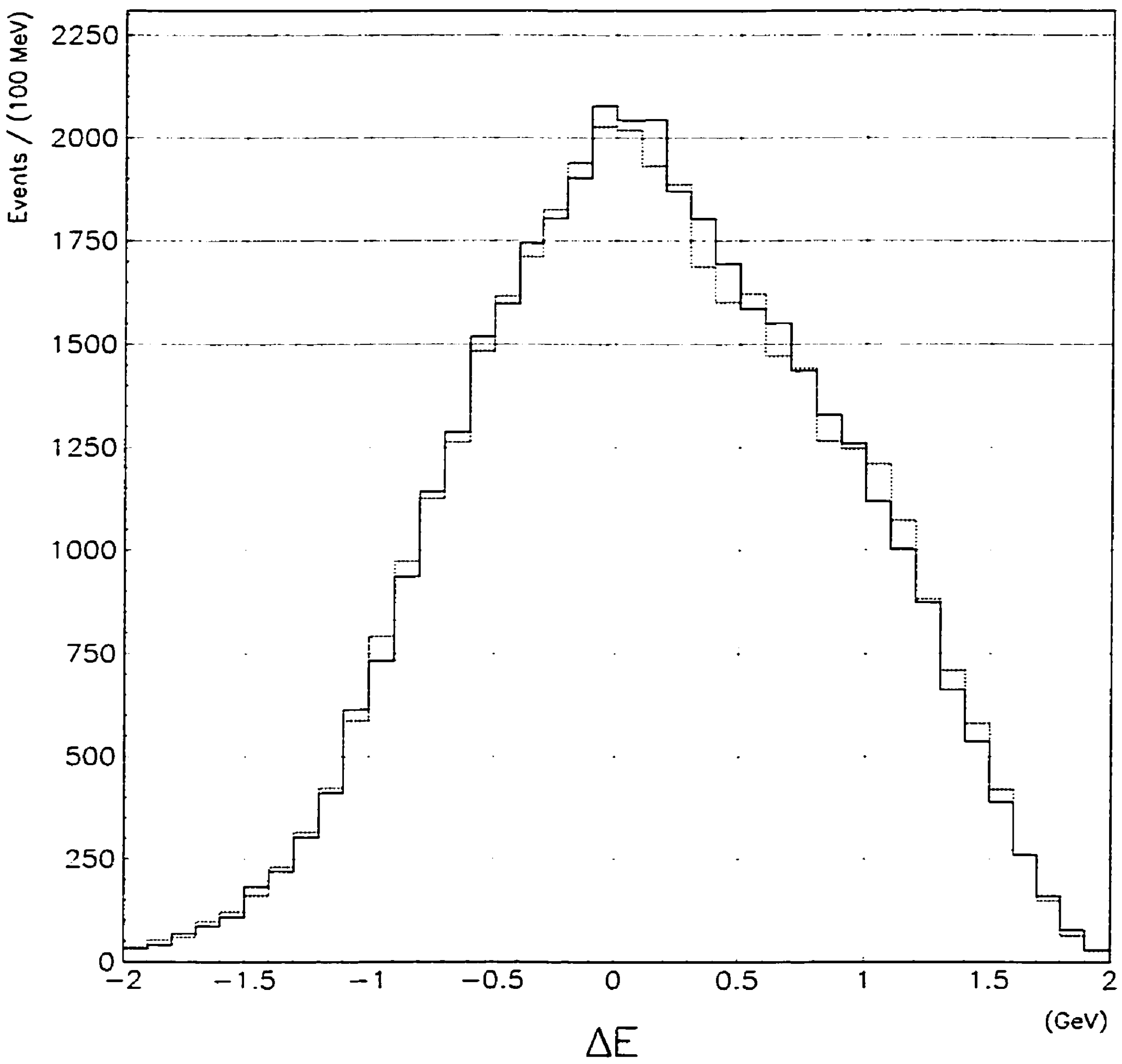

Figure 5.19: ΔE plot for the Monte Carlo M_B sideband of the D central band (full line), and the sum of sidebands and tagged Monte Carlo D's (dashed line). The two plots are in good agreement when comparing their shape and normalization.

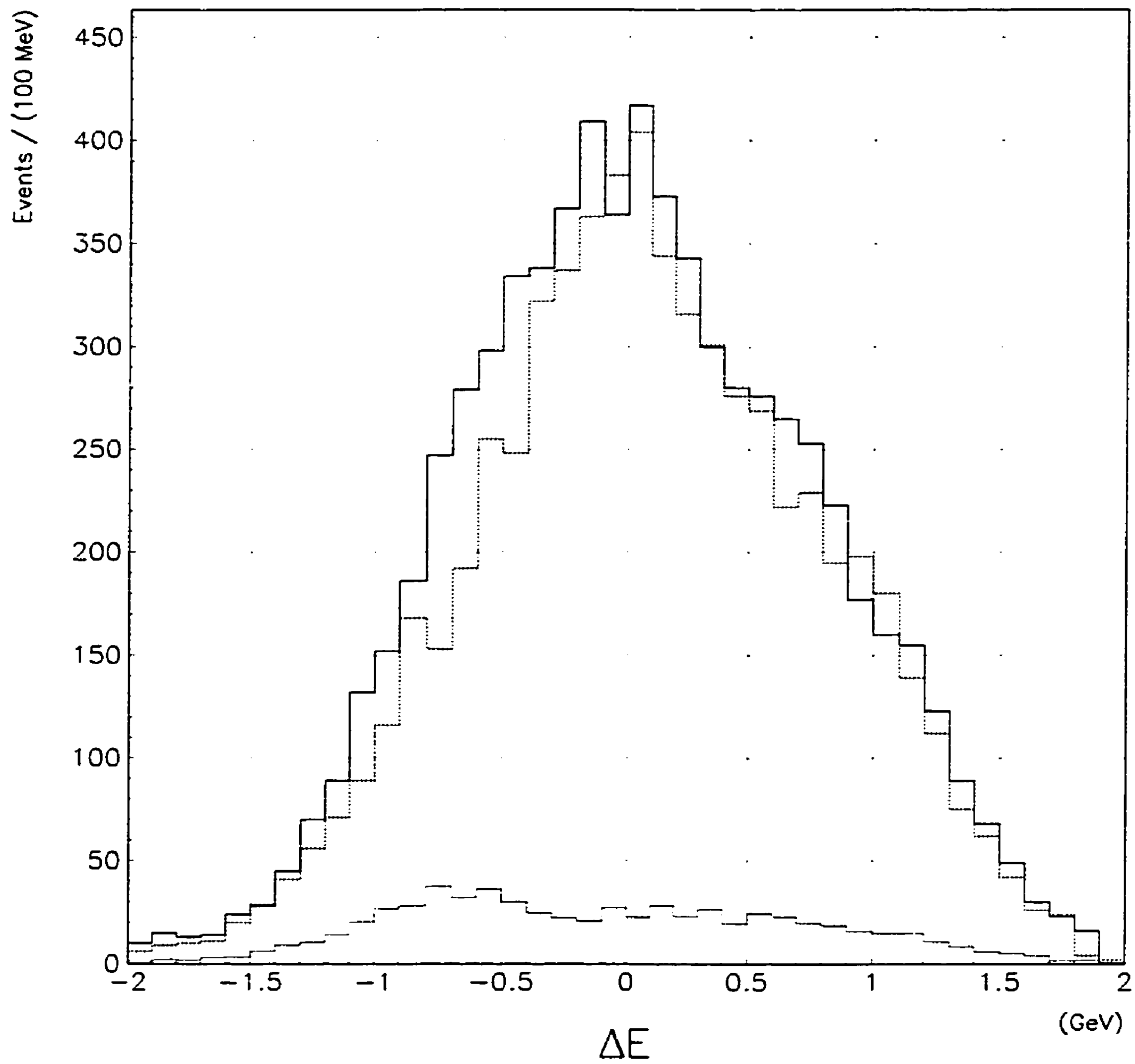

Figure 5.20: ΔE plot for the data M_B sideband. The full line represents the D central band in the data sample, the dashed line is the D sideband in the data sample and the dotted line is the tagged Monte Carlo D.

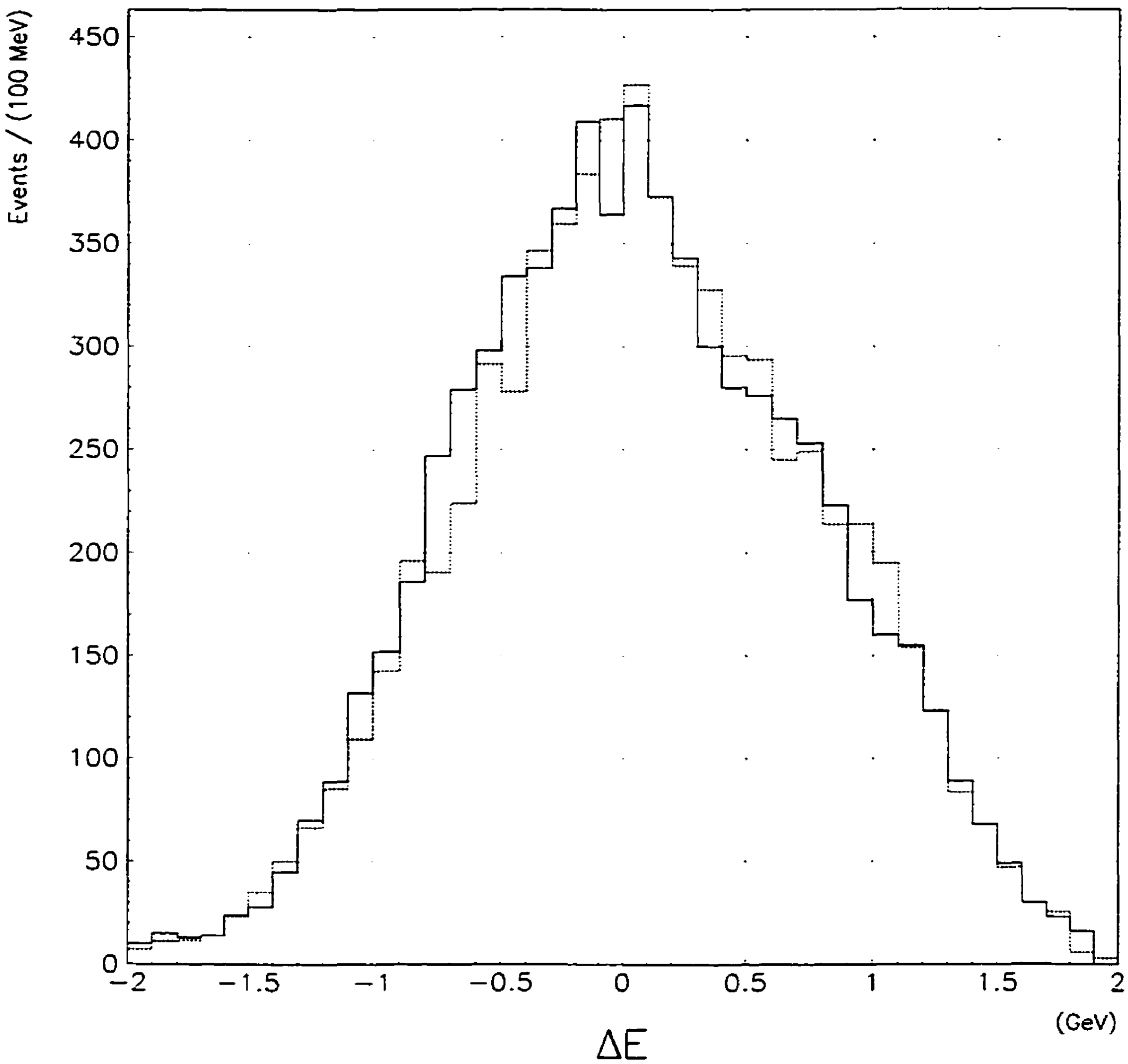

Figure 5.21: ΔE plot for the data M_B sideband of of D central band (full line), and the sum of the data sidebands and tagged Monte Carlo D's (dashed line). The two plots are in good agreement when comparing their normalization.

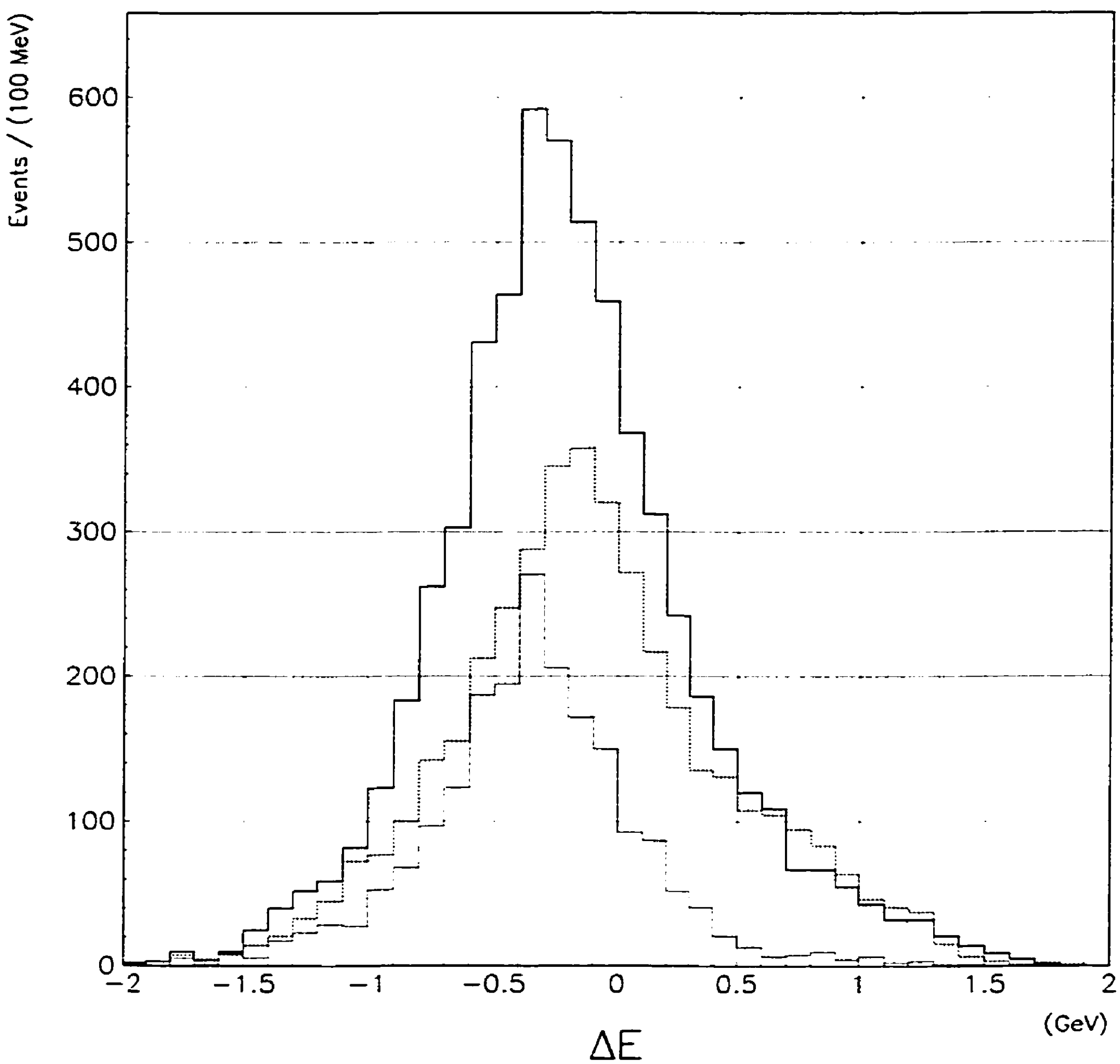

Figure 5.22: ΔE plot for the Monte Carlo M_B signal band. The full line represents the D central band, the dashed line is the D sideband and the dotted line is the tagged Monte Carlo D.

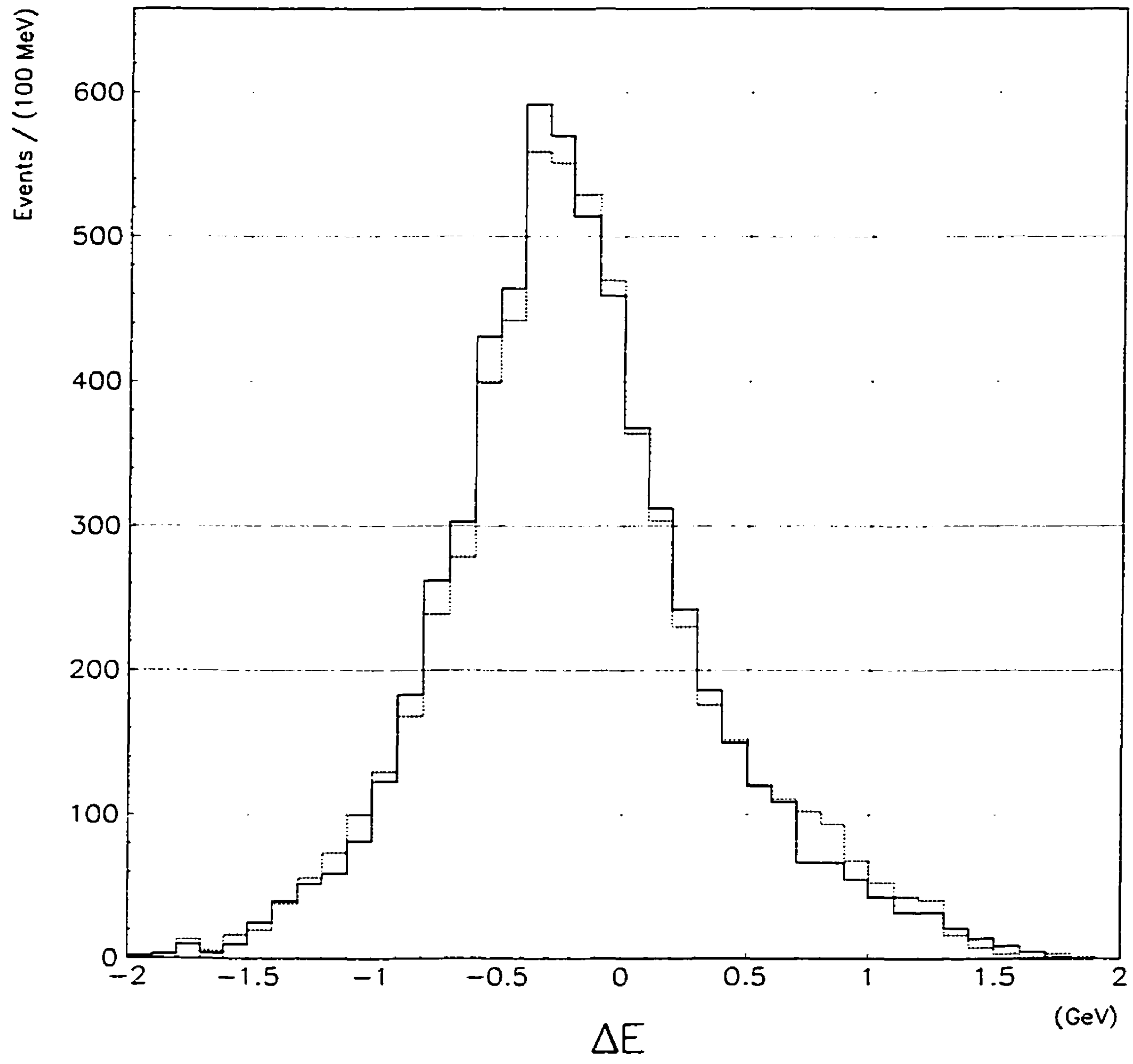

Figure 5.23: ΔE plot for the Monte Carlo M_B signal band of the D central band (full line), and the sum of sidebands and tagged Monte Carlo D's (dashed line). The two plots are in good agreement when comparing their shape and normalization.

the D sideband subtraction to get rid of the badly reconstructed D's. This subtraction turns out to represent the biggest part of our backgrounds. This is the case since from Figure 5.2 we can calculate that we have a ratio of 3 to 1 of background events to signal events. Another source of backgrounds comes from the continuum. This has been dealt with by doing a continuum subtraction as explained in Section 5.2.1. Whatever background is left comes from wrong pions since we've seen that backgrounds due to electron misidentification is very small, and hence negligible. So the last background contribution comes from the bad combinatoric pion. This means that in our event selection we have the right D meson selected as well as the right electron, but we select the wrong pion out of the event. Of the two methods for getting this remaining background we use the one involving our Monte Carlo sample. We do all the selection rules and then look at the MC truth of our selected D meson.

We then carried out several sideband studies where we restrict ourselves to some region next to our signal region. We thus studied the ΔE sidebands, the positive and negative one. In these studies we considered Monte Carlo events only and obtained quite a good agreement between the D central band describing our signal within this sideband and the D sideband plus the MC tagged D's describing our backgrounds. We also did a similar study with the data sample, where we used the data for the D central and sideband region, but still used the Monte Carlo for the tagged D contribution. Again we had a good agreement between the two plots. The final study was to look at the M_B sideband. In this case we compare the corresponding ΔE plots in a similar way as we did in the previous studies where we compared the M_B plots. We did this study for Monte Carlo only first and then for the data sideband too. In both cases we had a good agreement between the way our parametrization of the backgrounds describes the sideband signal.

One important key is that these studies were in the sideband region and hence no excess signal was either expected or observed. All these studies indicate that both signal and background are consistent in the various sidebands. We are now confident that this method gives a reliable answer to our question on how to deal with the "residual" backgrounds in our analysis.

5.4 Measuring $\mathcal{B}(B^- \to D^+\pi^-e^-\bar{\nu}_e)$

Now that all the backgrounds have been accounted for and that we are confident with the method we propose to use, we can go ahead and measure whatever excess events we have in the M_B mass bin region to extract the branching fraction on $B^- \to D^+\pi^-e^-\bar{\nu}_e$. In the sections to follow, the signal yield, the reconstruction efficiency, and then the result for $\mathcal{B}(B^- \to D^+\pi^-e^-\bar{\nu}_e)$ are presented.

5.4.1 Yield Extraction

We now use the technique that we tested in the previous sections on the various sideband studies. We perform the cuts on the D and B meson masses and then count the number of events found in the regions defined by these cuts. We then go ahead and subtract the various backgrounds with the corresponding scaling where applicable.

We measure 307 ± 20 events in the B mass region from our data sample, and 181 ± 17 events from the D sidebands. These two numbers have been corrected for the continuum contribution. We also perform this same operation for our tagged D Monte Carlo events and measure 92 ± 4 events in this region after having scaled the original number by the luminosity scaling of 0.2031. The final yield is then obtained after subtracting these two backgrounds from the signal. We measure an excess in our signal region of:

$$N_{D^+\pi^-e^-\nu_e} = 34 \pm 26 \tag{5.3}$$

The continuum and D sideband subtracted data plot overlayed with the scaled tagged D Monte Carlo background plot is shown in Figure 5.24.

5.4.2 Reconstruction Efficiencies

The efficiency of our event selection has been obtained from our signal Monte Carlo sample. All the cuts described in Chapter 4 were applied to this sample where the B^- meson decays as $B^- \to D^+\pi^-e^-\bar{\nu}_e$ and the other B decays generically. The D^+ is forced to decay to $K^-\pi^+\pi^+$ but any D^- is decayed generically. The entire procedure

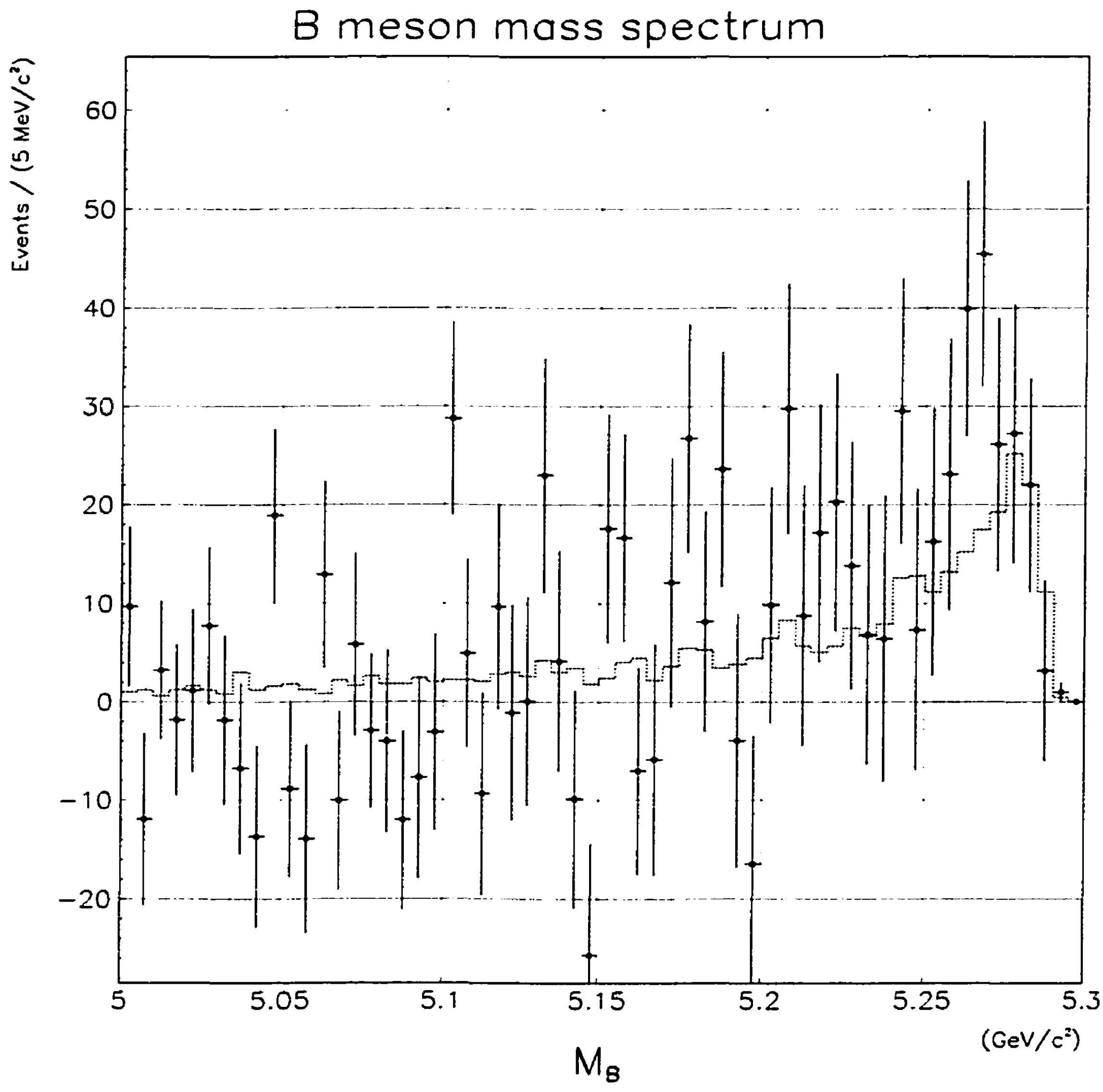

Figure 5.24: Final B meson mass spectrum. The data events were continuum and D sideband subtracted. The dashed line is the luminosity scaled tagged D Monte Carlo background sample.

applied to the data was repeated on this Monte Carlo sample. The efficiency of the signal reconstruction is obtained from the number of events that pass all the selection rules divided by the number of generated events. We obtain a signal efficiency of:

$$\epsilon_{D^+\pi^-e^-\nu_e} = 3.38 \pm 0.20\% \tag{5.4}$$

where the quoted error is statistical only. Figure 5.25 shows the final M_B distribution for tagged signal Monte Carlo events.

5.4.3 Results

The branching fraction for $\mathcal{B}(B^- \rightarrow D^+\pi^-e^-\nu_e)$ is then computed using:

$$\mathcal{B}(B^- \rightarrow D^+\pi^-e^-\nu_e) = \frac{N_{D^+\pi^-e^-\nu_e}/\epsilon_{D^+\pi^-e^-\nu_e}}{2 \times f_{+-} \times N_{\Upsilon(4S)} \times \mathcal{B}(D^+ \rightarrow K^-\pi^+\pi^+)}. \tag{5.5}$$

The yield and efficiency used in this calculation are obtained from Equations 5.3 and 5.4. The total number of $\Upsilon(4S)$ in our data sample is $N_{\Upsilon(4S)} = 3.27 \times 10^6$ and we use $\mathcal{B}(D^+ \rightarrow K^-\pi^+\pi^+) = 0.091$ as obtained from Reference [1]. We also assume that the branching fractions of $\Upsilon(4S)$ to charged and neutral $B\bar{B}$ pairs are $f_{+-} = f_{00} = 0.5$. The factor of 2 is to take into account that we have two B mesons for each $\Upsilon(4S)$.

We then obtain a final branching fraction measurement of:

$$\mathcal{B}(B^- \rightarrow D^+\pi^-e^-\nu_e) = 0.34 \pm 0.26\%, \tag{5.6}$$

where the error is statistical only. The experimental systematic error is presented in the last section of this chapter.

5.5 Upper Limit Calculation

The result we obtained on the branching fraction in the previous section is not statistically significant enough by any scientific standard. We have to convert this result into an upper limit on the measurement. We accomplish this using the Bayesian integration method where the yield is described by a Gaussian function. We interpret

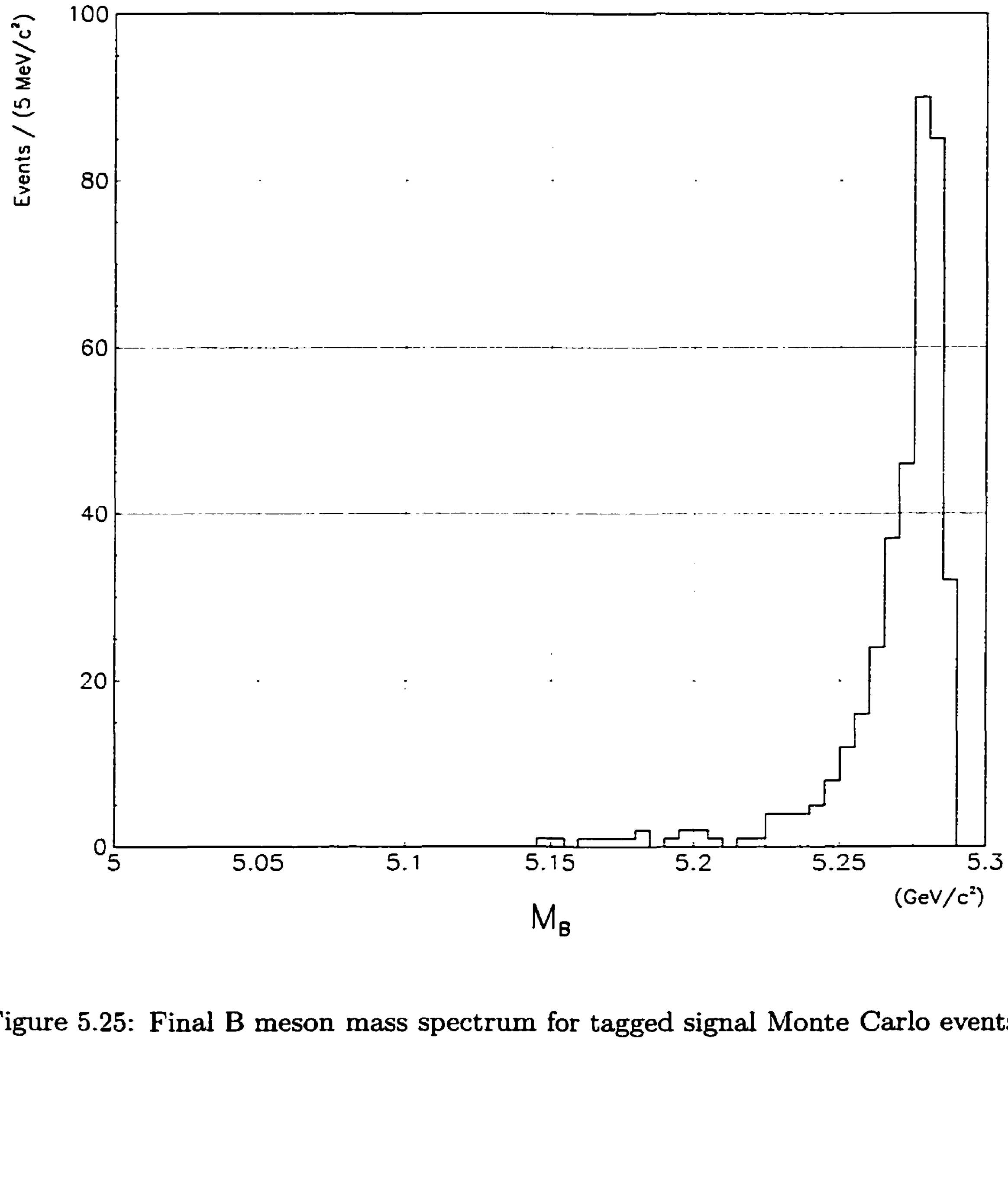

Figure 5.25: Final B meson mass spectrum for tagged signal Monte Carlo events.

the measured value in Equation 5.3 as the mean of the Gaussian and the error on this value as the sigma of the Gaussian distribution. We then integrate up to 90% of the positive area of this Gaussian. This value then corresponds to the upper limit on the number of measured events with a 90% $C.L.$ So using equation 5.3, we obtain an upper limit on the yield:

$$N_{UL} = 68.8. \tag{5.7}$$

Once we obtain the upper limit on the measured yield we can use the Equation 5.5 to calculate the upper limit on the branching fraction. This then translates into:

$$\mathcal{B}(B^- \to D^+\pi^-e^-\nu_e) < 0.68\% \text{ @ } 90\% \; C.L. \tag{5.8}$$

5.6 Systematic Studies

In this section, we estimate the impact of systematics errors on our measurement of the branching fraction of $B^- \to D^+\pi^-e^-\nu_e$. We will carefully enumerate them, and pay special attention to the largest source of uncertainty, which comes from our procedure for measuring the neutrino momentum. In general, the systematic error contributions are estimated from redoing the analysis, but by changing some of the sensitive parameters, like the normalization or the shape of a particular background source in the analysis. We then measure the yield and efficiency for each case and then recalculate the branching fraction and upper limit. The variation in the branching fraction with respect to the original analysis is considered as the systematic error attributed to the particular study. In the end, all the different contributions are added in quadrature to get the total systematic error on the branching fraction.

We now describe the detailed procedure used in extracting the systematic errors. The dominant systematic error in the analysis as mentioned before, comes from the neutrino reconstruction technique. This method relies on the reliability of our Monte Carlo simulations. We need to understand the efficiency of the event selection procedure, which means that we need to understand how often we are able to measure the neutrino momentum sufficiently precisely for a full reconstruction of the decay. The measurement of the neutrino momentum makes use of the entire detector, examining every track and shower in each event. That means that the Monte Carlo simulation used to estimate the efficiency needs to model every track and every shower throughout the entire detector, which is a rather tall order. This also affects our background studies since they are also modeled using the Monte Carlo. This mainly affects the modeling of the "other" B decay in the event. The modeling of the various generic decays of the B also affects the measurement of the efficiency and background rates.

The method used to determine the uncertainty on the result due to the modeling of the entire detector is known as the "knob turning" technique. It was originally developed for the $\bar{B} \to \pi \ell \bar{\nu}$ analysis [40, 52]. This method relies on making small changes in the Monte Carlo at the individual particle level in a variety of ways, trying to keep the modifications within reasonable bounds, based on our understanding of the detector. For each manipulation of a particular "knob" we measure the effect this has on the reconstruction efficiency and the yield measured using our method for signal extraction. The data distributions remain the same, since there is no modeling involved. From these, we then again rederive the branching fraction and note the change from the original analysis.

We list the different studies performed in Table 5.2. Some of these tests are scaled down to better represent reality. We follow this by giving some justifications why each of these knobs is being turned and by what amount. The entire set is intended to reflect the large variety of properties that are modeled by the simulation program.

1. Vary by $\pm 10\%$ the number of K_L^0's in the events. This is accomplished by reweighting the Monte Carlo sample by the corresponding factor. This shift is about twice the uncertainty in the mismatch between data and Monte Carlo in the number K_L mesons that was measured in the $\bar{B} \to \tau \bar{\nu}$ analysis [53]. Thus, we reduce the effect of this knob by 1/2 when we calculate the systematic error.

2. Vary by $\pm 17\%$ the amount of secondary leptons in the events. Again we accomplish this by reweighting the Monte Carlo sample by the corresponding factor. This shift is about twice the uncertainty in the mismatch between data and

Table 5.2: Knobs for the knob turning study

Knob	Effect
0	No changes
1	$\pm 10\%$ K_L^0
2	$\pm 17\%$ of secondary leptons
3	Throw out 1% of tracks
4	Throw out 3% of clusters
5	Use all KINCD values
6	Keep rejected splitoff cluster
7	Change clusters smearing by $\pm 10\%$
8	Change tracks smearing by $\pm 10\%$

Monte Carlo in the number of secondary leptons that were measured in an analysis of inclusive lepton production in B decays [19]. Thus, we reduce the effect of this knob by 1/2 when we calculate the systematic error.

3. Randomly remove 1.0% of tracks in the detector. The track-finding efficiency uncertainty has historically been one of the most important, and therefore most studied, quantities in the CLEO experiment [54], as all analyses depend on it.

4. Randomly remove 3% of showers in the calorimeter, which gives a decrease in photon-finding efficiency of 3%. The photon-finding efficiency has unfortunately not been studied in as great a detail as tracking efficiency, but the standard assumption is that the detector simulation models the efficiency correctly at the 2% level [55].

5. Drop the splitoff package entirely, accepting any showers with energy less than 25 MeV as splitoffs, and all other showers as photons. This represents a very extreme variation in the effectiveness of `SPLITF`. We will assume that the `SPLITF` package is reliable at the 20% level, and reduce the effect of this knob by 1/5 when we calculate the systematic error.

6. Drop the `TMNG` package entirely, treating all tracks as legitimate tracks. This extreme variation is meant to allow for different efficiency in data and Monte

Carlo. Again, we will assume that TMNG is reliable at the 20% level, and reduce the effect of this knob by 1/5 when we calculate the systematic error.

7. Increase the track momentum smearing by 10%. This is done by associating each track with the particle that created it at the generator level, calculating the difference between the measured momentum and the generator level momentum, and increasing that difference by 10%. This is an exaggeration of our momentum resolution, but we will keep the entire effect of this knob when we calculate the systematic error.

8. Increase the shower energy smearing by 10%. This smearing is done in a manner similar to that for the charged track momentum smearing.

We then summarize the individual contributions to the systematic error due to the neutrino reconstruction in Table 5.3. The final error after adding all the contributions in quadrature is 19.9%.

Table 5.3: Systematic Errors on the neutrino reconstruction due to knob turning

Uncertainty from	Get Value from	Contribution
Track Finding	Knob 3	12.2%
Fake (Clusters/Tracks)	Knob 5/6, divided by 5	11.1%
K_L^0 content	Knob 1, divided by 2	7.1%
Secondary ℓ content	Knob 2, divided by 2	6.7%
Track Smearing	Knob 7/8	3.8%
Cluster Finding	Knob 4	3.5%
Cluster Smearing	Knob 9/10	1.6%
Total		19.9%

The error on the background Monte Carlo subtraction is estimated from making several studies where we alter the set branching fraction for each contributing mode in our Monte Carlo by a certain fixed value. Since the $B^- \to D^0 e^- \bar{\nu}_e$ and $B^- \to D^{*0} e^- \bar{\nu}_e$ are well known, we vary their contribution up and down by one sigma obtained from the error on their measurement from CLEO. For the less well known decays we vary their contribution by 100%. We then extract the impact on the branching fraction produced by this change. We obtain a global variation of at most 5% in the final upper limit.

For the D sideband subtraction systematic error, we look at the problem using three different case studies. In the original analysis we assume that the background under the D^+ peak is linear. We now assume that the background takes a different kind of parametrization. We in turn parameterize the background by a quadratic and a cubic fit and also by Chebyshev functions. We observe a change in the amount subtracted from the signal region of less than 15%.

The continuum subtraction is treated similarly, by varying its contribution by one standard deviation. The effect of continuum subtraction has a small impact of 1% on the systematic error.

We combine these background subtraction contributions into one number using the quadrature method and quote a final error of 16%.

We then have an error associated with the the tracking efficiency. We attribute a 2% error for each track in our decay chain for a combined 10% error. Similarly we also have a 2% error per track for the particle identification process, which gives again a total 10% systematic error on the measurement.

The uncertainty of the branching fraction of the D^+ meson is obtained from the PDG book [1]. A 7% systematic error is associated with it.

We mentioned in Section 5.2.2 that the lepton fake rate is of the order of 0.1%. We therefore attribute a conservative 1% systematic error with this quantity.

Our measurement of the $B\bar{B}$ cross-section has an impact on the certainty of the number of $B\bar{B}$ events in our data sample. We estimate an error of 2% on this value.

We summarize all the contributions in Table 5.4. Again all the errors are added in quadrature for a final systematic error on the branching fraction ($B^- \to D^+\pi^-\ell\bar{\nu}_\ell$) of 31%.

The final systematic error is then combined with the upper limit we measured in the previous Section. We hence obtain a final result on the measurement of the upper limit on the branching fraction: $\mathcal{B}(B^- \to D^+\pi^-\ell\bar{\nu}_\ell) < 0.71\%$ at 90% C.L.

Table 5.4: Systematic Errors on $B^- \to D^+\pi^-\ell\bar{\nu}_\ell$.

Source of Systematic Errors	Contribution
Neutrino Reconstruction	20%
Background Subtraction	16%
Tracking Efficiency	10%
Particle Identification	10%
$\mathcal{B}(D^+ \to K^-\pi^+\pi^+)$	7%
Lepton Fake	1%
$B\bar{B}$ Cross-Section	2%
Total	31%

Chapter 6

Interpretations and Conclusions

6.1 Experimental Results

This thesis work presents an investigation of an exclusive semileptonic decay, the transition $B^- \to D^+\pi^-e^-\bar{\nu}_e$. Using the neutrino reconstruction technique we have set an upper limit on the measurement of its branching fraction. This is the first specific, non-resonant contribution that has been investigated experimentally. After performing all the selection rules and dealing with the remaining backgrounds by using continuum, sideband, and real tagged D monte Carlo events subtraction, we obtain a final result on the branching fraction:

$$\mathcal{B}(B^- \to D^+\pi^-e^-\bar{\nu}_e) = (0.34 \pm 0.26 \pm 0.11)\%, \tag{6.1}$$

where the first error is statistical and the second is the experimental systematic uncertainty.

This however, is not statistically significant, so we have to convert this measurement into an upper limit. We do this using the Bayesian method of interpreting a result as an upper limit on the measurement. The upper limit on the number of measured signal events in our data sample is calculated and then transformed into the upper limit on the branching fraction:

$$\mathcal{B}(B^- \to D^+\pi^-e^-\bar{\nu}_e) < 0.71\% \text{ at } 90\% \text{ C.L.} \tag{6.2}$$

This measurement was initiated in order to reconcile the deficit in the measured exclusive and inclusive semileptonic decays. Presently $2.1 \pm 1.0\%$ exclusive decays have not been accounted for and, of course, non-resonant decays should contribute to some part of this deficit.

6.2 Other Experimental Results

The present analysis is the first measurement of the particular exclusive channel presented in this analysis. Previously, the ALEPH [56] experiment at the CERN's LEP storage ring made a topological search of all the *combined* non-resonant modes during their B to $D^{(*)}X$ semileptonic study. They reported a result of:

$$\mathcal{B}(\bar{B} \to D\pi\ell\bar{\nu}_\ell) + \mathcal{B}(\bar{B} \to D^*\pi\ell\bar{\nu}_\ell) = (2.26 \pm 0.29 \pm 0.33)\%. \qquad (6.3)$$

The DELPHI [57] experiment, also at the CERN's LEP storage ring, made a similar study as ALEPH. They quoted a value for the ratio

$$\frac{\mathcal{B}(B \to D^{*-}X\,\ell^+\nu_\ell)}{\mathcal{B}(B \to D^{*-}X\,\ell^+\nu_\ell) + \mathcal{B}(B^0 \to D^{*-}\ell^+\nu_\ell)} = 0.19 \pm 0.10 \pm 0.06, \qquad (6.4)$$

where X represents neutral or charged particles. This only includes the D^*X modes and not the ones we have been interested in, mainly the DX modes. In both of these measurements, the first error is statistical and the second is the experimental systematic uncertainty.

The ALEPH measurement seems to be compatible with the current deficit although the fact that there should be other modes contributing makes it a little bit too high. The DELPHI measurement seems even higher when we consider the actual deficit and the fact that other modes should contribute in a more significant way than the D^*X mode.

6.3 Theoretical Predictions

As mentioned in Chapter 2 our signal is modeled using the Goity and Roberts model of the non-resonant decays. This model, using the chiral perturbation theory, predicts that $\mathcal{B}(B^- \to D\pi\ell\bar{\nu}_\ell) \simeq 1\%$. Also it expects a $\mathcal{B}(B^- \to D^*\pi\ell\bar{\nu}_\ell) \simeq 0.2\%$.

A new model that has been published recently by Isgur, has predictions on several two body non-resonant semileptonic decays . The author predicts smaller branching fractions for the non-resonant $D\pi$ decays, and predicts other contributions that should be considered. Our signal channel should account for at most $\mathcal{B}(B^- \rightarrow D\pi\ell\bar{\nu}_\ell) \simeq 0.2\%$

6.4 Interpretations

The first interpretation we make of these results is that our measurement is in agreement with the model on which we based our analysis. We only looked at the $B^- \rightarrow D^+\pi^-e^-\bar{\nu}_e$ decay. The other charge conjugate mode has to be accounted in a similar way. This other mode is the $B^- \rightarrow D^0\pi^0\ell\bar{\nu}_\ell$. These two modes have the magnitudes of their amplitude in the ratio of $\sqrt{2} : 1$. Our measurement hence represents only a part of the total B_{l4} decay branching fraction predicted by the Goity and Roberts model. Our upper limit result certainly includes the prediction from the Isgur model, due to its low value. No direct conclusions should be made from this since, for a valid interpretation of this result, one would have to redo this study with Monte Carlo samples based on this model.

Another point that has to be mentioned about these non-resonant modes is that the non-resonant states at the level of the D^* will have to be accounted for since they will certainly contribute to the semileptonic B meson decay. These are the $B^- \rightarrow D^{*+}\pi^-\ell\bar{\nu}_\ell$ and the $B^- \rightarrow D^{*0}\pi^0\ell\bar{\nu}_\ell$ modes. An indication for these decays has been presented in [46].

Yet another point to keep in mind is that there are broad resonances at the D^{**} level that have not been measured yet, and probably will not be in the near future due to the extreme difficulty reconstructing these events. These will decay to $D\pi$ and $D^*\pi$ states and hence should be accounted for in the final resolution of the exclusive semileptonic deficit. There could also be higher resonances above the D^{**} states, but at the present time there is no clear evidence that these have a significant branching fraction.

6.5 Future Prospects

Future prospects are divided into three different categories. The first one is the more obvious one and consists in adding the additional data collected by CLEO. Our analysis has been done on only a portion of the overall CLEO dataset, available at the time of the analysis. The data sample is now a factor of three larger and hence the inclusion of all the data events in the analysis could improve the significance at the statistical level of the signal we are after, and perhaps convert the measured upper limit into a branching fraction measurement.

The other direction to take would be to go after these other non-resonant decays as outlined in the previous section, especially the ones including the D^* resonance since one could in principle get an extra handle on reducing backgrounds by reconstructing the D^*.

One could also make an attempt at implementing the new model by Isgur and see how it affects the extraction of the signal decay channel. Since the optimization of our selection rules is based on Monte Carlo events, the acceptance is dependent on the model we base our analysis on. This means that a different model will generate a different efficiency for reconstructing the signal in question and also our background sample will be slightly altered by the different description of all these non-resonant modes presented by this model.

Yet another alternative would be to go to the newer B-Factories that started collecting data recently, like the BaBar and BELLE experiments, where the beams are boosted with respect to each other in the lab frame. This in turn should improve vertexing studies on the various decays. Also this would allow one to distinguish more easily between the two B mesons in the decay of the $\Upsilon(4S)$, which is not possible in symmetric colliders such as CLEO. We expect that the future measurements from CLEO and the competing B-Factories will eventually resolve the deficit we have been studying. First, because of vastly improved statistics and second, because the very different systematic errors involved in the two types of machines will significantly improve the understanding of the combinatoric backgrounds.

Appendix A

Personal and Original Contributions

I started as a McGill graduate student in September of 1993. The first year was spent on graduate level courses and preparation for the qualifying examinations for graduate studies. In May of 1994, I moved to Ithaca NY, to start doing research at the Cornell University based CLEO II experiment. Right away, I started an initial analysis project at CLEO. This was oriented towards a search for the Ω_C^0 (css) baryon in data coming from the e^+e^- interactions in the CLEO detector. During that time I also contributed to the Silicon Vertex Detector (SVD) effort. I was in charge of doing hardware work on the data boards that read out events form the SVD. These boards which were manufactured at the Carleton University Science Workshop had to be assembled, configured and tested before being used by the experiment.

From 1995 to 1996 I worked on a major contribution to the effort to reprocess the CLEO dataset. During this period I had to develop a method for extracting fitting weights for the Billoir Filter. These weights are used by the track reconstruction algorithm to transform raw voltages as measured by the detector into track and energy shower information used by the experimenters to analyze the data. After this development period was finished, I worked on the actual recalibration of the the tracking parameters for the complete Cleo II dataset. This "recompress" of the data consisted in using a better fitting algorithm, the Billoir Filter, an enhanced set of drift functions for the gas detectors and an improved geometry alignment algorithm. This is described briefly in Appendix C.

Once the calibration process was finished, I started working on analysis on a topic towards my Ph.D. degree. This is described in the body of the thesis and concerns semileptonic decays of B mesons to charm mesons. There was, and there still exists a significant discrepancy in the inclusive and exclusive semileptonic branching fractions of B mesons as measured by CLEO and other detectors at CERN. The purpose of my analysis was to look at the not yet detected $B^- \rightarrow D^+\pi^-e^-\bar{\nu}_e$ non-resonant decays in order to address the source of this discrepancy. A new upper limit was set for this branching ratio for the first time with the conclusion that this particular decay mode is not sufficient to explain the discrepancy.

Appendix B

CLEO Collaboration

This list of collaborators includes all the members of the CLEO collaboration at the time of writing of this thesis.

E. Lipeles,[1] M. Schmidtler,[1] A. Shapiro,[1] W. M. Sun,[1] A. J. Weinstein,[1] F. Würthwein,[1,1] D. E. Jaffe,[2] G. Masek,[2] H. P. Paar,[2] E. M. Potter,[2] S. Prell,[2] V. Sharma,[2] D. M. Asner,[3] A. Eppich,[3] T. S. Hill,[3] R. J. Morrison,[3] H. N. Nelson,[3] R. A. Briere,[4] B. H. Behrens,[5] W. T. Ford,[5] A. Gritsan,[5] J. Roy,[5] J. G. Smith,[5] J. P. Alexander,[6] R. Baker,[6] C. Bebek,[6] B. E. Berger,[6] K. Berkelman,[6] F. Blanc,[6] V. Boisvert,[6] D. G. Cassel,[6] M. Dickson,[6] P. S. Drell,[6] K. M. Ecklund,[6] R. Ehrlich,[6] A. D. Foland,[6] P. Gaidarev,[6] L. Gibbons,[6] B. Gittelman,[6] S. W. Gray,[6] D. L. Hartill,[6] B. K. Heltsley,[6] P. I. Hopman,[6] C. D. Jones,[6] D. L. Kreinick,[6] M. Lohner,[6] A. Magerkurth,[6] T. O. Meyer,[6] N. B. Mistry,[6] E. Nordberg,[6] J. R. Patterson,[6] D. Peterson,[6] D. Riley,[6] J. G. Thayer,[6] P. G. Thies,[6] B. Valant-Spaight,[6] A. Warburton,[6] P. Avery,[7] C. Prescott,[7] A. I. Rubiera,[7] J. Yelton,[7] J. Zheng,[7] G. Brandenburg,[8] A. Ershov,[8] Y. S. Gao,[8] D. Y.-J. Kim,[8] R. Wilson,[8] T. E. Browder,[9] Y. Li,[9] J. L. Rodriguez,[9] H. Yamamoto,[9] T. Bergfeld,[10] B. I. Eisenstein,[10] J. Ernst,[10] G. E. Gladding,[10] G. D. Gollin,[10] R. M. Hans,[10] E. Johnson,[10] I. Karliner,[10] M. A. Marsh,[10] M. Palmer,[10] C. Plager,[10] C. Sedlack,[10] M. Selen,[10] J. J. Thaler,[10] J. Williams,[10] K. W. Edwards,[11] R. Janicek,[12]

[1]Permanent address: Massachusetts Institute of Technology, Cambridge, MA 02139.

P. M. Patel,[12] A. J. Sadoff,[13] R. Ammar,[14] A. Bean,[14] D. Besson,[14] R. Davis,[14] N. Kwak,[14] X. Zhao,[14] S. Anderson,[15] V. V. Frolov,[15] Y. Kubota,[15] S. J. Lee,[15] R. Mahapatra,[15] J. J. O'Neill,[15] R. Poling,[15] T. Riehle,[15] A. Smith,[15] J. Urheim,[15] S. Ahmed,[16] M. S. Alam,[16] S. B. Athar,[16] L. Jian,[16] L. Ling,[16] A. H. Mahmood,[16,2] M. Saleem,[16] S. Timm,[16] F. Wappler,[16] A. Anastassov,[17] J. E. Duboscq,[17] K. K. Gan,[17] C. Gwon,[17] T. Hart,[17] K. Honscheid,[17] D. Hufnagel,[17] H. Kagan,[17] R. Kass,[17] T. K. Pedlar,[17] H. Schwarthoff,[17] J. B. Thayer,[17] E. von Toerne,[17] M. M. Zoeller,[17] S. J. Richichi,[18] H. Severini,[18] P. Skubic,[18] A. Undrus,[18] S. Chen,[19] J. Fast,[19] J. W. Hinson,[19] J. Lee,[19] N. Menon,[19] D. H. Miller,[19] E. I. Shibata,[19] I. P. J. Shipsey,[19] V. Pavlunin,[19] D. Cronin-Hennessy,[20] Y. Kwon,[20,3] A.L. Lyon,[20] E. H. Thorndike,[20] C. P. Jessop,[21] H. Marsiske,[21] M. L. Perl,[21] V. Savinov,[21] D. Ugolini,[21] X. Zhou,[21] T. E. Coan,[22] V. Fadeyev,[22] Y. Maravin,[22] I. Narsky,[22] R. Stroynowski,[22] J. Ye,[22] T. Wlodek,[22] M. Artuso,[23] R. Ayad,[23] C. Boulahouache,[23] K. Bukin,[23] E. Dambasuren,[23] S. Karamov,[23] G. Majumder,[23] G. C. Moneti,[23] R. Mountain,[23] S. Schuh,[23] T. Skwarnicki,[23] S. Stone,[23] G. Viehhauser,[23] J.C. Wang,[23] A. Wolf,[23] J. Wu,[23] S. Kopp,[24] S. E. Csorna,[25] I. Danko,[25] K. W. McLean,[25] Sz. Márka,[25] Z. Xu,[25] R. Godang,[26] K. Kinoshita,[26,4] I. C. Lai,[26] S. Schrenk,[26] G. Bonvicini,[27] D. Cinabro,[27] S. McGee,[27] L. P. Perera,[27] and G. J. Zhou[27]

[1]California Institute of Technology, Pasadena, California 91125

[2]University of California, San Diego, La Jolla, California 92093

[3]University of California, Santa Barbara, California 93106

[4]Carnegie Mellon University, Pittsburgh, Pennsylvania 15213

[5]University of Colorado, Boulder, Colorado 80309-0390

[6]Cornell University, Ithaca, New York 14853

[7]University of Florida, Gainesville, Florida 32611

[8]Harvard University, Cambridge, Massachusetts 02138

[9]University of Hawaii at Manoa, Honolulu, Hawaii 96822

[10]University of Illinois, Urbana-Champaign, Illinois 61801

---

[2]Permanent address: University of Texas - Pan American, Edinburg, TX 78539.
[3]Permanent address: Yonsei University, Seoul 120-749, Korea.
[4]Permanent address: University of Cincinnati, Cincinnati, OH 45221

[11]Carleton University, Ottawa, Ontario, Canada K1S 5B6
and the Institute of Particle Physics, Canada
[12]McGill University, Montréal, Québec, Canada H3A 2T8
and the Institute of Particle Physics, Canada
[13]Ithaca College, Ithaca, New York 14850
[14]University of Kansas, Lawrence, Kansas 66045
[15]University of Minnesota, Minneapolis, Minnesota 55455
[16]State University of New York at Albany, Albany, New York 12222
[17]Ohio State University, Columbus, Ohio 43210
[18]University of Oklahoma, Norman, Oklahoma 73019
[19]Purdue University, West Lafayette, Indiana 47907
[20]University of Rochester, Rochester, New York 14627
[21]Stanford Linear Accelerator Center, Stanford University, Stanford, California 94309
[22]Southern Methodist University, Dallas, Texas 75275
[23]Syracuse University, Syracuse, New York 13244
[24]University of Texas, Austin, TX 78712
[25]Vanderbilt University, Nashville, Tennessee 37235
[26]Virginia Polytechnic Institute and State University, Blacksburg, Virginia 24061
[27]Wayne State University, Detroit, Michigan 48202

Appendix C

Drift Chamber Calibration

I now proceed to supply some details on this topic, since I have personally spent a large fraction of my time on this specific sub-project. The following is a brief description of how we did the calibration of the Drift Chamber system composed of the precision tracking layer (PTL), vertex drift chamber (VD) and the main drift chamber (DR). The goal of this process is to calibrate these detectors for the reconstruction algorithm **pass2** which then converts the raw information on events collected from the detector into physically significant information about tracks and clusters found for each event.

Before 1996 the CLEO track fitter ignored the energy loss of a track in material the track traversed and included multiple scattering approximately. During the years 1996 to 1997 a new fitter was developed and all the data collected reprocessed with it. This new data is called the recompressed data. In this recompressed data the old track fitter was replaced by the Billoir Filter also known as the Kalman Fitter. This new fitter treats both multiple scattering and energy loss. It also provides error matrices of track parameters for all tracks and better measured track parameters for low momentum tracks. It also fits each track separately for each particle hypothesis.

During this time, many other changes took place in the tracking calibration process. The two major ones are that we now have a new method for aligning the time zeros (t0's) and we generate a new set of drift functions. The time zeros algorithm was simplified and became much more robust. The drift functions were generated using a new method and became much more reliable than before.

A description of all the technical improvements to the reconstruction and some calibration procedures can be found in References [58, 59, 60]. Here we outline the procedure for obtaining the tracking constants.

The procedure to make these constants was subdivided into several stages that had to be executed in the same order for each CLEO II dataset. We started this process by subdividing each $4S$ dataset into a manageable set of run numbers.

These subdivisions had to be carefully considered. We based our judgment mainly on the experiment log files filled during the data taking process and also on shifts in the previous version of the constants. The log books were scanned for any major changes in voltages and experimental conditions, such as changes to the observed gas content in the detectors. The program `zfiles` was used to extract the later information from the previous `cd.zfx`, the drift chamber constant database.

Once the subdivisions were set, we started first tuning the time zeros. There are three different constants for the time zeros: the crates, the preamps and individual wires. The crate constant is a significant one and is not retuned during this process. It is related to the original setup and does not change from day to day. We used the same constant as the one in the previous `cd.zfx` for the crates. We would then start by running the CDFT program on each of these individual subsets of the global $4S$ dataset. We used Bhabha samples for this part of the calibration. The program CDFT would produce histograms with all the information needed for the minimization process. Once done, we would then let the preamp edges float and let them align to the overall shape of the time zeros of all the wires for each layer. This process would then have to be repeated two or three times before all the half cards would be aligned with the same edge since after each iteration the edge of the main layer would shift slightly. There are three preamps, or half-cards, per layer. Once all the preamp edges gave us a satisfactory result, we would then rerun on the bhabha samples one last time and then let the minimization algorithm adjust individual wire's time zeros edges to the overall edge of the layer. A final check could be done at this point to make sure that no mistake crept in during the wire shifts. Also, the actual constant installation in to the `cd.zfx` database was verified by this last iteration.

We then reran on the whole $4S$ dataset again with the program CDFT but with a different script file to collect information about the drift functions. We used the drift functions from the previous dataset as a starting point to accelerate this process. The very first set of the drift functions was obtained after many iterations. Once these were available the remaining data sets took only two or three iterations to converge adequately. for the other sets.

Once this collection process was complete, a new set of drift functions was generated from this information using CDOFFCAL. This process would then have to be iterated so that we converged to a stable solution. This process of generating the new drift functions also generated many histograms for monitoring purposes. These histograms were used for deciding when convergence to the final drift functions was achieved. These plots were essentially the various residual distributions. These distributions were required to be flat and as close to zero as possible for the drift functions to be classed as having converged.

During the construction of these new drift functions, usually after the first or sometimes the second iteration, we would run the geometry program cdgeom, which, using Bhabhas, would verify that all the internal detectors were appropriately aligned. Since the major data sets were separated by periods of time where the CLEO detector was opened for general access and then closed, small changes could happen and hence these studies compensated for them and readjusted everything. The drift functions would then be regenerated to take into account any shift in the geometry of the detectors. At last, one final iteration was always run as a check that the previously generated drift functions were fine. This last iteration on drift functions was not installed if in fact satisfactory results were obtained.

Once the final drift functions were obtained and installed, we used the corresponding sample of muons and adjusted the Kalman fitting weights. There were four type of weights generated: one as a function of the layer, one as a function of the drift distance, one as a function of $\cos\theta$ of the track, and one as a function of the angle ϕ in the detector. These were generated in the following order. First we generated a file containing all the necessary information for every hit corresponding to a good track. Each weight function would then be split into several bins and each bin's residuals distribution would be rescaled such that we would obtain a normal Gaussian distribution. This rescaling would be repeated for the remaining weights. Finally each of these binned distributions would be interpolated such that we would obtain a continuous function. Since all of these weights are correlated, we had to repeat this process two or three times before getting a convergence to a stable solution. In the end each hit in the detector would have a weight corresponding to the product of the four weights. This final weight is basically the error matrix associated with the track parameters in the Kalman framework. A set of fitting weights was generated for each set of drift functions. So in rare cases where we needed two sets of drift functions for a particular data set, we generated two sets of corresponding weights.

These constants were then compiled into a particular format and all of them were installed into the production `cd.zfx`. Once all the other constants needed for the various other sub-detectors were generated by appropriate expert members of the collaboration, then **pass2** was run using all of these to process the raw data and generate the compressed format ready for physics analysis.

The project took over two years to complete. All the datasets 4S1 to 4SG were reprocessed and represented the total amount of data used for this analysis. The overall improvements were significant with respect to track reconstruction, vertexing and particle ID. Many analyses were redone to take advantage of this new reprocessed data.

Bibliography

[1] Particle Data Group, Eur. Phys. J. C **3**,1 (1998).

[2] M. Gell-Mann, Phys. Lett. **8B**, 214 (1964).

[3] G. Zweig, CERN-TH-401 (1964).

[4] J.J. Aubert *et al.*, Phys. Rev. Lett. **33**, 1404 (1974).

[5] J.E. Augustin *et al.*, Phys. Rev. Lett. **33**, 1406 (1974).

[6] L. Lederman *et al.*, Phys. Rev. Lett. **39**, 252 (1977).

[7] S. Weinberg, A. Salam, and S. Glashow, Rev. Mod. Phys. **52**, 515 (1980);
S. L. Glashow, Nucl. Phys. **22**, 579 (1961);
A. Salam and J. C. Ward, Phys. Lett. **13**, 168 (1964);
S. Weinberg, Phys. Rev. Lett. **19**, 1264 (1967).

[8] N. Isgur and M. B. Wise, Phys. Lett. B **232**, 113 (1989);
N. Isgur and M. B. Wise, Phys. Lett. B **237**, 527 (1990);
A. F. Falk, H. Georgi, B. Grinstein, and M. B. Wise, Nucl. Phys. B **343**, 1 (1990).

[9] M. Kobayashi and T. Maskawa, Prog. Theor. Phys. **49**, 652 (1973).

[10] N. Cabibbo, Phys. Rev. Lett. **10**, 531 (1963).

[11] L. Wolfenstein, Phys. Rev. Lett. **51**, 1945 (1983);
L. Wolfenstein, Ann. Rev. Nucl. Part. Sci. **36**, 137 (1986).

[12] P. S. Drell, "Experimental Aspects of the Standard Model: A Short Course for Theorists", Cornell preprint CLNS 96-1453, Lectures given at Theoretical Advanced Study Institute in Elementary Particle Physics (TASI 96), Boulder, Colorado, June 1996.

[13] CLEO Collaboration, G. Bonvicini *et al.*, Phys. Rev. **D57**, 6604 (1998).

[14] J.L. Goity and W. Roberts, Phys. Rev. **D51**, 3459 (1995).

[15] B. Barish *et al.*, Phys. Rev. Lett. **76**, 1570 (1996).

[16] M. Athanas *et al.*, Phys. Rev. Lett. **79**, 2208 (1997).

[17] B. Barish *et al.*, Phys. Rev. **D51**, 1014 (1995).

[18] G. Altarelli, N. Cabibbo, G. Corbò, L. Maiani, G. Martinelli, Nucl. Phys. B **208**, 365 (1982).

[19] R. Wang, Ph.D. thesis, University of Minnesota (1994).

[20] For a marvelous review on HQET consult:
M. Neubert, Phys. Rep. **245**, 259 (1994).

[21] E. V. Shuryak, Nucl. Phys. B **93**, 134 (1980);
M. B. Voloshin and M. A. Shiftman, Sov. J. Nucl. Phys. **47**, 511 (1988).

[22] D. Scora and N. Isgur, Phys. Rev. D **52**, 2783 (1995).

[23] N. Isgur, D. Scora, B. Grinstein, M. B. Wise, Phys. Rev. D **39**, 799 (1989);
N. Isgur and M. B. Wise, Phys. Rev. D **41**, 151 (1990).

[24] J. L. Goity and W. Roberts, Phys. Rev. D **51**, 3459 (1995).

[25] T.-M. Yan *et al.*, Phys. Rev. D **46**, 1148 (1992); Erratum *ibid.* Phys. Rev. D **55**, 5851 (1997).

[26] T.-Y. Cheng *et al.*, Phys. Rev. D **48**, 3204 (1993).

[27] C. L. Y. Lee, M. Lu, and M. B. Wise, Phys. Rev. D **46**, 5040 (1992).

[28] D. Lange, A. Ryd, V. Boisvert, and A. Bellerive, CLEO internal report CBX (in progress).

[29] N. Isgur, Phys. Rev. D **60**, 074030 (1999).

[30] CLEO Collaboration, Y. Kubota *et al.*, Nucl. Instrum. Methods A **320**, 66 (1992).

[31] C. Bebek *et al.*, Nucl. Instrum. Methods A **302**, 261 (1991).

[32] C. Bebek *et al.*, Cornell preprint CLNS 93-1241(1993).

[33] GEANT - Detector Description and Simulation Tool, 1993

[34] G. Fox and S. Wolfram, Phys. Rev. Lett. **41**, 1581 (1978).

[35] M. M. Zoeller, Ph.D. thesis, SUNY Albany, 1994.

[36] S. E. Roberts, Ph.D. Thesis, University of Rochester (1997).

[37] S. E. Roberts, M. Battle and E. Thorndike, CLEO internal report CBX 93-113 (1993).

[38] S. Roberts *et al.*, CLEO internal note CBX 93-113.

[39] B.K. Heltsley, CLEO internal note CBX 92-108.

[40] L. Gibbons *et al.*, CLEO internal notes CBX 95-6 and 96-26.

[41] K. Bloom *et al.*, CLEO internal notes CBX 95-75, CBX 95-98 and CBX 96-18.

[42] C. P. O'Grady and B. Gittelman, CLEO internal report CBX 91-82 (1991).

[43] C. P. O'Grady, Ph.D. Thesis, Cornell University (1994).

[44] Brian Heltsley *et al.*, CLEO internal note CBX 95-35 (1995).

[45] D. Bortoletto *et al.*, Nucl. Instrum. Methods A **320**, 114 (1992).

[46] A. Bellereive, Ph.D. Thesis, University (1997).

[47] W. R. Leo, "Techniques for Nuclear and Particle Physics Experiments", Springler-Verlag (1987).

[48] S. Roberts *et al.*, CBX 97-44

[49] M.S. Alam *et al.*, Phys. Rev. D **50**, 43 (1994).

[50] C.H. Wang *et al.*, "Electron Identification with CLEO II," CBX 91-52.

[51] HBOOK Manual p.90

[52] J.P. Alexander *et al.*, Phys. Rev. Lett. **77**, 5000 (1996).

[53] M. Artuso *et al.*, Phys. Rev. D **75**, 785 (1995).

[54] D. Besson, CLEO internal notes CBX 93-1, CBX 93-96, CBX 95-46, CBX 96-1, CBX 96-75; J.R. Patterson and J.G. Smith, CLEO internal note CBX 95-39.

[55] G. Ludwig, CLEO internal note CBX 92-25.

[56] ALEPH Collaboration, D. Buskulic *et al.*, Z. Phys. C **73**, 601 (1997); ALEPH Collaboration, D. Buskulic *et al.*, Phys. Lett. B **345**, 103 (1995).

[57] DELPHI Collaboration, P. Abreu etal, Z. Phys. C **71**, 539 (1996).

[58] A. Bellerive, S.L. Jones, M. Garcia-Sciveres, CLEO internal note CBX 94-39.

[59] R. Kutschke and A. Ryd, CLEO internal note CBX 96-20.

[60] A. Ryd, Ph.D. Thesis, University of California Santa Barbara (1996).